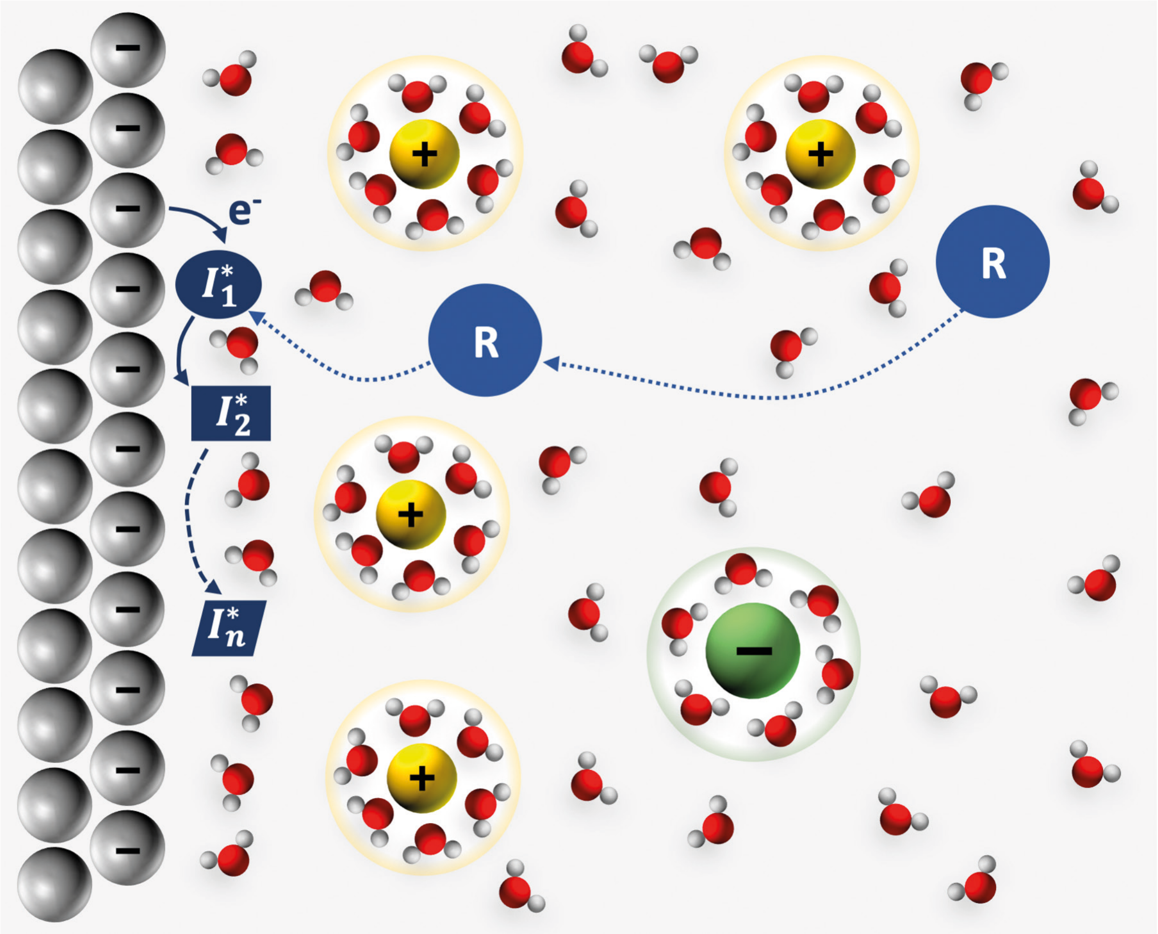

Hierarchical Modeling of Electrocatalytic Reactions from a Local Perspective

Xinwei Zhu

Energie & Umwelt / Energy & Environment
Band / Volume 695
ISBN 978-3-95806-889-6

Mitglied der Helmholtz-Gemeinschaft

JÜLICH
Forschungszentrum

Schriften des Forschungszentrums Jülich
Reihe Energie & Umwelt / Energy & Environment Band / Volume 695

Forschungszentrum Jülich GmbH
Institute of Energy Technologies (IET)
Theorie und computergestützte Modellierung von Materialien in der Energietechnik (IET-3)

Hierarchical Modeling of Electrocatalytic Reactions from a Local Perspective

Xinwei Zhu

Schriften des Forschungszentrums Jülich
Reihe Energie & Umwelt / Energy & Environment Band / Volume 695

ISSN 1866-1793 ISBN 978-3-95806-889-6

Bibliografische Information der Deutschen Nationalbibliothek.
Die Deutsche Nationalbibliothek verzeichnet diese Publikation in der
Deutschen Nationalbibliografie; detaillierte Bibliografische Daten
sind im Internet über http://dnb.d-nb.de abrufbar.

Herausgeber und Vertrieb:	Forschungszentrum Jülich GmbH Zentralbibliothek, Verlag 52425 Jülich Tel.: +49 2461 61-5368 Fax: +49 2461 61-6103 zb-publikation@fz-juelich.de www.fz-juelich.de/zb
Umschlaggestaltung:	Grafische Medien, Forschungszentrum Jülich GmbH
Druck:	Grafische Medien, Forschungszentrum Jülich GmbH

Schriften des Forschungszentrums Jülich
Reihe Energie & Umwelt / Energy & Environment, Band / Volume 695

ISSN 1866-1793
ISBN 978-3-95806-889-6

Vollständig frei verfügbar über das Publikationsportal des Forschungszentrums Jülich (JuSER)
unter www.fz-juelich.de/zb/openaccess.

Abstract

Electrocatalytic reactions, such as oxygen reduction/evolution reactions and CO_2 reduction reaction that are pivotal for the energy transition, are multi-step processes that occur in a nanoscale electric double layer (EDL) at a solid-liquid interface. Conventional analyses based on the Sabatier principle, using binding energies or effective electronic structure properties such as the d-band center as descriptors, are able to grasp overall trends in catalytic activity in specific groups of catalysts. However, thermodynamic approaches often fail to account for a plethora of electrolyte effects that arise in the EDL, including pH, cation, and anion effects. These effects have been observed to exert strong impacts on electrocatalytic reactions. There is growing consensus that the local reaction environment (LRE) in the EDL is the key to deciphering these complex and hitherto perplexing electrolyte effects. Increasing attention is thus paid to designing appropriate electrolytes, positioning the LRE at center stage. To this end, unraveling the LRE is becoming a new channel of delivering needed breakthroughs in electrochemical energy science.

Theory and modeling are getting more and more important and powerful in addressing this multifaceted problem that involves physical phenomena at different scales and interacting in a multidimensional parametric space. Theoretical models developed for this purpose should treat intrinsic multistep kinetics of electrocatalytic reactions, EDL effects from sub-nm scale to the scale of 10 nm, and mass transport phenomena bridging scales from < 0.1 to 100 μm. Given the diverse physical phenomena and scales involved, it is evident that the challenge at hand surpasses the capabilities of any single theoretical or computational approach.

In this thesis, I present a hierarchical theoretical framework to address the above challenge. It seamlessly integrates several modules: (i) microkinetic modelling that accounts for various

reaction pathways; (ii) an LRE model that describes the interfacial region extending from the nanometric EDL continuously to the solution bulk; (iii) first-principles calculations that provide parameters, *e.g.*, adsorption energies, activation barriers and EDL parameters. The microkinetic model considers all elementary steps without designating an *a priori* rate-determining step. The kinetics of these elementary steps are expressed in terms of local concentrations, potential, and electric field that are co-determined by EDL charging and mass transport in the LRE model.

This framework has been applied to several crucial reactions, including electrochemical CO_2 reduction, oxygen reduction/evolution reaction, and formic acid oxidation reaction, which has yielded vital insights on electrode kinetic phenomena, *i.e.*, potential-dependent Tafel slopes, cation effects, and pH effects. This thesis provides means to navigate the intricate couplings among processes occurring across a wide spectrum of time constants and lengths, and is expected to contribute to a comprehensive understanding of the influence of multistep kinetics and local reaction conditions on electrocatalytic reactions.

Zusammenfassung

Elektrokatalytische Reaktionen, wie Sauerstoffreduktions- und Sauerstoffentwicklungsreaktionen sowie die CO_2-Reduktionsreaktion, die für die Energiewende von entscheidender Bedeutung sind, sind mehrstufige Prozesse, die in einer nanoskaligen elektrischen Doppelschicht (EDL) an einer Fest-Flüssig-Grenzfläche ablaufen. Konventionelle Analysen, die auf dem Sabatier-Prinzip basieren und Bindungsenergien oder effektive elektronische Strukturmerkmale wie das d-Band-Zentrum als Deskriptoren verwenden, sind in der Lage, allgemeine Trends in der katalytischen Aktivität spezifischer Katalysatorgruppen zu erfassen. Thermodynamische Ansätze scheitern jedoch oft daran, die Vielzahl von Elektrolyteffekten, die in der EDL auftreten, wie pH-, Kationen- und Anioneneffekte, zu berücksichtigen. Es wurde beobachtet, dass diese Effekte einen starken Einfluss auf elektrokatalytische Reaktionen ausüben. Es herrscht zunehmend Einigkeit darüber, dass die lokale Reaktionsumgebung (LRE), die in der EDL vorherrscht, der Schlüssel zum Verständnis dieser komplexen und bisher schwer fassbaren Elektrolyteffekte ist. Daher richtet sich zunehmend der Fokus darauf, geeignete Elektrolyte zu entwerfen, wobei die LRE ins Zentrum gerückt wird. Infolgedessen wird das Verständnis der LRE immer wesentlicher für die Entwicklung von Elektrokatalysatoren mit gezielt abgestimmten Eigenschaften, die dringend benötigte Durchbrüche in der elektrochemischen Energiewissenschaft ermöglichen könnten.

Theorie und Modellierung gewinnen zunehmend an Bedeutung und werden immer leistungsfähiger, um dieses facettenreiche Problem zu adressieren, das physikalische Phänomene auf verschiedenen Skalen umfasst und in einem multidimensionalen Parameterraum interagiert. Für diesen Zweck entwickelte theoretische Modelle sollten die intrinsische Mehrstufenkinetik elektrokatalytischer Reaktionen, EDL-Effekte im Bereich von Sub-Nanometern bis zu 10 Na-

nometern sowie Massentransportphänomene, die Skalen von weniger als 0.1 µm bis 100 µm überbrücken, berücksichtigen. Angesichts der Vielfalt der physikalischen Phänomene und Skalen ist offensichtlich, dass die vorliegende Herausforderung die Möglichkeiten eines einzelnen theoretischen oder rechnerischen Ansatzes übersteigt.

In dieser Dissertation stelle ich einen hierarchischen theoretischen Rahmen vor, um die oben genannten Herausforderungen zu bewältigen. Es integriert nahtlos mehrere Module: (i) eine mikrokinetische Modellierung, die verschiedene Reaktionswege berücksichtigt; (ii) ein LRE-Modell, das die Grenzflächenregion beschreibt, die sich von der nanometrischen EDL kontinuierlich bis ins Lösungsmittelvolumen erstreckt; (iii) erst-prinzipielle Berechnungen, die Parameter wie Adsorptionsenergien, Aktivierungsbarrieren und EDL-Parameter liefern. Das mikrokinetische Modell berücksichtigt alle elementaren Schritte, ohne im Voraus einen geschwindigkeitsbestimmenden Schritt festzulegen. Die Kinetik dieser elementaren Schritte wird in Abhängigkeit von lokalen Konzentrationen, Potentialen und elektrischen Feldern ausgedrückt, die durch die Aufladung der EDL und den Massentransport im LRE-Modell gemeinsam bestimmt werden.

Dieses Rahmenwerk wurde auf mehrere entscheidende Reaktionen angewendet, darunter die elektrochemische CO_2-Reduktion, Sauerstoffreduktions- und Sauerstoffentwicklungsreaktionen sowie die Ameisensäureoxidation. Dies hat wesentliche Einblicke in kinetische Phänomene an der Elektrode geliefert, wie potenzialabhängige Tafel-Steigungen, Kationen- und pH-Effekte. Diese Dissertation bietet die Möglichkeit, die komplexen Kopplungen zwischen Prozessen, die über ein breites Spektrum von Zeitkonstanten und Längenskalen ablaufen, zu navigieren. Sie soll zu einem umfassenden Verständnis des Einflusses von Mehrstufenkinetik und lokalen Reaktionsbedingungen auf elektrokatalytische Reaktionen beitragen.

Contents

List of abbreviations

CO_2RR	CO_2 reduction reaction
NH_3RR	nitrate reduction reaction
ORR	oxygen reduction reaction
OER	oxygen evolution reaction
EDL	electric double layer
HOR	hydrogen oxidation reaction
HER	hydrogen evolution reaction
FAOR	formic acid oxidation reaction
RDS	rate-determining step
DFT	density functional theory
LRE	local reaction environment
AIMD	ab initio molecular dynamics
SHE	standard hydrogen electrode
RDT	rate determining term
PNP	Poisson-Nernst-Planck
pzc	potential of zero charge
OHP	outer Helmholtz plane
RDE	rotating disk electrode
IHP	inner Helmholtz plane
RHE	reversible hydrogen electrode
RP	reaction plane

1 Introduction

1.1 Electrocatalysis as a cornerstone of energy transition

With expanding industrialization and a growing world population, the production and consumption of energy are projected to increase further, making it the primary driver of global warming and climate change. To reach net-zero emissions and limit global warming to 1.5 ℃ by mid-century, the deployment of renewable energies is essential.[1, 2] Sustainable sources of energy, such as solar and wind, are at the center of the transition to less carbon-intensive and more sustainable energy systems. However, the production of electrical energy from these sources is typically intermittent, which hinders their reliability and overall effectiveness. Electrocatalysis, driven with a supply of electricity, is a promising pathway to store intermittent energy and convert CO_2, N_2, and H_2O into valuable chemicals and fuels, as shown in Figure 1.1.

For instance, the CO_2 reduction electrolyzer can convert CO_2 into important chemical products such as ethanol, propanol, or butanol, helping to mitigate the accumulation of greenhouse gas CO_2. This technology is highly attractive, as achieving net-negative emissions of CO_2 around the year 2050 is crucial to limiting global warming to the relatively safe level of 1.5 ℃.[3] Another extensively studied technology in recent years is the water electrolyzer, which splits water into oxygen and hydrogen. Driven by green electricity, the water electrolyzer produces hydrogen, which is widely regarded as one of the most promising energy carriers, with minimal CO_2 emissions.[4]

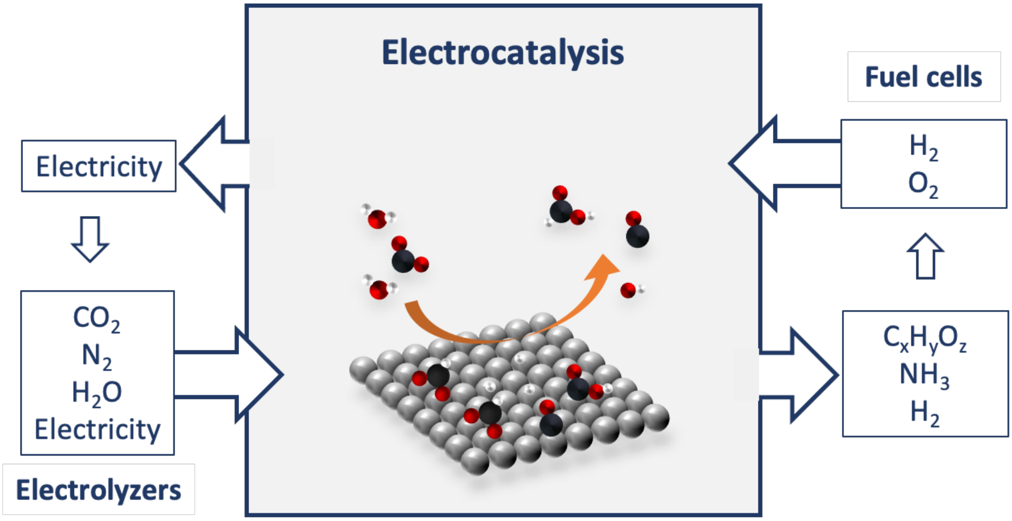

Figure 1.1: Schematic of a sustainable energy landscape based on electrocatalysis.

1.2 A key challenge in electrocatalysis

The efficiency of electrolyzers is governed by the electrocatalytic reactions at anode and cathode. Unfortunately, crucial electrocatalytic reactions, including electrochemical CO_2 reduction reaction (CO_2RR), nitrate reduction reaction (NH_3RR), and oxygen reduction/evolution reaction (ORR/OER), grapple with sluggish kinetics and inadequate selectivity. In order to make these technologies competitive for use at a large scale as part of a sustainable energy ecosystem, the underlying electrocatalytic reactions need to proceed with high efficiency. A fundamental understanding of reaction mechanisms and factors that limit activity and selectivity towards targeted products is imperative in order to prompt progress in electrolyzer design and development.

However, these endeavors are complicated and hindered by the intricate multi-step mechanisms and concurrent factors arising on multiple scales, including the reaction thermodynamics and kinetics at the atomic scale, the electric double layer (EDL) structure at the nanoscale, and the mass transport phenomena at the macroscale.[5] Further complicating matters, all these factors are intricately interconnected.

For instance, adsorbates on the electrode surface influence the surface charging relation, thereby altering the EDL structure. In some cases, the surface charging behavior as a function of potential can be non-monotonic due to residual charge on the adsorbates resulting from partial charge transfer reactions.[6, 7] At the same time, the EDL structure not only governs the reaction thermodynamics and kinetics,[5, 7–11] but also mass transport processes.[12] Specifically, the transport of reactants and products affects species concentrations, which subsequently influence the reaction kinetics and the EDL structure. These couplings make it exceptionally complex to achieve a comprehensive understanding of even simplified model reactions, such as hydrogen oxidation/evolution reactions (HOR/HER) and formic acid oxidation reaction (FAOR).[13, 14] This presents a pressing and significant challenge in the realm of electrochemistry.

To address this challenge, it is necessary to understand the interplay of these multiple factors and find a proper way to disentangle them. In this context, theory and modeling emerge as indispensable tools, that can offer critical insights and guide experimental efforts toward more efficient electrocatalytic systems.[1, 5, 15]

1.3 Essential components for understanding electrocatalysis

A fundamental step in constructing a comprehensive model for understanding electrocatalysis is identifying the crucial components that dictate reaction kinetics and interfacial behavior. Figure 1.2 depicts four essential components of a comprehensive understanding of electrocatalytic reactions:

- Multistep thermodynamics. The thermodynamics of an elementary step are determined by the binding energies of adsorbed intermediates involved in this step. Past approaches have correlated the overall activity and selectivity of a specific reaction with the binding energies of key intermediates, which are readily calculated using first-principles-based methods.[16–18] This line of research leads to the development of tools for screening catalysts, employing, for instance, the famous d-band model that had been developed by Nørskov and co-workers[16] or the generalized coordinate number model.[18]

- Multistep kinetics. Beyond thermodynamics, kinetic parameters, including but not limited to activation barriers, transfer coefficients, and preexponential factors, are important for a quantitative understanding of electrocatalysis.[19] In a few recent reports, these kinetic factors have been shown to change the qualitative trend of activity.[20–22] For instance, in a microkinetic analysis accounting for activation barriers and transfer coefficients of elementary steps, the peak of the volcano plot on the binding energy axis changes with electrode potential.[20, 21] In the quest to simplify microkinetic analyses, it has become a customary practice to identify a single step that governs the overall rate of the reaction, termed the rate-determining step (RDS).[23–25] The transition of the RDS from one step to another is often regarded as the cause of potential-dependent Tafel slopes.

- Electric double layer effects. Electrocatalytic reactions take place in the EDL at the catalyst-electrolyte interface.[8, 11, 26–28] There exist many EDL effects, including the classical Frumkin corrections (*i.e.*, the effects on potential and reactant concentration at the most probable reaction plane),[8] field-dependent adsorption energies of intermediates,[11, 27] and dependency of the solvent reorganization energy on the surface charge density.[29, 30] In addition to these equilibrium EDL effects, non-equilibrium EDL effects, firstly proposed by Levich *et al.* in the 1950s,[31] are resurfacing in recent studies.[10, 12]

- Mass transport. The consumption (production) of reactants (products) significantly influences local reactant/product concentrations and pH in the near-surface region.[14, 32] Recent progress has enabled direct probes of changes in ion concentrations and pH with a spatial resolution down to a few hundred nanometers.[33–36]

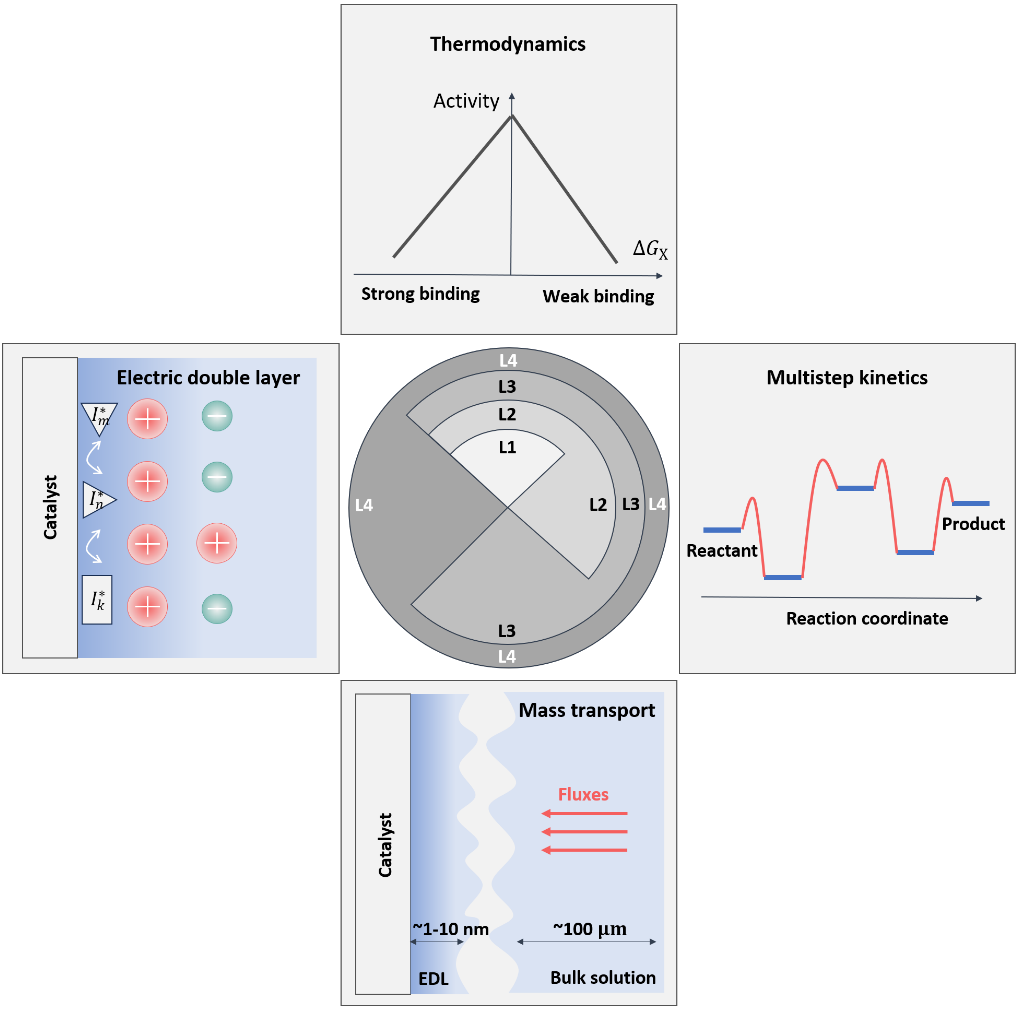

Figure 1.2: Four crucial components, *i.e.*, thermodynamics of elementary steps, multi-step kinetics, mass transport phenomena, and electric double layer, that need to be developed and involved to gain a proper understanding of the activity and selectivity of electrocatalytic reactions. Existing theoretical methodologies for electrocatalytic reactions are categorized into four levels based on the components treated. Models on level 1 (L1) consider only thermodynamics, while those on level 2 (L2) incorporate both thermodynamics and kinetics of multiple steps into a microkinetic model. Level 3 (L3) improves over L1 and L2 further by integrating the macroscopic mass transport in the electrolyte solution into the microkinetic model. Finally, level 4 (L4) completes the circle by adding electric double layer effects.

Based on the considered components, the existing theoretical methodologies for modeling electrocatalytic reactions are categorized into four levels, as summarized in Figure 1.2. Level 1 (L1) considers only thermodynamics. Specifically, L1 models focus on the potential energy profiles of electrocatalytic reactions with the binding energies of intermediates that can be readily calculated from density functional theory (DFT)-based first-principles simulations.[1, 17, 37] Despite the simplicity, L1 models can explain, surprisingly well, overall trends of activity and selectivity within groups of catalysts with similar electronic structures. The success of these models is evident from effective and easy-to-implement tools for screening catalyst materials, encompassing the d-band model,[16, 38] the generalized coordinate number,[18, 39] and volcano plots.[37, 40] In view of the simplicity of L1 models, it is unsurprising that counterexamples have been reported in the literature.[22, 41] For instance, the volcano plot predicts a sequence Pt(111) > Pt(100) > Pt(110) > Pt(211) for the ORR, yet experiments show a trend Pt(211) > Pt(110) > Pt(111) > Pt(100).[22] Additionally, concerns have been raised that the thermodynamics-based method may yield inaccurate results, due to the neglect of kinetic parameters of elementary steps, *e.g.*, activation barriers and transfer coefficients.[19–21]

As an obvious step, kinetic factors are incorporated into L1 models on level 2 (L2). L2 models treat the kinetics on two sublevels. The first sublevel relies on the RDS concept, and only the kinetics of the RDS is considered.[23–25] Practically, the RDS is often identified based on a Tafel slope analysis that is, however, problematic.[42] Values of the Tafel slope can vary to a great extent among different measurements, leading to disparate reaction mechanisms reported in different studies.[23, 24, 43–47] Furthermore, the Tafel slope exhibits high sensitivity to adsorbate coverages.[23, 46, 48] Therefore, the RDS usually changes with electrode potential. These inconsistencies necessitate a full microkinetic model that treats the thermodynamics and kinetics of all elementary steps without singling out an RDS, constituting the second sublevel on the L2. These models have been utilized to rationalize potential-dependent Tafel slopes and volcano plots for various reactions.[48–51]

Recent years have witnessed a growing awareness of the significance of electrolyte composition. Various electrolyte effects, including cation,[52–56] anion,[56, 57] and pH effects,[50, 56–58] have been observed for many reactions, yet the underlying mechanisms of these effects have remained elusive. Notably, most models on L1 and L2 fall short in interpreting electrolyte effects, as they often ignore the role of the electrolyte. Consensus is growing that these electrolyte effects originate from the change of the local reaction environment (LRE) at the catalyst-electrolyte interface, including local reactant concentrations, local pH, local potential, and local electric field within the EDL, of all which are shaped by the interplay of macroscopic mass transport and microscopic EDL charging. Therefore, resolving the LRE and its influence on the multistep kinetics has transpired as the focal point for further improvement, as emphasized in a recent Account of Xu *et al.*,

"The interplay of intrinsic microkinetics, homogeneous reactions, and mass transport limitations in determining the overall activity needs to be investigated in coupled transport–kinetic models."[28]

Following the classical works on the modeling of catalyst layers in fuel cells,[32, 59–61] refined models on level 3 (L3) incorporating mass transport into L2 models have recently been applied to the CO_2RR,[49] the HER/HOR,[50, 62] and the OER.[63] L3 models yield the local pH and reactant concentration in the diffusion layer (0.1-100 μm), the scale for models to meet experimental measurements.[33–36] For instance, Monteiro *et al.* measured the local pH during CO_2RR at a distance of 80 μm from the catalyst surface, and showed the consistency with numerical simulations.[34]

While L3 models are often claimed to be able to calculate local concentrations, it should be emphasized that the term "local" refers here to a macroscopic perspective with a scale of 0.1-100 μm. There is thus a gap to the microscopic reacting zone that is located in the EDL, which is at a much smaller scale of 0.1-10 nm. The EDL is not resolved in L3 models, while recent experimental evidence points to the central role of the EDL in understanding electrolyte effects.[9, 64–66]

1.4 Aims of this thesis

This thesis aims to incorporate EDL effects into L3 models to achieve a unified treatment of all components on level 4 (L4). This ambitious and multifaceted analysis encompasses not only the mechanism of the electrocatalytic reaction itself but also the intricacies of surface charging, the impact of partially ionic adsorbates, and the interplay of mass transport phenomena at the electrode-electrolyte interface.[7, 10, 11, 14, 51, 67–73] Given the diverse physical phenomena and scales involved, it becomes apparent that the challenge at hand surpasses the capabilities of any single theoretical or computational approach.

To address these complexities in a comprehensive yet effective manner, I have developed a hierarchical framework, as shown in Figure 1.3. It seamlessly integrates several modeling and simulation modules: (i) microkinetic modelling that accounts for various reaction pathways; (ii) an LRE model that describes the interfacial region extending from the nanometric EDL continuously to the solution bulk; (iii) first-principles calculations that provide parameters, *e.g.*, adsorption energies, activation barriers, and EDL parameters. By incorporating these components, this framework enables the decoupling of the contributions of various factors. Notably, it allows the extraction of intrinsic kinetics from the influences of the LRE, which are otherwise inaccessible in experiments.

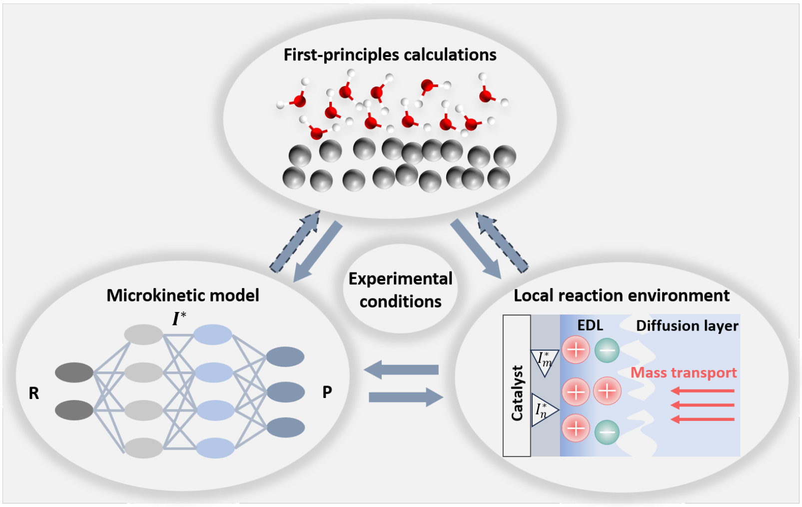

Figure 1.3: A hierarchical framework to decipher electrocatalytic reactions.

The reliability and versatility of this framework have been demonstrated through its application to understand the electrokinetics of several important reactions, including CO_2RR, OER, and FAOR. By analyzing various electrokinetic phenomena, key insights into electrocatalysis have been obtained, including potential-dependent Tafel slopes, cation effects, and pH effects—topics that are currently at the forefront of scientific debates.

During this doctoral project, several publications and contributions to publications have emerged. These works constitute the main parts of this thesis, as indicated at the beginning of each chapter. This thesis is structured as follows: Chapter 2 presents the development of the theoretical framework used in this thesis. In Chapter 3, I apply the framework to study electrochemical CO_2RR. Various kinetic phenomena observed in electrochemical CO_2 reduction at silver are understood from the perspective of the LRE. Chapter 4 focuses on disentangling the pH effects in the FAOR. Systematic comparison of the hierarchical framework and its simplified variants allows interwoven factors influencing the pH effects to be disentangled. Specifically, the distinct bell-shaped activity-pH relation in phosphate solution and the trapezoidal-shaped activity-pH relation in perchlorate solution, are deciphered. Chapter 5 presents a summary of the unique insights gained on various electrokinetic phenomena, including potential-dependent Tafel slopes, cation effects, and pH effects. These insights are general and applicable to other electrocatalytic reactions. Future possible improvements to the current framework will be discussed.

2 Building the hierarchical framework

In this chapter, I establish a theoretical framework for studying the LRE effects on electrocatalytic reactions. The framework comprises two essential submodels, as illustrated in Figure 2.1. The first submodel is a microkinetic model that integrates the thermodynamics and kinetics of all elementary steps. The second submodel processes the LRE, encompassing microscopic EDL structure and macroscopic mass transport in solution.

These two submodels are connected through boundary conditions and are solved in a self-consistent manner, *e.g.*, using COMSOL Multiphysics. The model inputs include experimental conditions such as temperature and electrolyte composition; reaction mechanisms derived from first-principles-based calculations, spectroscopic experiments, and analytical tools; energy parameters for reaction paths, *e.g.*, adsorption energies and activation barriers, obtained from DFT calculations; and EDL parameters extracted from ab initio molecular dynamics (AIMD) simulations. The model outputs include electrocatalytic performance metrics such as activity and selectivity, surface properties including adsorbate coverages and surface charging relations, and local reaction conditions such as local reactant distribution, local pH distribution, local potential distribution, and local electric field distribution.

The microkinetic model (Section 2.1) is based on my contributions to the published research article:

- Huang, J.; Zhu, X.; Eikerling, M. *The Rate-Determining Term of Electrocatalytic Reactions with First-Order Kinetics.* Electrochim. Acta 2021, 393, 139019.

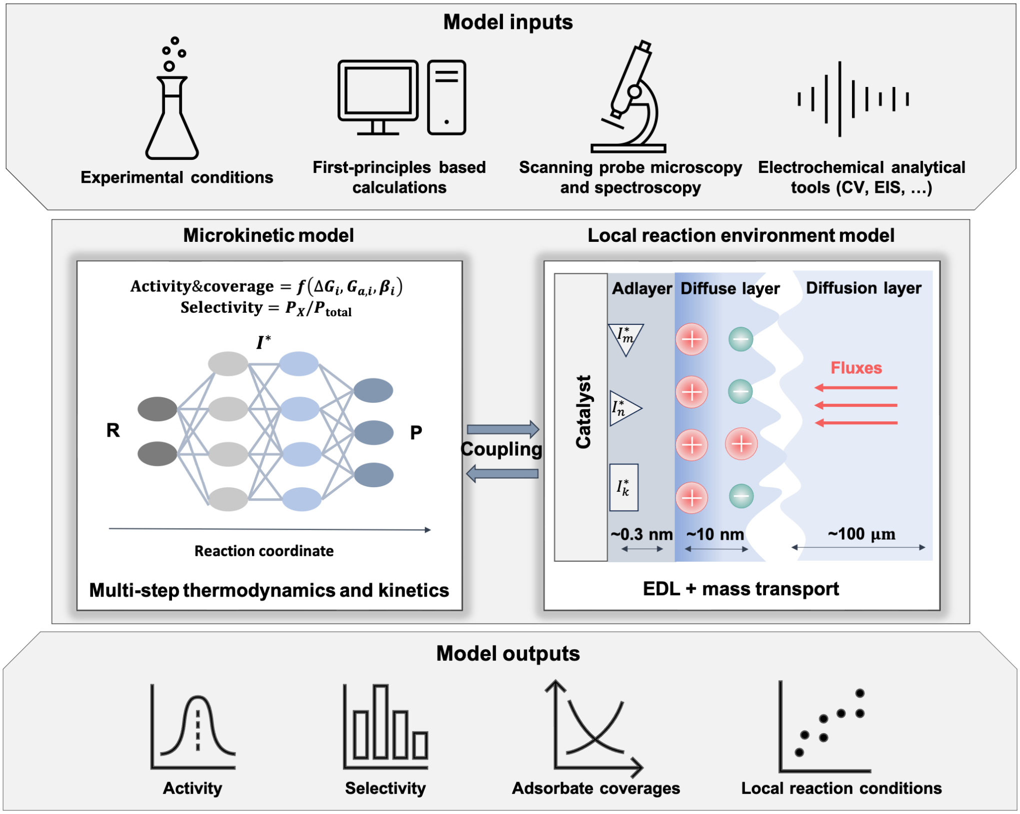

Figure 2.1: Hierarchical framework for modeling electrocatalytic reactions. The framework consists of two interrelated submodels, including a microkinetic model that accounts for the thermodynamics and kinetics of all elementary steps, and a submodel for the LRE that accounts for microscopic EDL effects and mass transport effects.

2.1 Microkinetic model

2.1.1 General formula

The microkinetic model requires *a priori* knowledge of the reaction mechanism that is usually inferred by combining key intermediates identified from spectroscopic experiments and first-principles-based calculations. A specific reaction mechanism is expressed as a series of elementary steps,

$$
\begin{aligned}
R +^* + n_1 e &\leftrightarrow I_1, \\
I_1 + n_2 e &\leftrightarrow I_2, \\
&\vdots \\
I_{i-1} + n_i e &\leftrightarrow I_i, \\
&\vdots \\
I_{N-1} + n_N e &\leftrightarrow P +^*,
\end{aligned}
\tag{2.1}
$$

where R and P denote the reactant and product, * denotes free sites on the catalyst surface for adsorption, I_i is an adsorbed intermediate with coverage θ_i, and n_i is the number of electrons transferred in the ith step.

The net rates of elementary steps are given by,

$$r_i = k_{+i}\theta_{i-1} - k_{-i}\theta_i, \quad i = 1, 2, \ldots, N, \tag{2.2}$$

where $\theta_0 = \theta_N$ denotes the coverage of free sites. Rate constants, k_{+i} and k_{-i}, are calculated based on transition state theory,

$$k_{\pm i} = \frac{k_B T}{h} c_{\pm i} \exp(-\frac{G_{a,\pm i}}{k_B T}). \tag{2.3}$$

Here, k_B is the Boltzmann constant, h is the Planck constant, T is the temperature, and $c_{\pm i}$ represents a concentration factor for species involved in forward or backward reactions other than the free active sites, adsorbates, and electrons.

Activation barriers, $G_{a,\pm i}$, can be written using the Brønsted–Evans–Polanyi (BEP) relation,[7, 74, 75]

$$
\begin{aligned}
G_{a,+i} &= G^0_{a,i} + \beta_i \Delta G_i, \\
G_{a,-i} &= G^0_{a,i} - (1 - \beta_i)\Delta G_i,
\end{aligned}
\tag{2.4}
$$

where $G^0_{a,i}$ is the activation energy of step i under standard conditions (1 bar pressure, pH = 0) for chemical steps, and at equilibrium potential under the standard conditions for electrochemical steps, β_i the transfer coefficient, and ΔG_i the reaction Gibbs free energy. For the electrochemical steps, ΔG_i shifts with potential in the following way,

$$\Delta G_i = n_i e(E_\mathrm{M} - \phi_\mathrm{RP} - E_i^\mathrm{eq}) + \Delta\Delta G_i, \tag{2.5}$$

with E_M being the applied potential relative to the standard hydrogen electrode (SHE), and ϕ_RP the electric potential at the reaction plane (RP). E_i^eq is the equilibrium potential of step i and is calculated using the Nernst equation,

$$E_i^\mathrm{eq} = -\frac{\Delta G_i^0}{n_i e}, \tag{2.6}$$

with ΔG_i^0 being the reaction free energy of step i under standard conditions, it can be obtained from first-principles calculations and thermodynamic modeling, as implemented in the computational hydrogen electrode scheme of Nørskov and colleagues.[17, 74] Additionally, recent studies underscore the significance of lateral interactions,[76] electric field,[77] or electrode surface charge in influencing the Gibbs free energies of adsorbates.[11, 27] These effects can be incorporated into this framework by introducing the term $\Delta\Delta G_i$, which is a function of coverages, surface charge density, and electric field.

Steady-state conditions imply

$$\frac{d\theta_i}{dt} = r_i - r_{i+1} = 0, \quad i = 1, 2, \ldots, N-1. \tag{2.7}$$

Combined with the conservation of adsorption sites,

$$\sum_{i=1}^{N} \theta_i = 1, \tag{2.8}$$

the equations in Eq. (2.7) can be solved to obtain θ_i and r_i. The steady-state current density is written as

$$j = e_0 \rho \sum_{i=1}^{N} n_i r_i, \tag{2.9}$$

with e_0 being the elementary charge and ρ being the number density of active sites at the electrode surface.

2.1.2 Rate determining term

For a reaction pathway with first-order kinetics, *i.e.*, a serial one that involves not more than one adsorbed intermediate on the reactant or product side of each elementary step, Figure 2.2(a), a closed set of equations is obtained,

$$\begin{bmatrix} k_{+1} & -k_{-1}-k_{+2} & k_{-2} & \cdots & 0 \\ 0 & k_{+2} & -k_{-2}-k_{+3} & \cdots & 0 \\ 0 & 0 & k_{+3} & \cdots & 0 \\ \vdots & \vdots & \vdots & \ddots & \vdots \\ 1 & 1 & 1 & \cdots & 1 \end{bmatrix} \begin{bmatrix} \theta_0 \\ \theta_1 \\ \theta_2 \\ \vdots \\ \theta_N \end{bmatrix} = \begin{bmatrix} 0 \\ 0 \\ 0 \\ \vdots \\ 1 \end{bmatrix}.$$

These equations can be solved for θ_i, which are expressed in a unified and compact form using a new formalism,

$$\theta_i = \frac{1}{\Xi} \sum_{j=0}^{N} \frac{\prod_{s=1}^{j} K_{P(P(i,-j),+s)}}{k_{-P(i,-j)}}, \quad i = 0, 1, 2, \ldots, N, \tag{2.10}$$

where the permutation operators $P(i, \pm j)$ depicted in Figure 2.2(b) and illustrated in Figure 2.2(c), point to the jth number counted from the ith number in the counterclockwise (-) and clockwise (+) direction, respectively. $K_i = \frac{k_{+i}}{k_{-i}}$ is the equilibrium constant of the ith elementary step. The denominator Ξ is given by

$$\Xi = \sum_{i=0}^{N} \sum_{j=0}^{N} \frac{\prod_{s=1}^{j} K_{P(P(i,-j),+s)}}{k_{-P(i,-j)}} = \sum_{i=0}^{N} \frac{1}{k_{-(i+1)}} \sum_{j=0}^{N} \prod_{s=1}^{j} K_{P(i+1,+s)}. \tag{2.11}$$

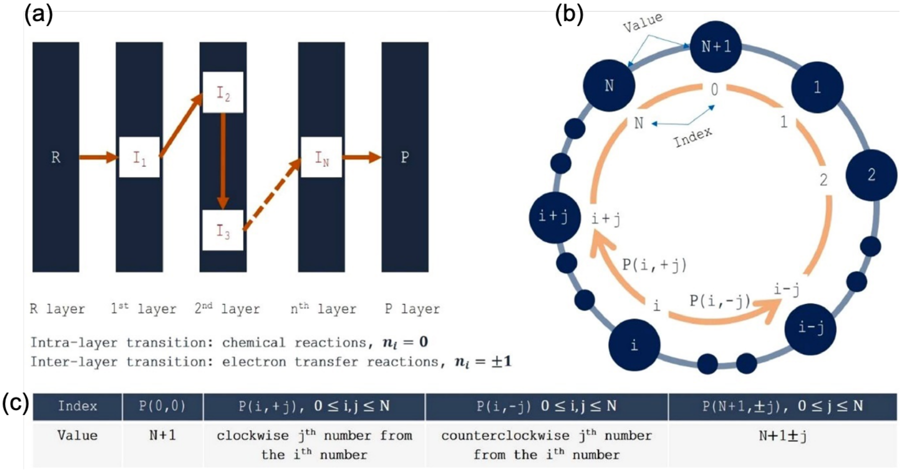

Index	P(0,0)	P(i,+j), $0 \le i,j \le N$	P(i,-j) $0 \le i,j \le N$	P(N+1,±j), $0 \le j \le N$
Value	N+1	clockwise jth number from the ith number	counterclockwise jth number from the ith number	N+1±j

Figure 2.2: (a) A multi-electron reaction with a serial reaction network. (b) Schematic diagram of the operator $P(i, \pm j)$. The inner circle corresponds to the index circle, and the outer circle represents the value circle. (c) Calculation rules of $P(i, \pm j)$. $P(i, +j)$ is the clockwise jth value from the ith value. $P(i, -j)$ is the counterclockwise jth value from the ith value. Additionally, $P(0, \pm 0) = N + 1$.

The current density, defined as $j = e\rho \sum_{i=1}^{N} n_i r_i = ne\rho r_1$, is calculated as

$$j = \frac{ne_0\rho}{\Xi} \left(\prod_{s=1}^{N+1} K_s - 1 \right). \tag{2.12}$$

$K_{total} = \prod_{s=1}^{N+1} K_s$ is the equilibrium constant of the total reaction, which is equal to 1 when the overall reaction is under equilibrium, namely, $j = 0$. As $K_{\text{total}} \propto \exp(-nF\eta/RT)$, $K_{\text{total}} \gg 1$ when an overpotential η is applied. In the overpotential region of practical interest, it is safe to assume that $K_{\text{total}} \gg 1$. $n = \sum_{i=1}^{N} n_i$ is the total electrons transferred in N steps. The inverse reaction rate (total reaction resistance) is given by

$$\frac{ne_0\rho}{j} \approx \sum_{i=1}^{N+1} \frac{\Theta_i}{k_{+i}}, \tag{2.13}$$

where thermodynamic factors Θ_i are given by

$$\Theta_i = \frac{\sum_{j=0}^{N} \prod_{s=1}^{j} K_{P(i,+s)}}{\prod_{s=1}^{N} K_{P(i,+s)}}. \tag{2.14}$$

Eq. (2.13) decomposes the overall reaction resistance into $(N+1)$ resistance terms. Usually, one of the $(N+1)$ resistance terms is much larger than the rest at specific potentials because the reaction rates vary exponentially with electrode potential. This term then determines the overall reaction resistance and is defined as the rate-determining term (RDT). The RDT is the ratio of a thermodynamic term composed of thermodynamic constants of N elementary steps to a single forward-reaction rate. The uniformity of the mathematical structure of the resistance terms will remarkably reduce the complexity of the kinetic analysis.

A simple example serves to illustrate the formalism. The example involves only one intermediate and two electrons, thus, $N=1$ and $n=2$. The Volmer-Heyrovsky mechanism of the HER, $\mathrm{H}^+ + \mathrm{e} + * \leftrightarrow \mathrm{H}_{\mathrm{ad}}$, $\mathrm{H}_{\mathrm{ad}} + \mathrm{H}^+ + \mathrm{e} \leftrightarrow \mathrm{H}_2 + *$, belongs to this category.

According to the algorithm shown in Figure 2.2(b),

$$\begin{aligned} P(0,-0) &= P(1,-1) = P(P(0,-1),+1) = 2, \\ P(0,-1) &= P(1,-0) = P(P(1,-1),+1) = 1. \end{aligned} \tag{2.15}$$

Therefore, Ξ now reads

$$\begin{aligned} \Xi &= \frac{1}{k_{-P(0,-0)}} + \frac{K_{P(P(0,-1),+1)}}{k_{-P(0,-1)}} + \frac{1}{k_{-P(1,-0)}} + \frac{K_{P(P(1,-1),+1)}}{k_{-P(1,-1)}} \\ &= \frac{1}{k_{-2}} + \frac{K_2}{k_{-1}} + \frac{1}{k_{-1}} + \frac{K_1}{k_{-2}}. \end{aligned} \tag{2.16}$$

According to Eq. (2.10), θ_0 and θ_1 are written as

$$\begin{aligned} \theta_0 &= \frac{1}{\Xi}\left(\frac{1}{k_{-P(0,-0)}} + \frac{K_{P(P(0,-1),+1)}}{k_{-P(0,-1)}}\right) = \frac{1}{\Xi}\left(\frac{1}{k_{-2}} + \frac{K_2}{k_{-1}}\right) \\ &= \frac{k_{-1} + k_{+2}}{k_{-1} + k_{+1} + k_{-2} + k_{+2}}, \\ \theta_1 &= \frac{1}{\Xi}\left(\frac{1}{k_{-P(1,-0)}} + \frac{K_{P(P(1,-1),+1)}}{k_{-P(1,-1)}}\right) = \frac{1}{\Xi}\left(\frac{1}{k_{-1}} + \frac{K_1}{k_{-2}}\right) \\ &= \frac{k_{+1} + k_{-2}}{k_{-1} + k_{+1} + k_{-2} + k_{+2}}. \end{aligned} \tag{2.17}$$

Afterwards, the current density becomes

$$\frac{2e\rho}{j} = \frac{\Theta_1}{k_{+1}} + \frac{\Theta_2}{k_{+2}}, \tag{2.18}$$

with thermodynamic factors given by

$$\begin{aligned} \Theta_1 &= \frac{1+K_2}{K_2}, \\ \Theta_2 &= \frac{1+K_1}{K_1}. \end{aligned} \tag{2.19}$$

The advantage of the presented formalism in the kinetic analyses of electrocatalytic reactions becomes more apparent when N and n are larger, namely, for more complex reactions, such as the ORR and the $CO2_2$RR.

2.1.3 Case study: oxygen reduction reaction

To demonstrate its advantage in electrocatalytic analyses, the RDT concept is applied to the ORR to clarify the inconsistencies in reported Tafel slopes across the literature. The ORR occurs via four elementary steps [7, 17, 74]:

$$O_2 + H^+ + * + e \leftrightarrow OOH_{ad}, \tag{Step 1}$$

$$OOH_{ad} + H^+ + e \leftrightarrow O_{ad} + H_2O, \tag{Step 2}$$

$$O_{ad} + H^+ + e \leftrightarrow OH_{ad}, \tag{Step 3}$$

$$OH_{ad} + H^+ + e \leftrightarrow H_2O + *. \tag{Step 4}$$

The ORR involves three adsorbates (OOH_{ad}, O_{ad} and OH_{ad}) and transfer four electrons, thus, $N = 3$ and $n = 4$. According to Eq. (2.13), the reaction resistance is decomposed into four terms,

$$\frac{4e_0\rho}{j} = \frac{\Theta_1}{k_{+1}} + \frac{\Theta_2}{k_{+2}} + \frac{\Theta_3}{k_{+3}} + \frac{\Theta_4}{k_{+4}}, \tag{2.20}$$

The thermodynamic factors are determined by using Eq. (2.13),

$$\begin{aligned}
\Theta_1 &= \frac{1 + K_2 + K_2K_3 + K_2K_3K_4}{K_2K_3K_4},\\
\Theta_2 &= \frac{1 + K_3 + K_3K_4 + K_3K_4K_1}{K_3K_4K_1},\\
\Theta_3 &= \frac{1 + K_4 + K_4K_1 + K_4K_1K_2}{K_4K_1K_2},\\
\Theta_4 &= \frac{1 + K_1 + K_1K_2 + K_1K_2K_3}{K_1K_2K_3}.
\end{aligned} \tag{2.21}$$

Figure 2.3 shows the four resistances, with parameters taken from refs. [7, 74] for Pt(111). It is apparent that $\frac{\Theta_1}{k_{+1}}$ is several orders higher than other resistances, implying that $\frac{\Theta_1}{k_{+1}}$ is the RDT of ORR at Pt(111).

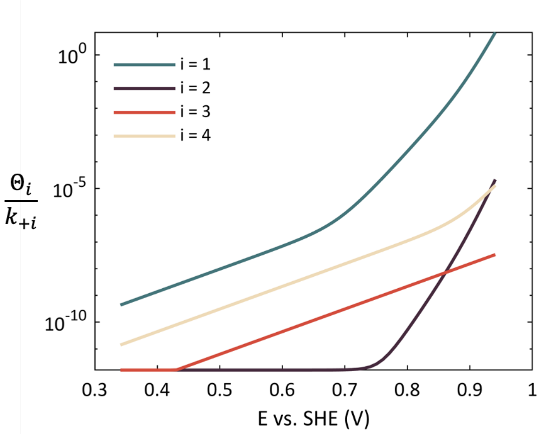

Figure 2.3: Four resistance terms of ORR, $\frac{\Theta_i}{k_{+i}}$. Parameters used in the calculation are $c_{O_2} = 0.032$ M, $c_{H^+} = 0.1$ M, $k_i^0 = 6.21 \times 10^{12}$, $G_{a,1}^{eq} = 0.37$ eV, $G_{a,2}^{eq} = G_{a,3}^{eq} = G_{a,4}^{eq} = 0.26$ eV, $\beta_i = 0.5$, $E_1^{eq} = 0.97$ V, $E_2^{eq} = 2.25$ V, $E_3^{eq} = 0.95$ V, and $E_4^{eq} = 0.75$ V. The potential is referred to the SHE.

To a further step, $\frac{\Theta_1}{k_{+1}}$ is decomposed into four subterms,

$$\frac{\Theta_1}{k_{+1}} = \frac{1}{k_{+1}K_2K_3K_4} + \frac{1}{k_{+1}K_3K_4} + \frac{1}{k_{+1}K_4} + \frac{1}{k_{+1}}. \tag{2.22}$$

At different potentials, a different term on the right-hand side dominates the electrode kinetics, as illustrated in Figure 2.4(a). Furthermore, the different subterms lead to different Tafel slopes.

The Tafel slope b is defined as,

$$b = -\frac{dE_\mathrm{M}}{d\log_{10} j}. \tag{2.23}$$

If $\frac{1}{k_{+1}K_2K_3K_4}$ is the dominated subterm, one finds

$$b = \frac{2.3RT}{F}\frac{1}{\beta_1 n_1 + n_2 + n_3 + n_4} = 17\ \mathrm{mV/dec}. \tag{2.24}$$

Similarly, $b = 24\,\mathrm{mV/dec}$ when $\frac{1}{k_{+1}+K_3K_4}$ is dominant; $b = 39\,\mathrm{mV/dec}$ when $\frac{1}{k_{+1}K_4}$ is dominant; and $b = 118\,\mathrm{mV/dec}$ when $\frac{1}{k_{+1}}$ is dominant.

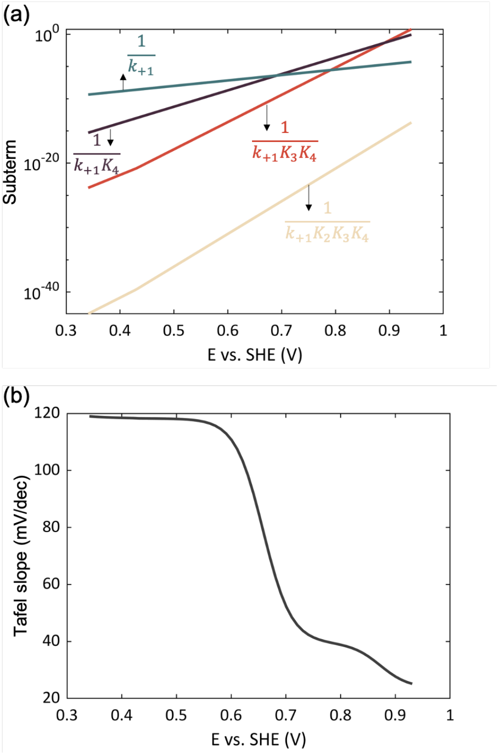

Figure 2.4: (a) Four resistance subterms in $\frac{\Theta_1}{k_{+1}}$. (b) Potential-dependent Tafel slopes of ORR.

As shown in Figure 2.4(b), the calculated Tafel slope is potential dependent, which is caused by the change of the dominant subterm. Specifically, the dominant subterm shifts from $\frac{1}{k_{+1}K_3K_4}$ to $\frac{1}{k_{+1}K_4}$ in the potential range of 0.7 V < E_M < 0.95 V, leading to b increases from 24 mV/dec to 39 mV/dec. In the potential range of 0.6 V < E_M < 0.7 V, the dominant subterm transforms from $\frac{1}{k_{+1}K_4}$ to $\frac{1}{k_{+1}}$, resulting in the increase of b from 39 mV/dec to 118 mV/dec. When $E_M < 0.6$ V, $\frac{1}{k_{+1}}$ is dominant and b remains at 118 mV/dec. Variations in Tafel slopes as gained from this analysis have been reported in literature, including 30 mV/dec,[74] 60 mV/dec,[44, 78] 77 mV/dec,[79] and 120 mV/dec.[44, 78, 80, 81] These variations in Tafel slopes are illustrated in Figure 2.4(b).

2.2 Local reaction environment model

2.2.1 Modified Poisson-Nernst-Planck theory

The Poisson-Nernst-Planck (PNP) equations have been widely used to describe ion transport in solutions throughout the twentieth century and into recent years.[10, 82] However, their standard form has limited applicability under electrocatalytic conditions. As a theory designed for dilute solutions, PNP predictions can easily violate the fundamental assumption of dilution near the electrode surface when the applied potential deviates significantly from the potential of zero charge (pzc).[83] Furthermore, the PNP theory treats ions as point charges without accounting for their finite sizes. As a result, ion concentrations increase exponentially with local potential, leading to unphysically large values at high local potentials.[84] In this section, a modified Poisson-Nernst-Planck theory is derived that considers the steric effects of particles in the solution.

The derivation starts from the free energy of the system, which is written as,

$$F = U - TS, \tag{2.25}$$

where U is the electrostatic contribution of internal energy, S the entropy and T the temperature.

The electrolyte is composed of ions and solvent molecules in general. Ions, denoted with a subscript α, have a charge of z_α and a number density of n_α. Solvent molecules, denoted with a subscript s, have a dipole moment p_s and a number density n_s. In the mean-field approximation,

U is expressed as,[71, 85]

$$U = \int \mathrm{d}V \left(-\frac{1}{2}\epsilon_{\mathrm{op}}(\nabla\phi)^2 + e_0\phi \sum z_\alpha n_\alpha - \frac{n_s}{\beta} \ln \frac{\sinh(\beta p_s \nabla\phi)}{\beta p_s \nabla\phi} \right), \tag{2.26}$$

where ϵ_{op} is the optical permittivity, ϕ the electric potential, and $\beta = \frac{1}{k_B T}$. The first term is the self-energy of the electric field, the next two terms are the electrostatic energies of the ions and solvents.

The entropy S is calculated using the lattice-gas model,[84, 86]

$$S = \int k_B \ln W, \tag{2.27}$$

where W is the number of ways of arranging all the particles in the total lattice cells,

$$W = \frac{N_t!}{N_s! \prod N_\alpha!}, \tag{2.28}$$

with N_s and N_α being particle numbers, and N_t the total number of lattice cells. The lattice cells are fully occupied without vacancy, thus N_s is given by,

$$N_s = (N_t - \sum N_\alpha \gamma_\alpha)/\gamma_s, \tag{2.29}$$

where γ_α is the size coefficient,

$$\gamma_\alpha = \left(\frac{d_\alpha}{d_t}\right)^3, \tag{2.30}$$

with d_α being the effective diameter of particle α, and d_t the reference lattice size. Taking d_s as the reference lattice size, one finds

$$N_s = N_t - \sum N_\alpha \gamma_\alpha. \tag{2.31}$$

Using the Stirling formula, namely, $\ln N! = N \ln N - N$ at $N \gg 1$, yields

$$S = -\int \mathrm{d}V k_B \left(\sum n_\alpha \ln n_\alpha + n_s \ln n_s - n_t \ln n_t + n_t - \sum n_\alpha - n_s \right). \tag{2.32}$$

Combining Eqs. (2.25), (2.26), and (2.32), the volumetric the free energy f ($F = \int f \mathrm{d}V$) is given by,

$$\begin{aligned} f = -\frac{1}{2}\epsilon_{op}(\nabla\phi)^2 + e_0\phi \sum z_\alpha n_\alpha - \frac{n_s}{\beta} \ln \frac{\sinh(\beta p_s \nabla\phi)}{\beta p_s \nabla\phi} + \\ \frac{1}{\beta} \left(\sum n_\alpha \ln n_\alpha + n_s \ln n_s - n_t \ln n_t + n_t - \sum n_\alpha - n_s \right). \end{aligned} \tag{2.33}$$

Using the Euler-Lagrange equation,

$$\frac{\partial f}{\partial X} - \nabla \left(\frac{\partial f}{\partial (\nabla X)} \right) = 0, \tag{2.34}$$

in terms of $X = \phi$ results in the modified Poisson equation,

$$\frac{\partial}{\partial x} \left(\epsilon_{\text{eff}} \frac{\partial \phi}{\partial x} \right) = -e_0 \sum z_\alpha n_\alpha, \tag{2.35}$$

with ϵ_{eff} being the effective dielectric permittivity,[87]

$$\epsilon_{\text{eff}} = \epsilon_{\text{op}} + \frac{n_s p_s}{\nabla\phi} L(\beta p_s \nabla\phi), \tag{2.36}$$

where $L(x) = \coth x - 1/x$ is the Langevin function. In the solution bulk, $\nabla\phi = 0$, thus,

$$\epsilon_{\text{eff}} = \epsilon_{\text{op}} + \beta n_s^b p_s^2/3 = \epsilon_s, \tag{2.37}$$

with n_s^b being the solvent number density in the solution bulk, and ϵ_s the bulk permittivity of the solvent medium. p_s can be obtained by solving Eq. (2.37).

The modified Nernst-Planck equation is derived by calculating the electrochemical potential of ion α using the formula,

$$\overline{\mu}_\alpha = \frac{\partial f}{\partial n_\alpha}. \tag{2.38}$$

When applying Eq. (2.38), it must be considered that $n_s = n_t - \sum n_\alpha \gamma_\alpha$ (Eq. (2.31)) is also a function of n_α. This dependence is the consequence of the fact that lattice cells are occupied by either ions or solvent molecules. Therefore, adding an ion α will simultaneously remove γ_α/γ_s solvent molecules. This consideration leads to

$$\overline{\mu}_\alpha = z_\alpha e_0 \phi + \frac{\gamma_\alpha}{\beta} \ln \frac{\sinh(\beta p_s \nabla \phi)}{\beta p_s \nabla \phi} + \frac{1}{\beta} \left(\ln n_\alpha - \gamma_\alpha \ln n_s \right). \tag{2.39}$$

For the transport dynamics near equilibrium, it is reasonable to postulate that the flux density is proportional to the gradient of the electrochemical potential,[83]

$$J_\alpha = -b_\alpha n_\alpha \nabla \overline{\mu}_\alpha = -D_\alpha \beta n_\alpha \nabla \overline{\mu}_\alpha, \tag{2.40}$$

where b_α is the mobility and D_α is the diffusion coefficient of ion α, with $b_\alpha = D_\alpha \beta$ being the Einstein relation. Combining with Eq. (2.39), J_α is determined as,

$$J_\alpha = -D_\alpha \left(\nabla n_\alpha + n_\alpha z_\alpha \beta e_0 \nabla \phi + n_\alpha \gamma_\alpha \beta p_s L(\beta p_s \nabla \phi) \nabla^2 \phi + n_\alpha \gamma_\alpha \frac{\sum_{i \neq s} \gamma_i \nabla n_i}{n_t - \sum_{i \neq s} \gamma_i n_i} \right). \tag{2.41}$$

As $n_t = \frac{1}{d_t^3}$, Eq. (2.41) is rewritten as

$$J_\alpha = -D_\alpha \left(\nabla n_\alpha + n_\alpha z_\alpha \beta e_0 \nabla \phi + n_\alpha \gamma_\alpha \beta p_s L(\beta p_s \nabla \phi) \nabla^2 \phi + n_\alpha \gamma_\alpha \frac{\sum_{i \neq s} d_i^3 \nabla n_i}{1 - \sum_{i \neq s} d_i^3 n_i} \right). \tag{2.42}$$

The mass conservation law gives

$$\frac{\partial n_\alpha}{\partial t} = -\nabla \cdot J_\alpha + R_\alpha, \tag{2.43}$$

where R_α is the source term due to homogeneous reactions, *e.g.*, conversion between CO_2 and HCO_3^- in the CO_2RR.

Since concentrations ($\mathrm{mol/m^3}$) are more commonly used than particle densities in electrocatalysis, Eqs. (2.35), (2.42), and (2.43) are transformed by using $c_\alpha = n_\alpha / N_A$, with N_A being the

Avogadro constant. This leads to

$$\begin{aligned}
&\frac{\partial}{\partial x}\left(\epsilon_{\text{eff}}\frac{\partial \phi}{\partial x}\right) = -F\sum z_\alpha c_\alpha, \\
&J_\alpha = -D_\alpha\left(\nabla c_\alpha + c_\alpha z_\alpha \beta e_0 \nabla\phi + c_\alpha \gamma_\alpha \beta p_s L(\beta p_s \nabla\phi)\nabla^2\phi + c_\alpha\gamma_\alpha \frac{\sum_{i\neq s} d_i^3 N_A \nabla c_i}{1-\sum_{i\neq s} d_i^3 N_A c_i}\right), \\
&\frac{\partial c_\alpha}{\partial t} = -\nabla\cdot J_\alpha + R_\alpha,
\end{aligned} \tag{2.44}$$

where F is the Faraday constant. The set of Eqs. (2.44) constitutes the modified PNP theory for multicomponent mass transport in solution, which are derived from a comprehensive free energy functional that considers the steric effects and solvent polarization.

When the solvent polarization and ion size asymmetry are neglected, the modified PNP theory reduces to the formula derived by Bazant *et al.* in [83],

$$\begin{aligned}
&\frac{\partial}{\partial x}\left(\epsilon_s\frac{\partial \phi}{\partial x}\right) = -F\sum z_\alpha c_\alpha, \\
&J_\alpha = -D_\alpha\left(\nabla c_\alpha + c_\alpha z_\alpha \beta e_0 \nabla\phi + c_\alpha \frac{\sum_{i\neq s} d_t^3 N_A \nabla c_i}{1-\sum_{i\neq s} d_t^3 N_A c_i}\right).
\end{aligned} \tag{2.45}$$

When the steric effects of particles and the solvent polarization are neglected, the ion flux is reduced to the standard Nernst-Planck equation,

$$J_\alpha = -D_\alpha\left(\nabla c_\alpha + c_\alpha z_\alpha \beta e_0 \nabla\phi\right). \tag{2.46}$$

2.2.2 Electric double layer model accounting for chemisorption

The modified PNP theory describes species and potential distributions beyond the outer Helmholtz plane (OHP), which represents the closest approach of solvated ions to the electrode surface. This region encompasses a diffuse layer, where the solution remains non-neutral, and a diffusion layer whose thickness varies depending on experimental conditions. For example, in rotating disk electrode (RDE) systems, the diffusion layer thickness is influenced by the rotation speed. Within the OHP, an EDL model incorporating chemisorption effects is employed, as shown in Figure 2.5.[88] The Helmholtz layer is divided into two sublayers, an inner Helmholtz layer located between the metal and the inner Helmholtz plane (IHP), which corresponds to the central plane of chemisorbed adsorbates, and an outer Helmholtz layer between the IHP and OHP.

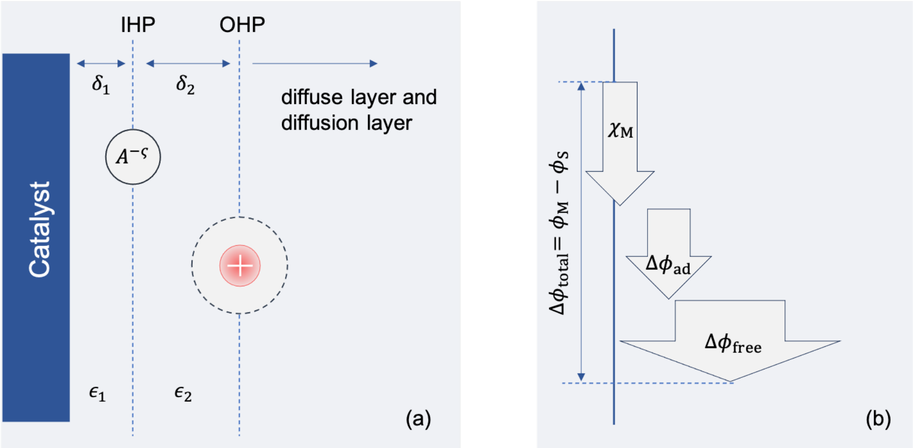

Figure 2.5: (a) Continuum EDL model consists of an IHP denoting the central plane of chemisorbed ions, and an OHP denoting the central plane of nonspecifically adsorbed ions. The regions between metal and IHP, and IHP and OHP are described as dielectric continua, parameterized with respective thicknesses δ_i and permittivities ϵ_i, with $i = 1, 2$. (b) The potential difference between the metal bulk and the solution bulk, $\Delta\phi_{\text{total}} = \phi_{\text{M}} - \phi_{\text{S}}$, can be separated into three components: χ_{M} denoting the potential drop at the metal surface due to electron distribution, $\Delta\phi_{\text{ad}}$ the potential change due to partially charged, chemisorbed ions, and $\Delta\phi_{\text{free}}$ the potential change due to excess ionic charge stored in the diffuse layer, namely, free surface charge.

The primary objective of the EDL model is to determine the electric potential distribution from the metal to the electrolyte solution. As illustrated in Figure 2.5(b), the overall potential difference $\Delta\phi_{\text{total}}$ between metal bulk (ϕ_{M}) and solution bulk (ϕ_{s}) comprises at least three components. A significant potential drop occurs at the metal surface due to the metal electron spillover, denoted as χ_{M}. Additionally, two other potential differences contribute: one arising from partially charged, chemisorbed ions, and one due to the free surface charge density, σ_{free}, defined as the negative of the net ionic charge in the diffuse layer.[6, 88]

The above decomposition scheme is expressed as [89]

$$\phi_{\text{M}} - \phi_{\text{S}} = \chi_{\text{M}} + \Delta\phi_{\text{ad}} + \Delta\phi_{\text{free}}, \tag{2.47}$$

with

$$\Delta\phi_{\text{free}} = \phi_{\text{OHP}} + \sigma_{\text{free}} \sum \frac{\delta_i}{\epsilon_i}, \tag{2.48}$$

where ϕ_{OHP} is the potential at the OHP that represents the potential change over the diffuse layer. $\Delta\phi_{\text{ad}}$ is calculated as the potential difference across an equivalent planar capacitor with a charge amount of $\sum_A e_0\rho\theta_A\varsigma_A$,

$$\Delta\phi_{\text{ad}} = \frac{\delta_1}{\epsilon_1} \sum_A e_0\rho\theta_A\varsigma_A, \tag{2.49}$$

where θ_A and ς_A are the coverage and net electron excess of a chemisorbed adsorbate A, and $\sum_A e_0\rho\theta_A\varsigma_A$ is the amount of charge carried by all adsorbates at the IHP. ς_A is positive for negatively charged adsorbates and negative for positively charged adsorbates.

As is well-known, ϕ_{M} in Eq. (2.47) is not directly measurable. In electrochemical experiments, the potential of the working electrode (WE) is measured relative to a reference electrode (RE). The electrode potential is expressed as $E_{\text{M}} = \phi_{\text{M}} - \phi_{\text{RE}}$, with ϕ_{RE} being the inner potential of the RE. If the RE is placed in the same electrolyte as the WE, the electrode potential can be rewritten as $E_{\text{M}} = (\phi_{\text{M}} - \phi_{\text{S}}) - (\phi_{\text{RE}} - \phi_{\text{S}})$. For a SHE used as the RE, $(\phi_{\text{M}} - \phi_{\text{S}})$ becomes

$$\phi_{\text{M}} - \phi_{\text{S}} = E_{\text{SHE}} + (\phi_{\text{RE}} - \phi_{\text{S}})_{\text{SHE}}, \tag{2.50}$$

where E_{SHE} is the electrode potential versus the SHE.

Combining Eq. (2.47) and Eq. (2.50) yields

$$E_{\text{SHE}} + (\phi_{\text{RE}} - \phi_{\text{S}})_{\text{SHE}} - \chi_{\text{M}} = \Delta\phi_{\text{ad}} + \Delta\phi_{\text{free}}. \tag{2.51}$$

At the pzc and in the absence of adsorbates,

$$E_{\text{SHE}}^{\text{pzc}} + (\phi_{\text{RE}} - \phi_{\text{S}})_{\text{SHE}} - \chi_{\text{M}} = 0, \tag{2.52}$$

where $E_{\text{SHE}}^{\text{pzc}}$ is the pzc versus the SHE. Therefore, $(\phi_{\text{RE}} - \phi_{\text{S}})_{\text{SHE}} - \chi_{\text{M}} = -E_{\text{SHE}}^{\text{pzc}}$. Substituting this into Eq. (2.51) yields

$$E_{\text{SHE}} - E_{\text{SHE}}^{\text{pzc}} = \Delta\phi_{\text{ad}} + \Delta\phi_{\text{free}}. \tag{2.53}$$

Finally, combining Eqs. (2.48), (2.49) and (2.53), the equation that describes the EDL structure within OHP is obtained,

$$E_{\text{SHE}} - E_{\text{SHE}}^{\text{pzc}} = \phi_{\text{OHP}} + \sigma_{\text{free}} \sum \frac{\delta_i}{\epsilon_i} + \frac{\delta_1}{\epsilon_1} \sum_A e_0 \rho \theta_A \varsigma_A. \tag{2.54}$$

It is worth noting that a more advanced EDL model, which accounts for water chemisorption, has been developed recently.[88] In that model, Eq. (2.54) requires modification to incorporate the potential drop caused by dipoles of chemisorbed water molecules.

2.3 Numerical solution of the framework

The submodels within this framework are interdependent and must be solved in a self-consistent manner. Firstly, the reaction kinetics described in Eq. (2.2) are influenced by the LRE. For instance, the reactant concentration at the reaction plane, typically chosen at the OHP for convenience in applying Frumkin corrections [11, 90], should be applied. Additionally, the rate constants are significantly affected by the local potential and electric field, as described in Eq. (2.5). These local conditions need to be determined by the LRE model. Secondly, the mass transport is governed by the partial current densities, which are obtained from the microkinetic model. Thirdly, adsorbate coverages impact the surface charging relation, as expressed in Eq. (2.54). Fourthly, the EDL model and the mass transport model are coupled to ensure a continuous description of the potential distribution from the metal surface to the bulk solution.

These connections are established through the boundary conditions for solving the modified PNP equations, as shown in Figure 2.6. The model domain spans between OHP and the solution bulk, with the diffusion layer thickness determined according to experimental conditions.[91] The right boundary is situated in the solution bulk, where concentrations match bulk concentrations, and the electric potential is taken as the reference potential, namely, $\phi = 0$. The left boundary is located at the OHP, and the fluxes at this side correlate with the current densities obtained from the microkinetic model,

$$J_i = \frac{j}{F}\frac{v_i}{n_{\text{total}}}, \tag{2.55}$$

where v_i is the respective stoichiometric number of species i, with v_i being negative for reactants and positive for products, and n_{total} is the total number of electrons involved in the reaction.

The EDL model is incorporated into the left boundary condition for the electric potential,

$$\sigma_{\text{free}} = -\epsilon_{\text{eff}} \left.\frac{\partial \phi}{\partial x}\right|_{x=0} = \frac{1}{\sum \frac{\delta_i}{\epsilon_i}} \left(E_{\text{SHE}} - E_{\text{SHE}}^{\text{pzc}} - \phi|_{x=0} - \frac{\delta_1}{\epsilon_1} \sum_A e_0 \rho \theta_A \varsigma_A \right). \tag{2.56}$$

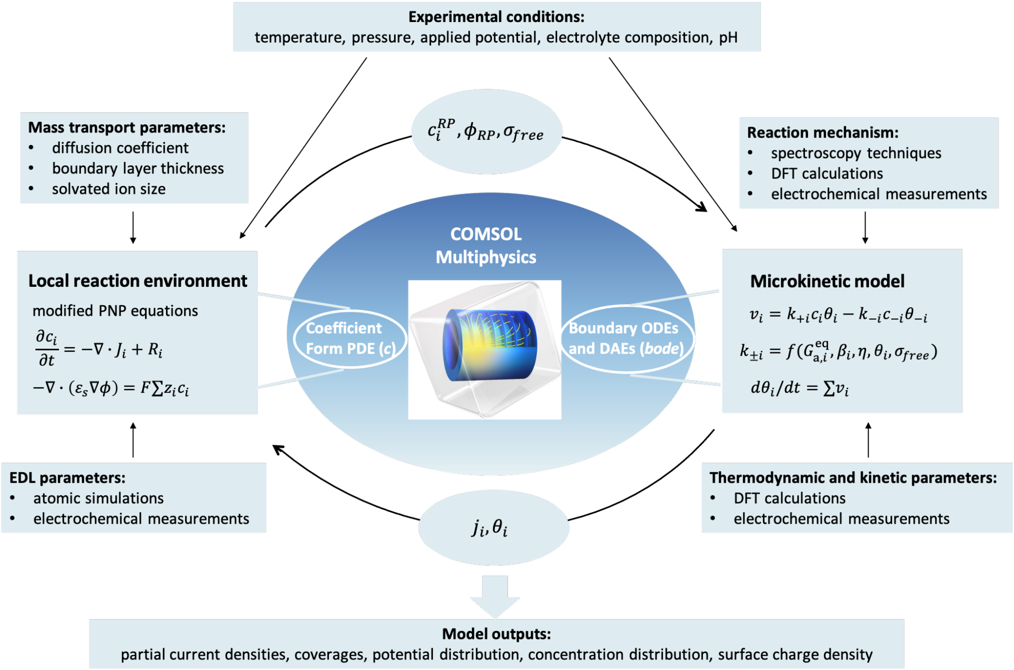

Figure 2.6: Flowchart for solving the hierarchical framework.

It has been pointed out by Johnson *et al.* that the surface charge boundary conditions are often misused in L4 models, leading to incorrect conclusions regarding EDL effects.[90] The inconsistencies arise from the adoption of inaccurate permittivity for the adlayer or the artificial imposition of an electric potential at the RP. In this thesis, key parameters are estimated based on AIMD simulations. In addition, to the best of my knowledge, the approach is unique in that it considers the surface dipole moment induced by partially charged chemisorbates. It has been shown that the residual charge on adsorbates markedly modifies the surface charging relation and the LRE.[6] Furthermore, it is worth noting that a more detailed EDL structure that accounts for the first water layer can also be integrated into Eq. (2.56).[88]

The overall model parameters can be categorized into three groups. The first group of parameters describes reaction properties, including adsorption energies, activation barriers, transfer coefficients and lateral interaction coefficients between adsorbates. These parameters are derived primarily from DFT calculations. The second group characterizes the EDL structure, encompassing the permittivity and thickness of the adlayer, effective diameters of solvated ions, and dipole moments of adsorbates. These parameters can be obtained with the aid of DFT and AIMD. The third group defines the mass transport characteristics, incorporating diffusion coefficients, bulk concentrations, and diffusion layer thickness. These parameters relate to experimental conditions. With the provided inputs, the overall model can be solved self-consistently, *e.g.*, using COMSOL Multiphysics in a computationally efficient manner.

3 Electrochemical CO_2 reduction at silver from a local perspective

In this chapter, I apply the framework to electrochemical CO_2 reduction, which is a viable process to store renewable energy and transform CO_2 into chemical fuels and value-added chemicals. The study reveals how the local reaction environment dictates the mechanism and kinetics of CO_2 reduction to CO at an Ag electrode. It yields vital mechanistic insights into the reaction behavior. The increasing Tafel slope with overpotential is seen to be influenced by the surface charging relation and mass transport effects. In addition, the decrease of the CO current density at high overpotentials is found to be caused not only by the decrease in CO_2 concentration due to mass transport, surface charge effects and pH increase, but also by lateral interactions between the adsorbates. Moreover, it will be explored how electrolyte properties, including bicarbonate concentration, solvated cation size, and CO_2 partial pressure, tune the local reaction environment.

The chapter is based on the published research article:

- Zhu, X.; Huang, J.; Eikerling, M. *Electrochemical CO_2 Reduction at Silver from a Local Perspective.* ACS Catal. 2021, 11, 23, 14521–14532.

3.1 Introduction

Electricity production from renewable energy sources will have to grow at an escalating pace if the direst consequences of climate change are to be averted. On the path towards a defossilized, environmentally benign and sustainable energy economy, two pressing challenges must be addressed: (i) the balance of anthropogenic CO_2 production must be rapidly reduced to net zero (and then net negative); (ii) the development of infrastructure concepts and technologies for large-scale and long-term energy storage must keep pace with the growth of renewable power sector.

The conversion of CO_2 into chemical fuels (and value-added chemicals), driven with a supply of renewable energy, is the most compelling option to tackle both of these challenges at once.[3, 92] However, CO_2 electrolysis is limited by a low energy efficiency and the usually low current density of fuel production. The critical CO_2RR exhibits notoriously sluggish kinetics as well as a low selectivity towards the formation of convenient transportation fuels and benign media for energy storage, such as ethanol, propanol or butanol. The latter products exhibit high energy density (J/L) and specific energy (J/kg), are liquid at ambient conditions and therefore easy to store.

CO is a key intermediate of the CO_2RR to C_{2+} products.[3, 92, 93] Au and Ag are known as the most active and selective catalysts for CO_2RR to CO.[3, 94, 95] Albeit being a seemingly simple process, CO_2 reduction to CO at Ag has not been completely understood and remains a source of controversial debates.

Tafel analysis is a vital mechanistic probe of multistep reactions. Different Tafel slopes (denoted as b) that have been reported for CO_2RR at Ag can be associated with distinct reaction mechanisms and pathways or RDSs. Rosen *et al.* determined $b = 134$ mV/dec and $b = 64$ mV/dec on polycrystalline and nanostructured Ag, respectively, in the range of low overpotentials. Based on these data, they concluded that the first proton-coupled electro transfer (PCET) step is the RDS at polycrystalline Ag, while the second proton transfer (PT) step was identified as the RDS at nanostructured Ag.[96] Dunwell *et al.* obtained $b = 59$ mV/dec on both polycrystalline Ag and nanostructured Ag at lower overpotentials, leading them to claim that the RDS at both electrodes is a PT step following upon an initial electron transfer step or PCET step.[25] Moreover, they found a Tafel slope of 118 mV/dec at higher overpotentials in their experiments, which was ascribed to mass transport effects and/or site blocking due to cation accumulation at the OHP.

First-principles computational studies have also reported different RDSs, including the hydrogenation of adsorbed CO_2 to $COOH_{ad}$,[49] or the PCET step of $COOH_{ad}$ to CO_{ad}.[77] The incongruent findings and interpretations may arise from the neglect or insufficient consideration of the LRE that prevails at the surface of the electrocatalyst, which exerts a marked impact on the apparent kinetics.[97–101] By the LRE here, I refer to not only the interfacial liquid region of several nm thickness, in which the electric potential and ion concentrations exhibit strong spatial variations, but also the surface of the solid catalyst, which is covered with multiple types of adsorbed intermediates.

Surface-enhanced infrared spectroscopy has been used to detect the concentration gradients in the region of 5-10 nm away from the electrode.[97] However, direct experimental probes of the LRE at the OHP are currently out of reach. Theoretical modelling has to step up to fill this gap in understanding, which has major implications for our ability to find or design new electrocatalyst materials and scrutinize their utility under realistic reaction conditions. A comprehensive treatment of the LRE should consider ion transport in the electrolyte solution that is dictated by the excess charge density on the electrode surface, as well as the formation and desorption of multiple adsorbed intermediates that interact with each other and with solution species in a complex way.

To date, a comprehensive theoretical treatment that accounts for these phenomena has not been devised for the CO_2RR at Ag. Several models have been developed to focus on the species transport in solution.[49, 102, 103] However, these approaches do not account for the surface charging relation of the electrode material. Ringe *et al.* developed a multiscale model for the CO_2RR at a gold electrode including surface charging effects.[11] Competitive reactions and lateral interactions were found to be minor effects in their case and therefore were not considered. However, DFT calculations have revealed the importance of interactions between intermediates $HCOO_{ad}$, $COOH_{ad}$ and H_{ad} on Ag,[76] stressing the importance of considering lateral interactions between adsorbates in kinetic modeling.

In this study, the hierarchical model is applied to describe the LRE for CO_2RR at a planar Ag electrode. Different reaction pathways, including CO pathway, H_2 pathway, and HCOOH pathway, have been considered in the microkinetic model. Armed with this approach, I unravel why the CO partial current density first increases and then decreases with overpotential, and how the Tafel slope is determined by the intrinsic kinetics and the LRE. Then, the LRE is tuned by varying the electrolyte properties, including the concentration of bicarbonate, the type of electrolyte cation, and the partial pressure of CO_2.

3.2 Model development

The reduction of CO_2 is modelled on a planar Ag(110) electrode in 0.1 M $KHCO_3$ solution at ambient conditions (25℃, 101.3 kPa). The potential of interest is between -0.3 V and -1.4 V. Hereinafter, all potentials are referenced to the reversible hydrogen electrode (RHE), unless otherwise noted. In this potential range, several reactions may occur in parallel, including the main reaction, that is, CO_2 reduction to CO, and the competitive reactions, *i.e.*, CO_2 reduction to HCOOH and HER. [104, 105]

3.2.1 Microkinetic model

The reaction mechanism used in this model includes three pathways: the CO pathway (Steps 1 and 2), the HCOOH pathway (Steps 3 and 4), and the H_2 pathway (Steps 5 and 6), forming three main products of CO_2 RR on Ag. [104, 105]

$$CO_2 + H_2O + e^- + * \rightleftharpoons COOH_{ad} + OH^- \qquad \text{(Step 1)}$$

$$COOH_{ad} + H_2O + e^- \rightarrow CO + H_2O + OH^- + * \qquad \text{(Step 2)}$$

$$CO_2 + H_2O + e^- + 2* \rightleftharpoons HCOO_{ad} + OH^- \qquad \text{(Step 3)}$$

$$HCOO_{ad} + H_2O + e^- \rightarrow HCOOH + OH^- + 2* \qquad \text{(Step 4)}$$

$$H_2O + e^- + * \rightleftharpoons H_{ad} + OH^- \qquad \text{(Step 5)}$$

$$H_{ad} + H_2O + e^- \rightarrow H_2 + OH^- + * \qquad \text{(Step 6)}$$

The following simplifications are made: (1) The reverse reactions of Steps 2, 4, and 6 are neglected considering that the solubilities of CO and H_2 are quite low,[106] and the concentration of HCOOH is negligible due to the low formation rate.[105, 107] (2) The desorption of CO_{ad} is very fast,[96, 108] so I combine $COOH_{ad}$ reduction to CO_{ad} and CO_{ad} desorption into Step 2. (3) The Tafel step of the HER is not considered since it is not energetically favorable at Ag.[49] (4) The possible inter-conversion of $COOH_{ad}$ and $HCOO_{ad}$ is not considered. $\theta_{\mathrm{COOH_{ad}}} = 0$ because $COOH_{ad}$ hardly adsorbs on Ag as demonstrated with DFT studies.[76] The simulated coverage of $COOH_{ad}$ is less than 1.8×10^{-4} in this work. Therefore, the conversion of $COOH_{ad}$ to $HCOO_{ad}$ can be neglected. In addition, DFT studies have found that $\Delta G_{\mathrm{COOH_{ad}}} - \Delta G_{\mathrm{HCOO_{ad}}} \approx 1\ eV$ on Ag,[76] which means that the conversion of $HCOO_{ad}$ to $COOH_{ad}$ is energetically unfavorable. (5) All reaction steps are considered as PCET steps, as in refs. [109–111]. I notice that sequential proton and electron transfer steps were also proposed.[112] In addition, the adsorption of CO_2 was shown to be the RDS on gold.[11] To date, there is still no consensus on the reaction mechanisms and this thus remains an important topic for future research. (6) The proton precursor here is H_2O not H^+, because the proton concentration is 1.58×10^{-7} M in 0.1 M $KHCO_3$ solution (pH = 6.8), which can only support a current density in the order of 10^{-3} mA cm^{-2}, as illustrated in Figure 3.1.

Figure 3.1 shows the distribution of proton concentration in the electrolyte, when the partial current density of H^+ is 1.7×10^{-3} mA cm^{-2}. In this case, the proton concentration near the surface approaches 0, indicating that the limiting partial current density of H^+ is only in the order of 10^{-3} mA cm^{-2}.

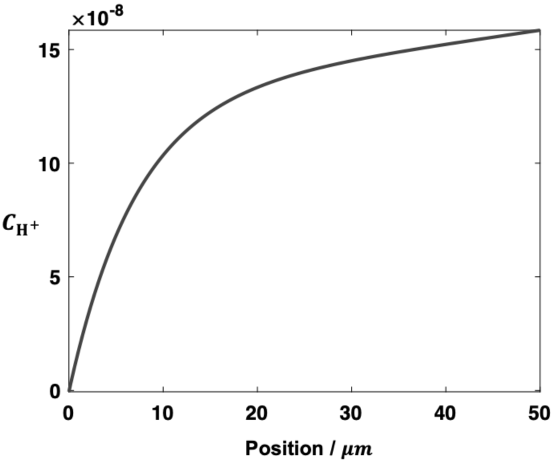

Figure 3.1: The distribution of c_{H^+} (mol/L) in solution when the partial current density of H^+ is 1.7×10^{-3} mA cm^{-2}.

Based on the reaction equations, the following system of rate equations is solved at steady state,

$$\frac{d\theta_{\mathrm{COOH_{ad}}}}{dt} = r_1 - r_2 = 0, \tag{3.1}$$

$$\frac{d\theta_{\mathrm{HCOO_{ad}}}}{dt} = r_3 - r_4 = 0, \tag{3.2}$$

$$\frac{d\theta_{\mathrm{H_{ad}}}}{dt} = r_5 - r_6 = 0, \tag{3.3}$$

where $\theta_{\mathrm{COOH_{ad}}}$, $\theta_{\mathrm{HCOO_{ad}}}$, and $\theta_{\mathrm{H_{ad}}}$ are coverages, and r_i is the reaction rate of step i. For the latter, there are the following relations,

$$r_1 = k_1 c^{\mathrm{RP}}_{\mathrm{CO_2}} \theta_0 - k_{-1} \theta_{\mathrm{COOH_{ad}}} c^{\mathrm{RP}}_{\mathrm{OH^-}}, \tag{3.4}$$

$$r_2 = k_2 \theta_{\mathrm{COOH_{ad}}}, \tag{3.5}$$

$$r_3 = k_3 c^{\mathrm{RP}}_{\mathrm{CO_2}} \theta_0^2 - k_{-3} \theta_{\mathrm{HCOO_{ad}}} c^{\mathrm{RP}}_{\mathrm{OH^-}}, \tag{3.6}$$

$$r_4 = k_4 \theta_{\mathrm{HCOO_{ad}}}, \tag{3.7}$$

$$r_5 = k_5 \theta_0 - k_{-5} \theta_{\mathrm{H_{ad}}} c^{\mathrm{RP}}_{\mathrm{OH^-}}, \tag{3.8}$$

$$r_6 = k_6 \theta_{\mathrm{H_{ad}}}, \tag{3.9}$$

with $\theta_0 = 1 - \theta_{\mathrm{COOH_{ad}}} - 2\theta_{\mathrm{HCOO_{ad}}} - \theta_{\mathrm{H_{ad}}}$ being the vacancy coverage (free sites). The concentrations $c^{\mathrm{RP}}_{\mathrm{CO_2}}$ and $c^{\mathrm{RP}}_{\mathrm{OH^-}}$ are concentrations at the reaction plane. These concentrations will be determined from the LRE model. Rate constants of the forward and reverse reactions, k_i and k_{-i}, are calculated from Eq. (2.3). For the reaction Gibbs free energy, ΔG_i, the lateral interactions between adsorbates are considered. Thus, Eq. (2.5) becomes,

$$\Delta G_i = e(E_{\mathrm{M}} - \phi_{\mathrm{RP}} - E_i^{\mathrm{eq}}) \pm \sum_{X_j} \xi_{X_j,X_i} \theta_{X_j}, \tag{3.10}$$

where $\xi_{X_j,X_i}\theta_{X_j}$ represents the variations in the Gibbs free energies caused by lateral interactions between intermediates involved in step i, X_i, and all the intermediates X_j ($\mathrm{COOH_{ad}}$, $\mathrm{HCOO_{ad}}$, $\mathrm{H_{ad}}$), with ξ_{X_j,X_i} being the lateral interaction parameters. [113]

Since $\theta_{\mathrm{COOH_{ad}}} \approx 0$, the term $\xi_{\mathrm{COOH_{ad}},X_i}\theta_{\mathrm{COOH_{ad}}}$ can be neglected. The detailed expressions for ΔG_i are written as,

$$\Delta G_1 = e(E_M - \phi_{\mathrm{RP}} - E_1^{\mathrm{eq}}) + \xi_{\mathrm{HCOO_{ad}},\mathrm{COOH_{ad}}}\theta_{\mathrm{HCOO_{ad}}} + \xi_{\mathrm{H_{ad}},\mathrm{COOH_{ad}}}\theta_{\mathrm{H_{ad}}}, \tag{3.11}$$

$$\Delta G_2 = e(E_M - \phi_{\mathrm{RP}} - E_2^{\mathrm{eq}}) - \xi_{\mathrm{HCOO_{ad}},\mathrm{COOH_{ad}}}\theta_{\mathrm{HCOO_{ad}}} - \xi_{\mathrm{H_{ad}},\mathrm{COOH_{ad}}}\theta_{\mathrm{H_{ad}}}, \tag{3.12}$$

$$\Delta G_3 = e(E_M - \phi_{\mathrm{RP}} - E_3^{\mathrm{eq}}) + \xi_{\mathrm{HCOO_{ad}},\mathrm{HCOO_{ad}}}\theta_{\mathrm{HCOO_{ad}}} + \xi_{\mathrm{H_{ad}},\mathrm{HCOO_{ad}}}\theta_{\mathrm{H_{ad}}}, \tag{3.13}$$

$$\Delta G_4 = e(E_M - \phi_{\mathrm{RP}} - E_4^{\mathrm{eq}}) - \xi_{\mathrm{HCOO_{ad}},\mathrm{HCOO_{ad}}}\theta_{\mathrm{HCOO_{ad}}} - \xi_{\mathrm{H_{ad}},\mathrm{HCOO_{ad}}}\theta_{\mathrm{H_{ad}}}, \tag{3.14}$$

$$\Delta G_5 = e(E_M - \phi_{\mathrm{RP}} - E_5^{\mathrm{eq}}) + \xi_{\mathrm{HCOO_{ad}},\mathrm{H_{ad}}}\theta_{\mathrm{HCOO_{ad}}} + \xi_{\mathrm{H_{ad}},\mathrm{H_{ad}}}\theta_{\mathrm{H_{ad}}}, \tag{3.15}$$

$$\Delta G_6 = e(E_M - \phi_{\mathrm{RP}} - E_6^{\mathrm{eq}}) - \xi_{\mathrm{HCOO_{ad}},\mathrm{H_{ad}}}\theta_{\mathrm{HCOO_{ad}}} - \xi_{\mathrm{H_{ad}},\mathrm{H_{ad}}}\theta_{\mathrm{H_{ad}}}. \tag{3.16}$$

The coverages $\theta_{\mathrm{COOH_{ad}}}$, $\theta_{\mathrm{HCOO_{ad}}}$, and $\theta_{\mathrm{H_{ad}}}$ can be obtained by solving the rate equations. The partial current densities are given by,

$$j_{\mathrm{CO}} = 2e\rho r_2, \tag{3.17}$$

$$j_{\mathrm{HCOOH}} = 2e\rho r_4, \tag{3.18}$$

$$j_{\mathrm{H_2}} = 2e\rho r_6, \tag{3.19}$$

$$j_{\mathrm{CO_2}} = j_{\mathrm{CO}} + j_{\mathrm{HCOOH}}, \tag{3.20}$$

$$j_{\mathrm{OH^-}} = -(j_{\mathrm{CO}} + j_{\mathrm{HCOOH}} + j_{\mathrm{H_2}}), \tag{3.21}$$

where ρ is the number density of active sites at Ag(110), and $e\rho = 0.68$ C m^{-2} is used in this model. [49]

3.2.2 Local reaction environment model

The model system is shown in Figure 3.2. The hydrodynamic boundary layer thickness at the cathode surface was determined to be 50 μm according to the diffusion-limited current of ferricyanide reduction [104]. The RP is located at $x = 0$. Outside the RP resides the boundary layer, which includes the diffuse layer and the diffusion layer. In the diffuse layer, electrostatic interactions dominate over thermal motion, breaking the electroneutrality condition. The thickness of the diffuse layer is generally lower than 10 nm, which is three orders of magnitude smaller than that of the diffusion layer.

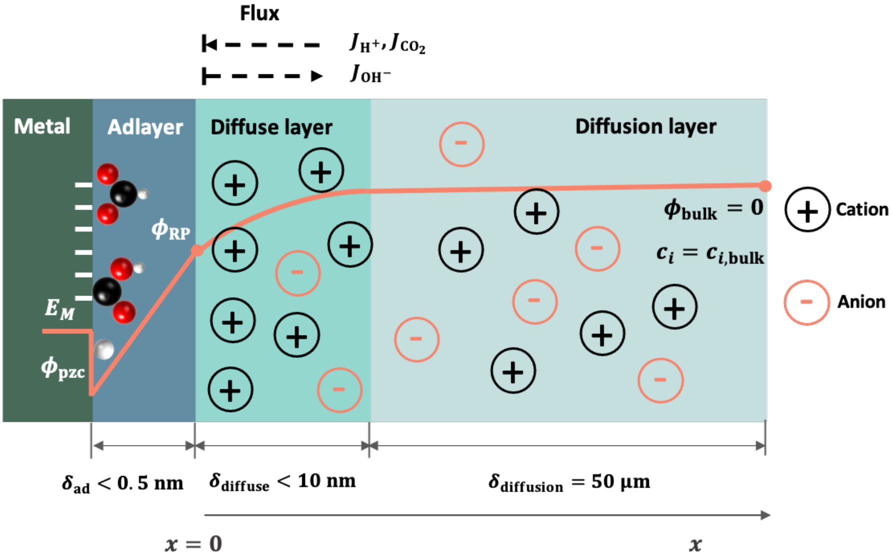

Figure 3.2: Schematic illustration of the model system. Three zones in the EDL are distinguished: the adlayer, the diffuse layer and the diffusion layer. The orange line is an illustrative potential profile for the case of negative surface charge, with ϕ_{pzc} and ϕ_{bulk} the potential of zero charge and the bulk potential, respectively. δ_{ad}, δ_{diffuse} and $\delta_{\text{diffusion}}$ are the thicknesses of the adsorbate layer, diffuse layer and diffusion layer, respectively. Fluxes at the reaction plane are indicated.

The multicomponent mass transport including CO_2, HCO_3^-, CO_3^{2-}, OH^-, H^+, and K^+ are considered. The transport of species in the boundary layer is described by a simplified version of the modified PNP theory, namely, Eq. (2.44). The simplified version takes into account steric effects but neglects water polarization,

$$\begin{aligned} &\frac{\partial}{\partial x}\left(\epsilon_s \frac{\partial \phi}{\partial x}\right) = -F\sum z_\alpha c_\alpha, \\ &J_\alpha = -D_\alpha\left(\nabla c_\alpha + c_\alpha z_\alpha \beta e_0 \nabla\phi + c_\alpha \gamma_\alpha \frac{\sum_{i\neq s} d_i^3 N_A \nabla c_i}{1-\sum_{i\neq s} d_i^3 N_A c_i}\right), \\ &\frac{\partial c_\alpha}{\partial t} = -\nabla\cdot J_\alpha + R_\alpha, \end{aligned} \tag{3.22}$$

where R_α is the rate of production of species α due to homogeneous reactions. The following homogeneous reactions in the solution are considered,

$$\mathrm{CO_2 + OH^- \rightleftharpoons HCO_3^-} \quad \text{(Step R1)}$$

$$\mathrm{HCO_3^- + OH^- \rightleftharpoons CO_3^{2-} + H_2O} \quad \text{(Step R2)}$$

$$\mathrm{OH^- + H^+ \rightleftharpoons H_2O} \quad \text{(Step R3)}$$

The expressions for R_α are written as,

$$R_{\mathrm{CO_2}} = -k_{R1} c_{\mathrm{CO_2}} c_{\mathrm{OH^-}} + k_{-R1} c_{\mathrm{HCO_3^-}}, \tag{3.23}$$

$$R_{\mathrm{HCO_3^-}} = k_{R1} c_{\mathrm{CO_2}} c_{\mathrm{OH^-}} - k_{-R1} c_{\mathrm{HCO_3^-}} - k_{R2} c_{\mathrm{HCO_3^-}} c_{\mathrm{OH^-}} + k_{-R2} c_{\mathrm{CO_3^{2-}}}, \tag{3.24}$$

$$R_{\mathrm{CO_3^{2-}}} = k_{R2} c_{\mathrm{HCO_3^-}} c_{\mathrm{OH^-}} - k_{-R2} c_{\mathrm{CO_3^{2-}}}, \tag{3.25}$$

$$R_{\mathrm{OH^-}} = -k_{R1} c_{\mathrm{CO_2}} c_{\mathrm{OH^-}} + k_{-R1} c_{\mathrm{HCO_3^-}} - k_{R2} c_{\mathrm{HCO_3^-}} c_{\mathrm{OH^-}} + k_{-R2} c_{\mathrm{CO_3^{2-}}} - k_{R3} c_{\mathrm{OH^-}} c_{\mathrm{H^+}} + k_{-R3}, \tag{3.26}$$

$$R_{\mathrm{H^+}} = -k_{R3} c_{\mathrm{OH^-}} c_{\mathrm{H^+}} + k_{-R3}, \tag{3.27}$$

$$R_{\mathrm{K^+}} = 0. \tag{3.28}$$

with $k_{\pm Ri}$ being the rate constants of the homogeneous reactions.

In this work, the steady-state approximation is used, namely, $\frac{\partial c_\alpha}{\partial t} = 0$. Additionally, only the size asymmetry of K^+ is considered because the metal is negatively charged and K^+ is the counterion in the EDL. For other species, $\gamma_\alpha = 1$. The boundary conditions are given by Eq. (2.55) and (2.56). The dipole moment of COOH$_{\mathrm{ad}}$ can be neglected because $\theta_{\mathrm{COOH_{ad}}} \approx 0$.

3.2.3 Model parameterization

The model is parameterized in this section. Parameters of the microkinetic model are listed in Tables 3.1 and 3.2. E_1^{eq} and E_2^{eq} have been calculated using DFT calculations in ref. [104]. E_3^{eq}, E_4^{eq}, E_5^{eq}, and E_6^{eq} have been obtained from the DFT studies in ref. [76]. For the CO pathway, β_1 and β_2 are set to the common value of 0.5. The activation barrier of Step 1 in 0.1 M KHCO$_3$ (pH = 6.8) solution is determined to be 0.43 eV at -1.0 V vs. RHE [49], and thus $G_{a,1}^{\mathrm{eq}} = 0.43\,\mathrm{eV} - \beta_1 \left(-1.0 - 0.059 \times 6.8 - E_1^{\mathrm{eq}}\right)$ eV $= 0.53$ eV. The activation barrier of Step 2 is calculated to be 0.7 eV at -0.11 V vs. RHE for Ag(111) at pH = 14 [77], then $G_{a,2}^{\mathrm{eq}} = 0.7\,\mathrm{eV} - \beta_2\left(-0.11 - 0.059 \times 14 - E_2^{\mathrm{eq}}\right)$ eV $= 1.4$ eV.

There is little information for the HCOOH pathway at Ag, because HCOOH is only a side product. Therefore, $G_{a,3}^{\mathrm{eq}}$ and $G_{a,4}^{\mathrm{eq}}$, β_3 and β_4 are fitted from the experimental data.

For the H_2 pathway, DFT results show the activation barriers of the Volmer step and the Heyrovsky step as 0.52 eV and 0.72 eV at -1.0 V vs. RHE at pH = 6.8 [49], then $G_{a,5}^{\mathrm{eq}} = 1.01$ eV and $G_{a,6}^{\mathrm{eq}} = 1.27$ eV. β_5 and β_6 are fitted to 0.5 and 0.3, respectively.

Table 3.1: Reaction parameters used in the model, including the standard equilibrium potential, E_i^{eq}, the activation energy, $G_{a,i}^{\mathrm{eq}}$, and the transfer coefficient, β_i, of step i

Step i	ΔG_i^0 (eV)	E_i^{eq} (V SHE)	$G_{a,i}^{\mathrm{eq}}$ (eV)	β_i
1	$\Delta G^0_{\mathrm{COOH_{ad}}} - \Delta G^0_{\mathrm{CO_2}}$	-1.223	0.5310	0.5
2	$\Delta G^0_{\mathrm{CO_{ad}+H_2O}} - \Delta G^0_{\mathrm{COOH_{ad}}}$	0.523	1.411	0.5
3	$\Delta G^0_{\mathrm{HCOO_{ad}}} - \Delta G^0_{\mathrm{CO_2}}$	0.2222	1.15	0.4
4	$\Delta G^0_{\mathrm{HCOOH}} - \Delta G^0_{\mathrm{HCOO_{ad}}}$	-0.5422	1.04	0.3
5	$\Delta G^0_{\mathrm{H_{ad}}}$	-0.4422	1.1510	0.5
6	$-\Delta G^0_{\mathrm{H_{ad}}}$	0.4422	1.3110	0.3

The lateral interaction coefficients $\xi_{\mathrm{HCOO_{ad},COOH_{ad}}}$, $\xi_{\mathrm{HCOO_{ad},HCOO_{ad}}}$, $\xi_{\mathrm{HCOO_{ad},H_{ad}}}$, and $\xi_{\mathrm{H_{ad},COOH_{ad}}}$ have been taken from ref. [76], assuming that the changes in binding energies due to lateral interactions are linearly related to the coverages. $\xi_{\mathrm{H_{ad},HCOO_{ad}}}$ and $\xi_{\mathrm{H_{ad},H_{ad}}}$ are fitting parameters.

Table 3.2: Lateral interaction coefficients, $\xi_{\mathrm{X}_j,\mathrm{X}_i}$ (eV)

	$\mathrm{HCOO_{ad}}$	$\mathrm{H_{ad}}$
$\mathrm{COOH_{ad}}$	0.2	1.2
$\mathrm{HCOO_{ad}}$	0.5	0.4
$\mathrm{H_{ad}}$	0.45	0.37

The energetic parameters are allowed to vary within 0.2 eV around their base values, considering the uncertainty associated with DFT calculations of reaction and transition-state energies [114]. Sensitivity analyses of fitting parameters, $G^{eq}_{a,3}$, $G^{eq}_{a,4}$, $\xi_{H_{ad},HCOO_{ad}}$, $\xi_{H_{ad},H_{ad}}$, β_1, β_2, β_3, β_4, β_5, and β_6, are thus provided. To perform these analyses, I have varied the values of specific parameters in their feasible ranges while keeping all other parameters constant, and then calculated the partial current densities at $E_M = -1.2\,V$ and pH = 6.8.

The surface charging and mass transport effects are neglected here, and I focus on intrinsic kinetics. That is to say, I use $\phi_{RP} = 0$, and $c_\alpha = c_{\alpha,bulk}$. The performance of a specific pathway is controlled by two sequential steps. Therefore, $G^{eq}_{a,3}$ and $G^{eq}_{a,4}$ for the HCOOH pathway, β_1 and β_2 for the CO pathway, β_3 and β_4 for the HCOOH pathway, and β_5 and β_6 for the H_2 pathway are analyzed jointly. The results are shown below. The high sensitivity of the model performance to these parameters implies a high confidence in the fitted parameters.

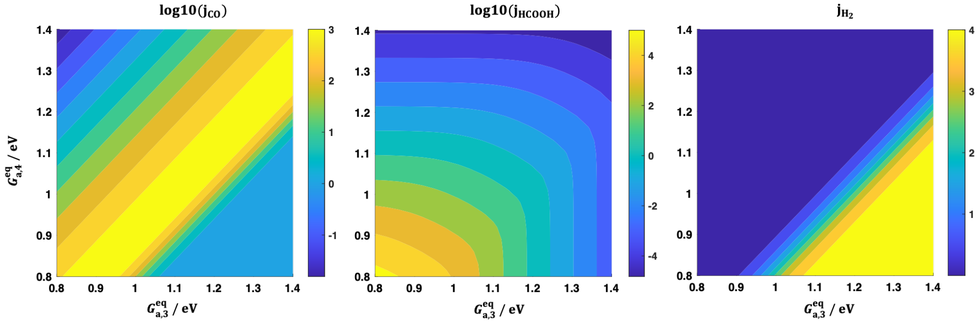

Figure 3.3: Parameter sensitivity analysis of $G^{eq}_{a,3}$ and $G^{eq}_{a,4}$.

As shown in Figure 3.3, the highest j_{CO} is obtained around $G^{eq}_{a,3} = G^{eq}_{a,4}$. When $G^{eq}_{a,3} < G^{eq}_{a,4}$, $\theta_{HCOO_{ad}}$ increases because the adsorption of $HCOO_{ad}$ is strengthened. Then j_{CO} decreases due to the site-blocking effect of $HCOO_{ad}$. On the contrary, $\theta_{HCOO_{ad}}$ decreases when $G^{eq}_{a,3} > G^{eq}_{a,4}$. However, j_{CO} also decreases in this case. This is because the adsorption of H_{ad} is promoted at the same time, which inhibits $COOH_{ad}$ adsorption even more severely than $HCOO_{ad}$ through lateral interactions. [76] The analysis reveals that, albeit being a minor product, $HCOO_{ad}$ plays an important role in the CO_2RR on Ag. j_{HCOOH} increases with decreasing $G^{eq}_{a,3}$ as the adsorption of $HCOO_{ad}$ is strengthened, or with decreasing $G^{eq}_{a,4}$ as the desorption of $HCOO_{ad}$ is promoted. j_{H_2} increases with increasing $G^{eq}_{a,3}$ because the adsorption of $HCOO_{ad}$ is weakened, or with decreasing $G^{eq}_{a,4}$ as the desorption of $HCOO_{ad}$ is promoted. The adsorption of H_{ad} is enhanced in both cases.

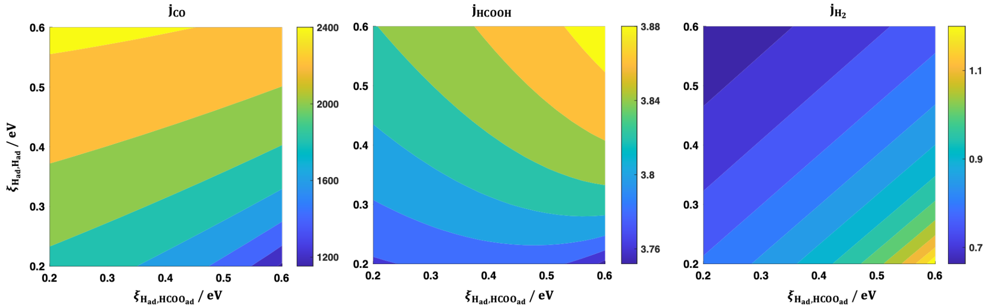

Figure 3.4: Parameter sensitivity analysis of $\xi_{H_{ad},H_{ad}}$ and $\xi_{H_{ad},HCOO_{ad}}$.

j_{CO} increases monotonically as $\xi_{H_{ad},H_{ad}}$ increases or $\xi_{H_{ad},HCOO_{ad}}$ decreases, as shown in Figure 3.4. Due to the lateral interactions, a larger $\xi_{H_{ad},H_{ad}}$ reduces H_{ad} adsorption, and a smaller $\xi_{H_{ad},HCOO_{ad}}$ promotes $HCOO_{ad}$ adsorption, which in turn inhibits H_{ad} adsorption. $\theta_{H_{ad}}$ decreases in both cases, and j_{CO} increases as a result because the adsorption of $COOH_{ad}$ is improved. j_{HCOOH} and j_{H_2} are less sensitive to $\xi_{H_{ad},H_{ad}}$ and $\xi_{H_{ad},HCOO_{ad}}$.

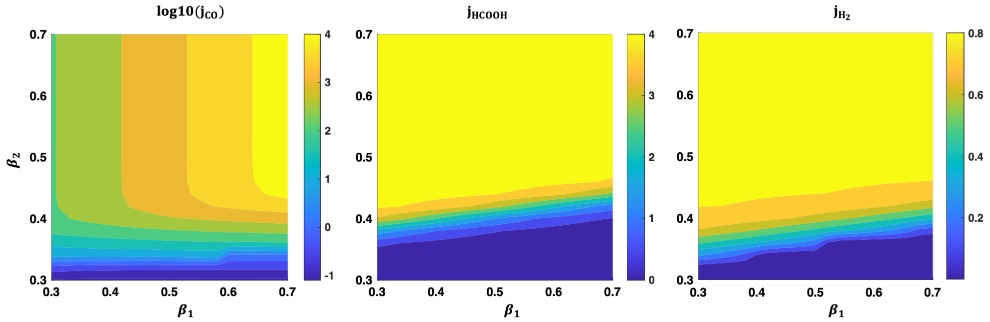

Figure 3.5: Parameter sensitivity analysis of β_1 and β_2.

Figure 3.5 shows the sensitivity of the transfer coefficients of the CO pathway. j_{CO} is very sensitive to β_1 and β_2, and increases with increasing β_1 and β_2. When $\beta_2 > 0.45$, the desorption of $COOH_{ad}$ is much faster than its adsorption, leading to very low $COOH_{ad}$ coverage. Thus, j_{HCOOH} and j_{H_2} are not sensitive to β_1 and β_2 in this case.

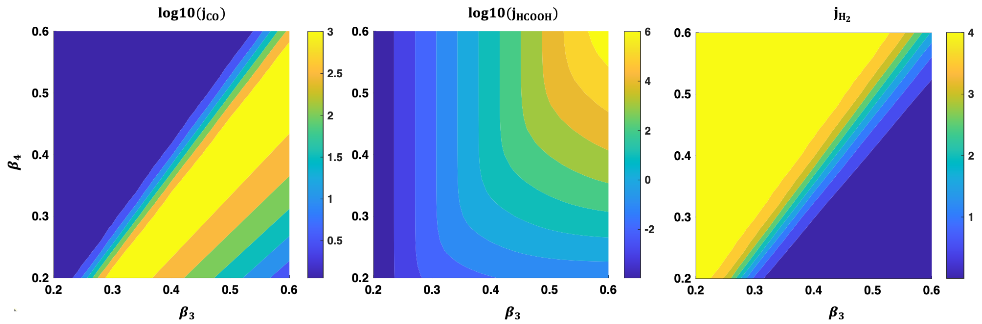

Figure 3.6: Parameter sensitivity analysis of β_3 and β_4.

Figure 3.6 shows the sensitivity of the transfer coefficients of the HCOOH pathway. j_{HCOOH} is very sensitive to β_3 and β_4, and increases with increasing β_3 and β_4. j_{CO} is also very sensitive to β_3 and β_4, and the highest j_{CO} is obtained around $\beta_3 = \beta_4$. $j_{\mathrm{H_2}}$ increases with decreasing β_3 or increasing β_4.

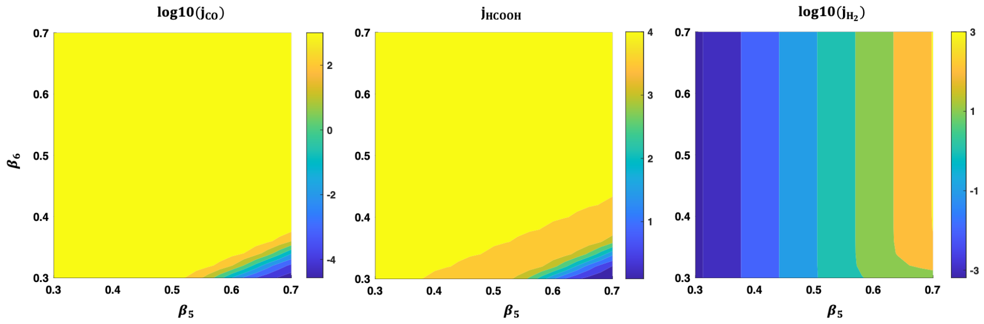

Figure 3.7: Parameter sensitivity analysis of β_5 and β_6.

Figure 3.7 shows the sensitivity of the transfer coefficients of the H_2 pathway. When $\beta_6 > 0.45$ or $\beta_5 < 0.4$, the desorption of H_{ad} is very fast compared with its adsorption, resulting in $\theta_{\mathrm{H_{ad}}} \approx 0$. In this case, j_{CO} and j_{HCOOH} are always located in the optimal region and independent of β_5 and β_6. Otherwise, j_{CO} and j_{HCOOH} increase with decreasing β_5 or increasing β_6. $j_{\mathrm{H_2}}$ increases with increasing β_5 or increasing β_6. However, $j_{\mathrm{H_2}}$ is not sensitive to β_6 when $\beta_6 > 0.4$, as the adsorption of H_{ad} is rate-limiting for the H_2 pathway in this situation.

The detailed parameters for the LRE model, including the parameters for the EDL and the parameters for the mass transport, are summarized in Tables 3.3, 3.4, and 3.5, including the sources that they have been extracted from.

With these parameters, the model was solved iteratively. Given the initial current densities and coverages at a specific applied potential, the potential distribution and concentration distributions in the solution phase can be obtained from the LRE model. The calculated potential and reactant concentrations at the RP are then used in the microkinetic model to calculate new values of current densities and coverages. The cycle iterates until the current densities are converged, with the criterion of relative error convergence being 1×10^{-3}.

Table 3.3: Parameters of the EDL

Item	**Category**	**Value**	**Note**
$HCOO_{ad}$	Net charge number per adsorbate	0.68	Ref. [76]
H_{ad}	Net charge number per adsorbate	0.25	Ref. [76]
ϕ_{pzc}	Potential of zero charge	-0.73 V (SHE)	Ref. [104]
ϵ_s	Permittivity of the electrolyte solution	$78.5\epsilon_0$	ϵ_0 is the permittivity of vacuum
ϵ_{ad}	Permittivity of the adlayer	$6\epsilon_0$	Ref. [115]
δ_{ad}	Thickness of the space between the metal surface and the adsorbate layer	0.2 nm	Bond length of Pt-OH_{ad} [116]

Table 3.4: Rate constants of homogeneous reactions

Reaction	Forward rate constant [11, 102]	Reverse rate constant [11, 102]
Step R1	5.93×10^3	1.28×10^{-4}
Step R2	1×10^8	2.03×10^4
Step R3	2.4×10^9	2.4×10^{-5}

Table 3.5: Parameters for the mass transport, including bulk concentrations, diffusion coefficients, effective solvated diameters, and rate constants of homogeneous reactions

Category	Item	Value
$c_{\alpha,\mathrm{bulk}}$ (M)[103]	CO_2	0.0342
	HCO_3^-	0.0999
	CO_3^{2-}	3.1×10^{-5}
	OH^-	6.31×10^{-8}
	H^+	1.58×10^{-7}
	K^+	0.1
D_α (m^2/s)[102, 103]	CO_2	1.91×10^{-9}
	HCO_3^-	1.185×10^{-9}
	CO_3^{2-}	0.923×10^{-9}
	OH^-	5.723×10^{-9}
	H^+	9.311×10^{-9}
	K^+	1.957×10^{-9}
	Na^+	1.334×10^{-9}
	Li^+	1.029×10^{-9}
d_α (m) [117]	K^+	0.662×10^{-9}
	Na^+	0.716×10^{-9}
	Li^+	0.764×10^{-9}

3.3 Revealing the impact of the local reaction environment

In what follows, I first validate the model by comparing simulation results with experimental data. A detailed mechanistic analyses of the bell-shaped polarization curve and the origins of potential dependencies in Tafel slopes are then presented.

3.3.1 Model-experiment comparison

Figure 3.8 shows the simulated CO partial current density in the potential range between -0.3 V and -1.4 V. Experimental data from Clark *et al.*,[104] Hoshi *et al.*,[105] Hatsukade *et al.*,[107] and Singh *et al.*[54] are closely reproduced by this model. The experimentally observed increasing Tafel slope with overpotential is captured. Specifically, the CO partial current density increases with overpotential when $E_\mathrm{M} > -1.25$ V, and decreases when $E_\mathrm{M} < -1.25$ V, resulting in the peculiar bell shape. A mechanistic explanation of the bell shape is to be given in the following section.

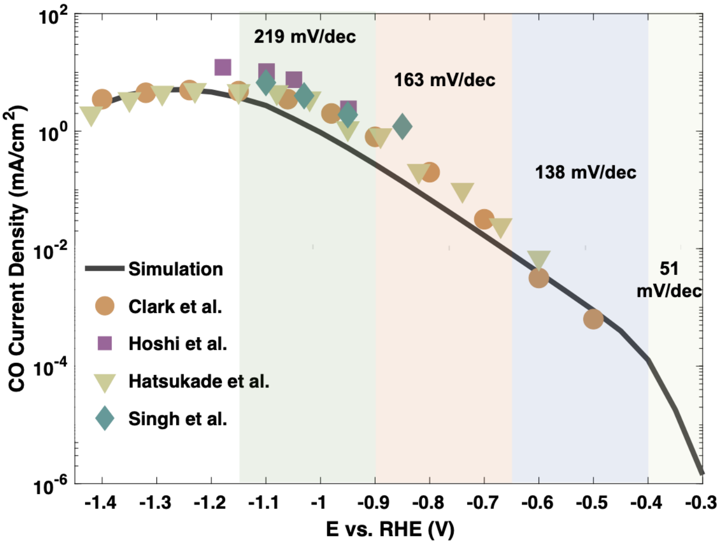

Figure 3.8: Model–experiment comparison in terms of the CO partial current density. The experimental data are obtained on Ag in 0.1 M $KHCO_3$. The Tafel slopes were calculated in different potential ranges as marked by different background colors.

I also reproduced the partial current densities of HCOOH and H_2, as shown in Figure 3.9. The excellent agreement between the model and experimental data for different reaction products demonstrates the reliability of this model.

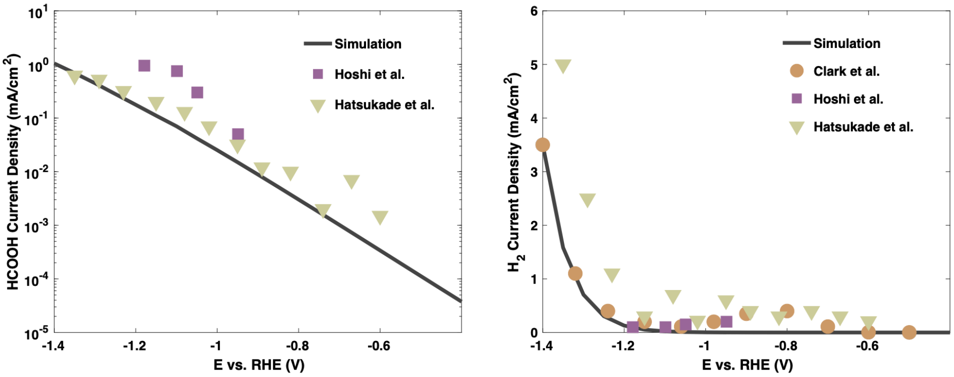

Figure 3.9: Model-experiment comparison in terms of HCOOH partial current density and H_2 partial current density.

3.3.2 Origins of the bell-shaped curve

The maximum current density is only about 5 mA/cm^2 at $E_\mathrm{M} = -1.25$ V, which is significantly smaller than the diffusion-limited current density that is estimated as $\sim$20 mA/cm^2 using the mass transport model.[49] As shown in Figure 3.10(a), the partial current density of CO_2, $j_{\mathrm{CO_2}} = j_\mathrm{CO} + j_\mathrm{HCOOH}$, decreases at high overpotentials, implying that the decreasing trend cannot be explained by the increasing consumption rate of CO_2.

Analysis according to the microkinetic model yields

$$\theta_{\mathrm{COOH_{ad}}} = \frac{k_1 c^{\mathrm{RP}}_{\mathrm{CO_2}} \theta_0}{k_{-1} c^{\mathrm{RP}}_{\mathrm{OH^-}} + k_2}, \tag{3.29}$$

$$\frac{1}{\mathrm{TOF}} = \frac{1}{k_2 \theta_{\mathrm{COOH_{ad}}}} = \frac{1}{k_1 c^{\mathrm{RP}}_{\mathrm{CO_2}} \theta_0} + \frac{c^{\mathrm{OHP}}_{\mathrm{OH^-}}}{K_1 k_2 c^{\mathrm{RP}}_{\mathrm{CO_2}} \theta_0}, \tag{3.30}$$

with $K_1 = k_1/k_{-1}$ being the equilibrium constant of Step 1. 1/TOF represents the effective resistance of CO_2RR to CO, which consists of two terms. Therefore, the activity of CO_2RR to CO can be represented as a series of resistances. In the context of a serial resistor network, the notion of RDT becomes meaningful (Eq. (2.13)).

As shown in Figure 3.10(b), $\frac{c^{\mathrm{RP}}_{\mathrm{OH^-}}}{K_1 k_2 c^{\mathrm{RP}}_{\mathrm{CO_2}} \theta_0}$ is the RDT when $E_\mathrm{M} > -0.5$ V, and $\frac{1}{k_1 c^{\mathrm{RP}}_{\mathrm{CO_2}} \theta_0}$ is the RDT when $E_\mathrm{M} < -0.5$ V. Therefore, the increasing current density at $E_\mathrm{M} > -0.5$ V is due to the decrease of $\frac{c_{\mathrm{OH^-}}^{\mathrm{RP}}}{K_1 k_2 c_{\mathrm{CO_2}}^{\mathrm{RP}} \theta_0} \cdot \frac{1}{k_1 c_{\mathrm{CO_2}}^{\mathrm{RP}} \theta_0}$ decreases with overpotential when -1.25 V $< E_{\mathrm{M}} < -0.5$ V and increases when $E_{\mathrm{M}} < -1.25$ V, resulting in the nonmonotonic current density. To understand the nonmonotonic behavior, the potential dependence of k_1, K_1, k_2, $c_{\mathrm{CO_2}}^{\mathrm{RP}}$, $c_{\mathrm{OH^-}}^{\mathrm{RP}}$ and θ_0 need to be analyzed.

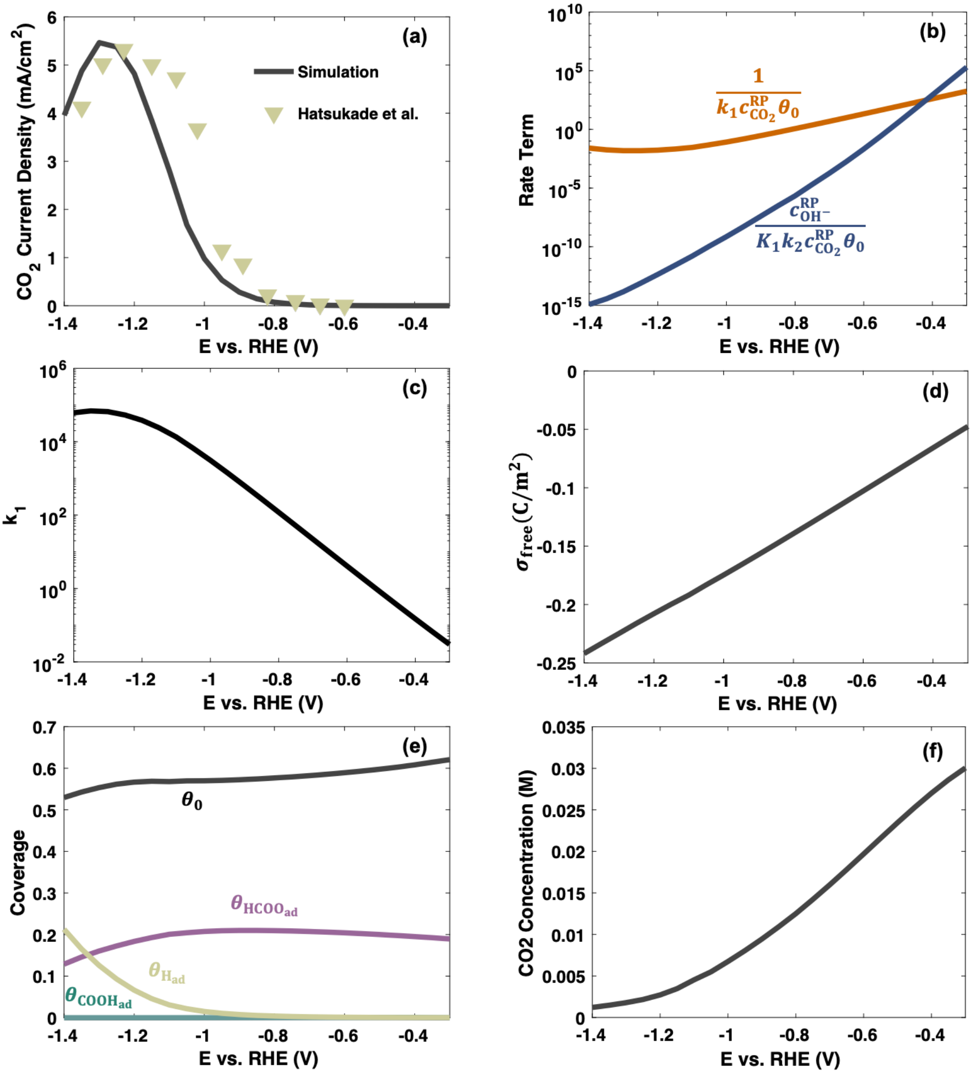

Figure 3.10: (a) Model-experiment comparison in terms of the CO$_2$ partial current density. (b) Rate-determining terms of the CO partial current density. (c) Forward rate constant of Step 1, k_1. (d) Surface charging relation. (e) Coverages of COOH$_{\mathrm{ad}}$, HCOO$_{\mathrm{ad}}$, H$_{\mathrm{ad}}$ and free sites. (f) CO$_2$ concentration at the RP.

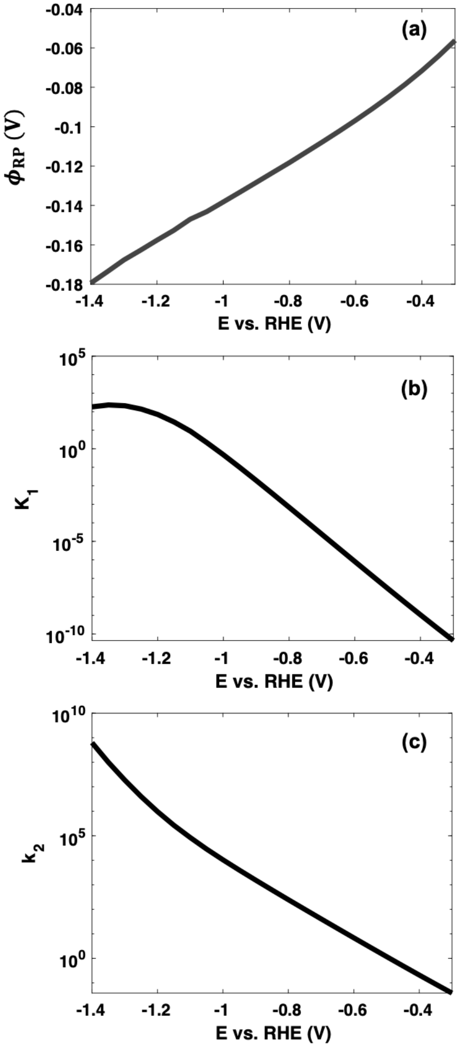

Figure 3.11: (a) Simulated potential at the RP as a function of electrode potential. (b) Equilibrium constant of Step 1, K_1. (c) Forward rate constant of Step 2, k_2.

As shown in Figure 3.10(c), k_1 deviates from the Tafel equation, $k_i = k_i^0 \exp\left(-\frac{\beta_i F E}{RT}\right)$. Two factors are responsible for this deviation: the surface charging effects and lateral adsorbate-adsorbate interactions. ϕ_{RP} is negative due to negative σ_{free} (Figure 3.10(d)), and decreases with overpotential following the surface charging relation, as presented in Figure 3.11(a). Consequently, the driving force of interfacial charge transfer, defined as $-(E_{\mathrm{M}} - \phi_{\mathrm{RP}} - E_i^{\mathrm{eq}})$, is lower than $-(E_{\mathrm{M}} - E_i^{\mathrm{eq}})$. This effect is essentially a Frumkin correction. DFT calculations have shown that H_{ad} repels $COOH_{ad}$ more than $HCOO_{ad}$.[76] With increasing overpotential, $HCOO_{ad}$ is replaced by H_{ad} (Figure 3.10(e)), inhibiting the formation of $COOH_{ad}$ to a greater extent. When $E_M < -1.25$ V, $G_{a,1}$ increases anomalously with overpotential because ΔG_1 increases due to lateral adsorbate interactions (Eq. (3.10)), resulting in the decrease of k_1. K_1 and k_2 increase monotonically when $E_M > -0.5$ V, as shown in Figure 3.11(b) and Figure 3.11(c).

As shown in Figure 3.10(e), $\theta_{HCOO_{ad}}$ is dominant over $\theta_{COOH_{ad}}$ and $\theta_{H_{ad}}$ when $E_M > -1.1$ V, and decreases with overpotential. $\theta_{COOH_{ad}}$ is nearly zero in the whole potential range. In addition, $\theta_{HCOO_{ad}} \approx 0$ when $E_M > -1.1$ V and $\theta_{H_{ad}}$ increases with overpotential. θ_0 remains almost constant due to the balance between $\theta_{HCOO_{ad}}$ and $\theta_{H_{ad}}$.

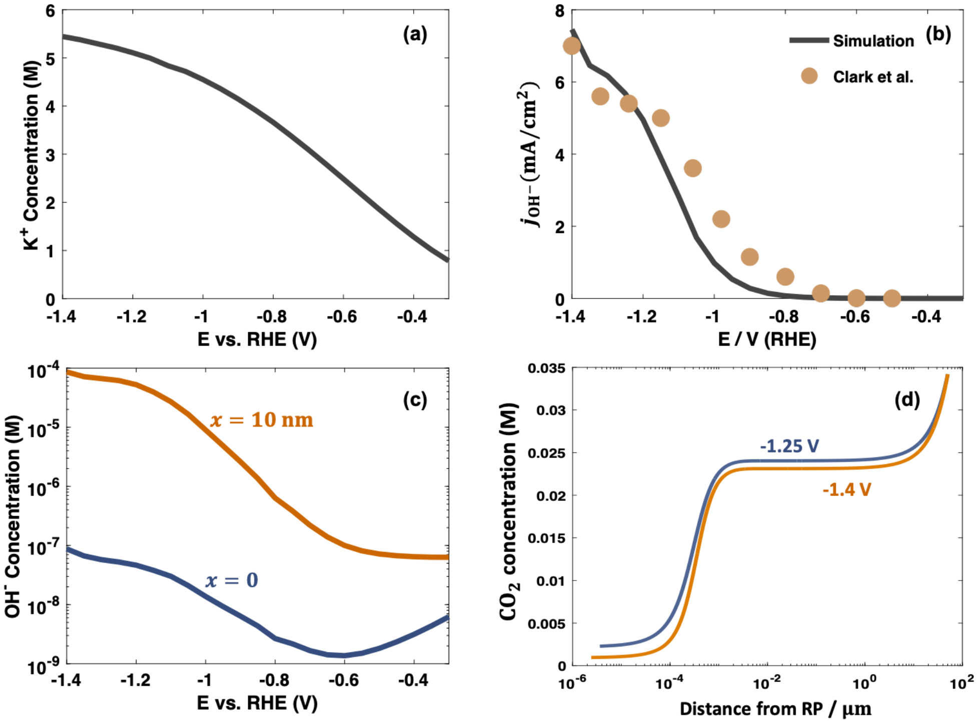

Figure 3.12: (a) K^+ concentration at the RP. (b) Partial current density of OH^-. (c) OH^- contration at $x = 0$ (RP) and $x = 10$ nm. (d) Distribution of c_{CO_2} at -1.25 V and -1.4 V by using experimental current densities to calculate fluxes.

$c^{RP}_{CO_2}$ decreases monotonically with overpotential, as shown in Figure 3.10(f). It should be noted that $c^{RP}_{CO_2}$ is influenced not only by the mass transport of CO_2, but also by the surface charge density. The magnitude of negative σ_{free} increases with overpotential (Figure 3.10(d)). Therefore, the concentration of K^+ at the RP dramatically increases due to electrostatic attraction (Figure 3.12(a)). K^+ occupies most of the space near the electrode surface, thus repelling CO_2.[11] $c^{\text{RP}}_{\text{OH}^-}$ decreases slowly for $E_{\text{M}} > -0.6$ V due to the electrostatic repulsion; it increases for $E_{\text{M}} < -0.6$ V due to the increasing generation rate of OH^- (see j_{OH^-} in Figure 3.12(b)), as shown in Figure 3.12(c). It should be noted that the increase in $c^{\text{RP}}_{\text{OH}^-}$ also decreases $c^{\text{RP}}_{\text{CO}_2}$ through the homogeneous reaction in Steps R1-R3.

Combined, when $E_{\text{M}} > -0.5$ V, $c^{\text{RP}}_{\text{CO}_2}$, $c^{\text{RP}}_{\text{OH}^-}$, and θ_0 remain nearly constant, the dominant term in $\frac{c^{\text{RP}}_{\text{OH}^-}}{K_1 k_2 c^{\text{RP}}_{\text{CO}_2} \theta_0}$ is $K_1 k_2$, which increases monotonically with overpotential, leading to the decrease of $\frac{c^{\text{RP}}_{\text{OH}^-}}{K_1 k_2 c^{\text{RP}}_{\text{CO}_2} \theta_0}$; When $-1.25\text{ V} < E_{\text{M}} < -0.5$ V, the increase of k_1 dominates over the decrease of $c^{\text{RP}}_{\text{CO}_2}$, causing the decrease of $\frac{1}{k_1 c^{\text{RP}}_{\text{CO}_2} \theta_0}$; When $E_{\text{M}} < -1.25$ V, both k_1 and $c^{\text{RP}}_{\text{CO}_2}$ decrease, resulting in the increase of $\frac{1}{k_1 c^{\text{RP}}_{\text{CO}_2} \theta_0}$.

In conclusion, the activity of the CO_2RR to CO is not only determined by the intrinsic kinetics that increases monotonically with overpotential, but also by the LRE. The LRE is determined by the interplay between the mass transport effects that decrease the CO_2 concentration in the RP, the surface charging effects that decrease the driving force of interfacial charge transfer and block CO_2 transport, and the lateral interactions between adsorbates that inhibit the adsorption of COOH_{ad}. Specifically, the intrinsic kinetics dominates when $E_{\text{M}} > -1.25$ V, resulting in the decrease of $\frac{c^{\text{RP}}_{\text{OH}^-}}{K_1 k_2 c^{\text{RP}}_{\text{CO}_2} \theta_0}$ and $\frac{1}{k_1 c^{\text{RP}}_{\text{CO}_2} \theta_0}$. As a result, the CO current density increases with overpotential in this potential range. When $-1.4\text{ V} < E_{\text{M}} < -1.25$ V, $c^{\text{RP}}_{\text{CO}_2}$ decreases, and the repulsive effect on COOH_{ad} from lateral interactions becomes stronger, causing the anomalous decrease of the CO current density.

It has been proposed that the decrease of j_{CO} on Ag is mainly caused by the enhanced rate of hydrogen evolution, which generates OH^- and thus decreases the CO_2 concentration.[118] The distributions of c_{CO_2} at -1.25 V and -1.4 V by using experimental current densities in ref. [104] as fluxes are compared (Figure 3.12(d)). It can be seen that $c^{\text{RP}}_{\text{CO}_2}$ at -1.4 V is about 40% of $c^{\text{RP}}_{\text{CO}_2}$ at -1.25 V.

If the lateral interactions are neglected, k_1 at -1.25 V should be only about 5% of k_1 at -1.4 V according to the Butler-Volmer equation. Based on this assessment, it is expected that $k_1 c^{\mathrm{RP}}_{\mathrm{CO_2}}$ increases with overpotential. Therefore, only considering the decrease of CO_2 concentration is insufficient to rationalize the decrease of j_{CO} with increasing overpotential, bringing into play lateral interactions as another possible (and, in my understanding, likely) origin of the observed trend.

In this context, it should be noted that $HCOO_{\mathrm{ad}}$ was detected by surface-enhanced Raman spectroscopy,[76] whereas, interestingly, H_{ad} was detected by infrared spectroscopy in the absence of CO_2 and disappeared when CO_2 was introduced.[112] Furthermore, it was observed that the HER was severely suppressed in CO_2-saturated solution.[104] These observations together suggest a significant impact of interactions between adsorbates.

3.3.3 Origin of the potential-dependent Tafel slope

As shown in Figure 3.10, the model gives $b = 51$ mV/dec (close to 59 mV/dec) when $E_{\mathrm{M}} > -0.4$ V, and $b > 118$ mV/dec when $-0.4\ \mathrm{V} > E_{\mathrm{M}} > -1.2$ V, consistent with experimental measurements on bulk Ag,[25] nanostructured Ag,[96] polycrystalline Au,[108] and oxide-derived Au.[119] To explain the potential-dependent Tafel slope, I first explore the intrinsic kinetics of the CO pathway. That means that I neglect for the moment the competitive reactions, mass transport, and surface charging effects. In this case, the analytical expression for $\theta_{\mathrm{COOH_{ad}}}$ can be obtained as,

$$\theta_{\mathrm{COOH_{ad}}} = \frac{k_1 c_{\mathrm{CO_2}}}{k_1 c_{\mathrm{CO_2}} + k_{-1} c_{\mathrm{OH^-}} + k_2}. \tag{3.31}$$

Then,

$$\frac{1}{\mathrm{TOF}} = \frac{1}{k_2 \theta_{\mathrm{COOH_{ad}}}} = \frac{1}{k_2} + \frac{1}{k_1 c_{\mathrm{CO_2}}} + \frac{1}{K_1 k_2} \frac{c_{\mathrm{OH^-}}}{c_{\mathrm{CO_2}}}. \tag{3.32}$$

Figure 3.13(a) displays the RDTs as a function of potential. When $E_{\mathrm{M}} > -0.4$ V, $\frac{1}{K_1 k_2} \frac{c_{\mathrm{OH^-}}}{c_{\mathrm{CO_2}}}$ is the RDT, and $b = \frac{2.3RT}{(1+\beta_2)F} = 39$ mV/dec, as shown in Figure 3.13(b). When $E_{\mathrm{M}} < -0.4$ V, $\frac{1}{k_1 c_{\mathrm{CO_2}}}$ is the RDT, and $b = \frac{2.3RT}{\beta_1 F} = 118$ mV/dec. A more general analysis of the Tafel slope of multi-electron reactions can be found in ref. [48].

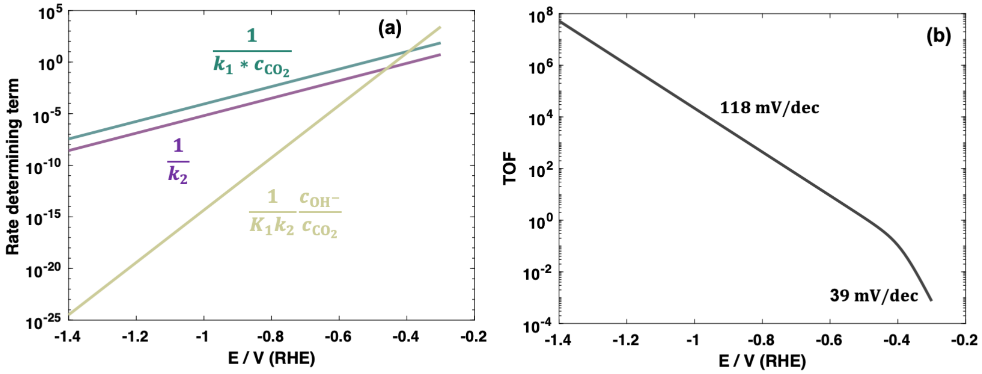

Figure 3.13: (a) Rate determining terms and (b) intrinsic activity-potential relation of the CO$_2$RR to CO. The LRE is not considered in the calculations, namely, $\phi_{\mathrm{RP}} = 0$, $c_i^{\mathrm{RP}} = c_i^{\mathrm{bulk}}$.

Starting from the intrinsic Tafel slopes shown in Figure 3.13(b), I add complexity to the analysis by considering the impact of the LRE. When -1.25 V $< E_{\mathrm{M}} < -0.4$ V, both $j_{\mathrm{CO_2}}$ and negative σ_{free} increase with increasing overpotential, as shown in Figure 3.11(a) and (d), leading to $b > 118$ mV/dec. When $E_{\mathrm{M}} > -0.4$ V, $j_{\mathrm{CO_2}}$ is very small and $\theta_{\mathrm{HCOO_{ad}}}$, $\theta_{\mathrm{H_{ad}}}$, and θ_0 remain almost constant, Figure 3.11(a) and (e), indicating that the competitive reactions and mass transport effects are unimportant in this potential range. Instead, the primary factor controlling the Tafel slope is the surface charging relation, which decreases the driving force and $c_{\mathrm{CO_2}}^{\mathrm{RP}}$. Thus, the Tafel slope increases from 39 mV/dec to 51 mV/dec (close to 59 mV/dec). It should be noted that 39 mV/dec and 59 mV/dec refer to different rate-determining steps in the Tafel analysis. Consequently, it is necessary to consider the LRE when deciphering the reaction mechanisms with Tafel analysis.

3.4 Tuning the local reaction environment

In this section, I demonstrate how the local reaction environment can be tuned by varying the bicarbonate concentration, the type of electrolyte cations, and the CO$_2$ pressure.

3.4.1 Role of bicarbonate

The bicarbonate (HCO_3^-) is involved in the homogeneous reactions. Therefore, the LRE can be tuned by varying the concentration of HCO_3^-, $c_{HCO_3^-}$. As the solution pH changes with $c_{HCO_3^-}$, the influence of $c_{HCO_3^-}$ is different on SHE and RHE scales.

Let us change $c_{HCO_3^-}$ from 0.05 M to 0.5 M at fixed ionic strength and K^+ concentration by adding $KClO_4$. For this case, the pH shifts from 6.5 to 7.5. If the electrode potential is referenced to the SHE scale, j_{CO} should be independent of $c_{HCO_3^-}$ when the mass transport effects are insignificant because HCO_3^- is not involved in the reaction mechanism (Steps 1-6). If the electrode potential is referenced to the RHE scale, the driving force, defined as $-(E_{M,\,SHE} - E^{eq}_{i,SHE})$, will increase by an amount of $RT \ln 10/F = 59$ mV (neglecting the surface charging effect for the moment, namely, $\phi_{RP} = 0$).

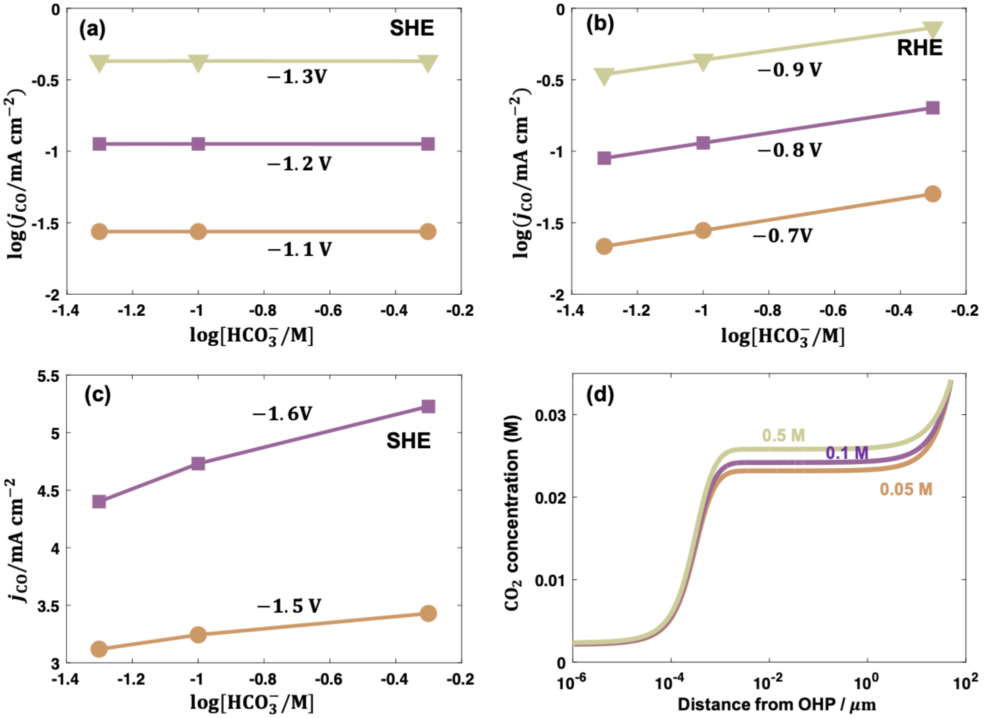

Figure 3.14: Bicarbonate concentration dependence of the CO partial current density at (a) -1.1 V, -1.2 V, -1.3 V vs. SHE, (b) at -0.7 V, -0.8 V, -0.9 V vs. RHE, and (c) at -1.5 V and -1.6 V vs. SHE. (d) Concentration distributions of CO_2 in solutions with 0.05 M, 0.1 M and 0.5 M bicarbonate at -1.6 V vs. SHE.

As discussed in the previous section, $\frac{1}{K_1 k_2}\frac{c_{\mathrm{OH^-}}}{c_{\mathrm{CO_2}}}$ is the RDT for $E_\mathrm{M} > -0.4$ V, the dependence of j_CO on bicarbonate concentration, denoted as $b_{\mathrm{HCO_3^-}}$, is 0.5; $\frac{1}{k_1 c_{\mathrm{CO_2}}}$ is the RDT for $E_\mathrm{M} < -0.4$ V, resulting also in $b_{\mathrm{HCO_3^-}} = 0.5$.

I calculate $b_{\mathrm{HCO_3^-}}$ at -1.1 V, -1.2 V, and -1.3 V vs SHE, all being 0, as shown in Figure 3.14(a). When the RHE scale is used, $b_{\mathrm{HCO_3^-}} \approx 0.4$ is obtained, regardless of the overpotential, as shown in Figure 3.14(b). $b_{\mathrm{HCO_3^-}}$ is smaller than 0.5 because σ_free becomes more negative with $c_{\mathrm{HCO_3^-}}$ due to the pH increase, and the mass transport effects grow with increasing j_CO.

In experimental studies, both $b_{\mathrm{HCO_3^-}} = 0.58$[96, 108] and $b_{\mathrm{HCO_3^-}} = 0.45$[120] have been reported, leading to different conclusions on the role of bicarbonate. Here, I clarify that the different experimental values of $b_{\mathrm{HCO_3^-}}$ are caused by the use of different potential scales. It should also be noted that $b_{\mathrm{HCO_3^-}} \approx 1$ was observed on oxide-derived Au nanoparticles,[119] and polycrystalline Au.[108] This abnormal value of $b_{\mathrm{HCO_3^-}} \approx 1$ is related to the unusual experimental conditions. In ref. [119], $b_{\mathrm{HCO_3^-}}$ is determined at potentials with severe mass transport limitations. In addition, phosphate, which has been shown to inhibit the reaction,[120] was used as a buffer to maintain the ionic strength in ref. [108].

However, the higher $c_{\mathrm{HCO_3^-}}$ can increase j_CO on the SHE scale when the mass transport effects are significant, as shown in Figure 3.14(c). This enhancement can be attributed to the buffering capacity of bicarbonate, which can maintain the local pH (Figure 3.15), and consequently increase the local CO$_2$ concentration by inhibiting the homogeneous reaction, as shown in Figure 3.14(d).

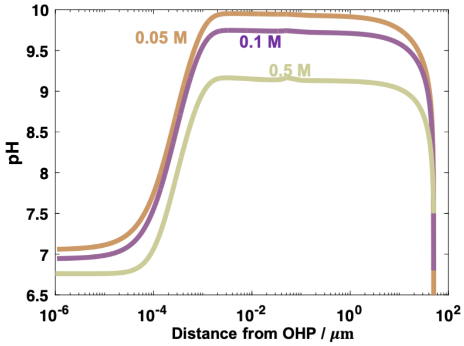

Figure 3.15: pH distribution in 0.05 M, 0.1 M and 0.5 M bicarbonate solutions at -1.6 V vs SHE.

In conclusion, $c_{\mathrm{HCO_3^-}}$ affects the LRE by changing the pH and buffering capacity of the solution. On the SHE scale, j_{CO} is independent of $c_{\mathrm{HCO_3^-}}$ when mass transport effects are insignificant since $\mathrm{HCO_3^-}$ is not the direct reactant, while it increases with $c_{\mathrm{HCO_3^-}}$ when mass transport effects are significant because of the buffering capacity of $\mathrm{HCO_3^-}$. On the RHE scale, $b_{\mathrm{HCO_3^-}} \approx 0.5$ is obtained due to the pH shift.

3.4.2 Cation effects

The LRE can also be tuned by using different electrolyte cations. For nonspecifically adsorbing cations, they are characterized by the effective size, the diffusion coefficient, and the charge number. In this section, I considered three cations, $\mathrm{K^+}$, $\mathrm{Na^+}$, and $\mathrm{Li^+}$, with $d_{\mathrm{K^+}} < d_{\mathrm{Na^+}} < d_{\mathrm{Li^+}}$, considering their solvation shells.[117] The electrolyte solutions are 0.1M $\mathrm{KHCO_3/NaHCO_3/LiHCO_3}$. As shown in Figure 3.16(a), the intensity of the steric effect of cations, $d_i^3 N_A c_i$, follows the order of $\mathrm{K^+} < \mathrm{Na^+} < \mathrm{Li^+}$, consistent with the order of solvated ion size. A larger steric effect would lead to a decreased $c_{\mathrm{CO_2}}^{\mathrm{RP}}$, as shown in Figure 3.16(b). Consequently, j_{CO} follows the order of $\mathrm{K^+} > \mathrm{Na^+} > \mathrm{Li^+}$, Figure 3.16(c), which is in line with experimental observations.[54]

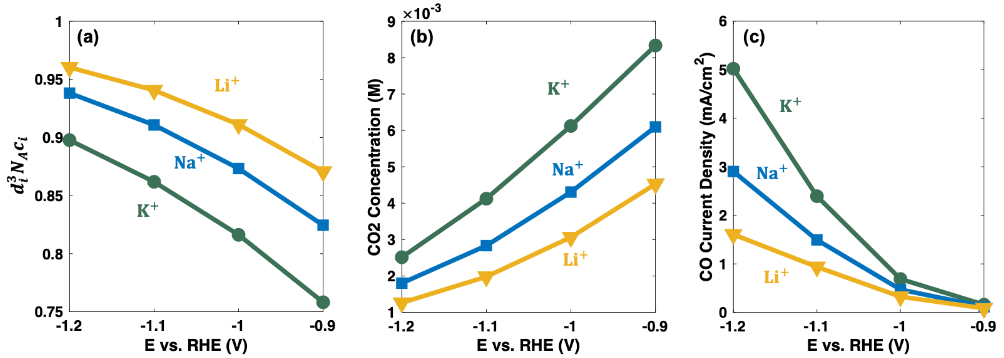

Figure 3.16: (a) Intensity of the steric effect of cations, (b) $\mathrm{CO_2}$ concentrations at RP, and (c) CO partial current densities in 0.1 M $\mathrm{KHCO_3/NaHCO_3/LiHCO_3}$ solutions.

The pH at the RP follows the order $\mathrm{K^+} > \mathrm{Na^+} > \mathrm{Li^+}$, as shown in Figure 3.17, which is consistent with results in ref. [27]. The cation size effect on j_{HCOOH} is similar to that on j_{CO}, as the two pathways share the same reactant $\mathrm{CO_2}$ (Figure 3.18). However, $j_{\mathrm{H_2}}$ is not sensitive to the cation sizes of K^+, Na^+, and Li^+ as the proton precursor is H_2O and the backward reaction of Step 5 can be neglected ($k_{-5}c^{RP}_{OH^-} \ll k_5$). The results in Figure 3.18 are in agreement with experimental results.[54]

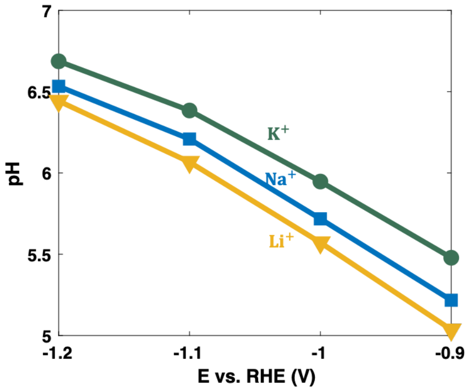

Figure 3.17: pH at the RP in 0.1 M $KHCO_3$/$NaHCO_3$/$LiHCO_3$ solutions.

It should be noted that cation effects are multifaceted in electrocatalysis, including for instance hydrolysis,[54] promoter,[53], and electric field effects.[77, 111] The analysis in this work emphasizes the steric effect. The same cation overcrowding effect has recently also been applied to explain the cation effect on the oxygen evolution reaction.[68]

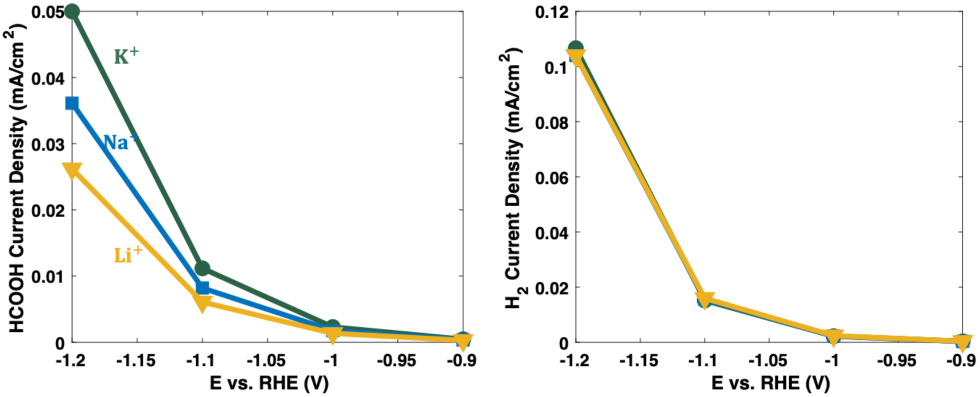

Figure 3.18: HCOOH and H_2 partial current densities in 0.1 M $KHCO_3$/$NaHCO_3$/$LiHCO_3$ solutions.

3.4.3 Effects of CO_2 pressure

CO_2 is involved not only in the electrochemical reactions (Steps 1–4), but also in the homogeneous reaction. Therefore, varying the pressure of CO_2 will affect the LRE in two ways: changing the local CO_2 concentration and pH, and modifying adsorbate coverages on the catalyst surface. Herein, the dependence of j_{CO} on CO_2 pressure is investigated (defined as b_{CO_2}) in 0.1 M $KHCO_3$ solution. For convenience, the SHE scale is used considering the shift of bulk pH with CO_2 pressure.

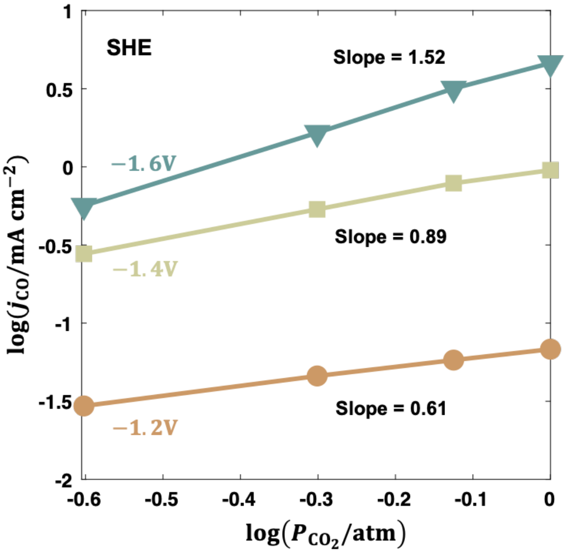

Figure 3.19: CO_2 partial pressure dependence of j_{CO} at -1.2 V, -1.4 V, -1.6 V vs. SHE.

As shown in Figure 3.19, it has been finded that b_{CO_2} increases sequentially with overpotential, being <1 at -1.2 and -1.4 V and >1 at -1.6 V. The variation of b_{CO_2} with potential is caused by the influence of LRE. At low overpotentials, $\theta_{H_{ad}}$ is negligible, while the increase of CO_2 concentration promotes the adsorption of $HCOO_{ad}$. Thus, the increase of $\theta_{HCOO_{ad}}$ inhibits the CO pathway through site blocking effects and lateral interactions, leading to $b_{CO_2} < 1$. At high overpotentials, $\theta_{H_{ad}}$ is not negligible, and the increase of $\theta_{HCOO_{ad}}$ can inhibit the adsorption of H_{ad}, which has a stronger repulsion effect on $COOH_{ad}$, leading to $b_{CO_2} > 1$.

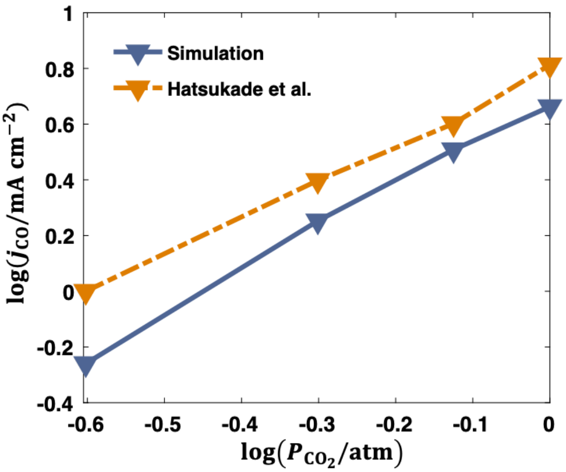

Figure 3.20: CO_2 partial pressure dependence of j_{CO} at -1.2 V vs. RHE.

The simulated b_{CO_2} shows good agreement with the experimental data at -1.2 V (RHE),[107] as shown in Figure 3.20. However, b_{CO_2} at a specific overpotential is usually used as a mechanistic probe for the CO_2RR. Values of $b_{CO_2} \approx 0.5$[96] and $b_{CO_2} \approx 1$[108, 121] have been reported in the literature, leading to different reaction mechanisms. Here, I caution not to use the observed b_{CO_2} as a probe of the reaction mechanism and not to use $b_{CO_2} = 1$ to determine the reaction rate in kinetic modeling.

3.5 Conclusions

In this chapter, I applied the hierarchical framework to elucidate the influence of the local reaction environment on CO_2 reduction at an Ag electrode. Several important insights are gleaned from the model.

Firstly, the model explains the bell-shaped CO partial current density caused by the transition between rate-determining terms. The intrinsic kinetics is dominant at low and medium overpotentials, resulting in the increase of activity. Based on the assessment of the CO_2 concentration at the reaction plane, the anomalous decrease of the CO partial current density at high overpotentials is unlikely to be attributable solely to the decrease of CO_2 concentration. However, a consistent explanation of the trend can be given if lateral interactions between $HCOO_{ad}$, $COOH_{ad}$, and H_{ad} are accounted for in the model. This, of course, does not exclude other explanations of the experimental trends so far not accounted for in the model. In addition, it has been shown that the experimentally observed Tafel slope of 59 mV/dec at low overpotentials is a combined result of the intrinsic slope of 39 mV/dec and the surface charge effects, while the Tafel slope of > 118 mV/dec at medium overpotentials is a combined result of the intrinsic slope 118 mV/dec, the surface charge effects, and the mass transport effects.

The local reaction environment was tuned by varying the bicarbonate concentration, the type of electrolyte cation, and the CO_2 pressure. I show that the bicarbonate is neither the direct reaction partner nor the main source of CO_2, but it can increase the local CO_2 concentration when the mass transport effects are significant by maintaining the local pH and inhibiting the homogeneous reaction of CO_2 to HCO_3^-. The steric effect of cations is shown to increase with the solvated size of cations, resulting in the activity in the order of $K^+ > Na^+ > Li^+$. Besides, the dependence of activity on the pressure of CO_2 was shown to change with overpotential. These results together stress the importance of the local reaction environment in understanding electrocatalytic reactions.

4 pH effects in a model electrocatalytic reaction disentangled

In this chapter, I apply the hierarchical framework to study pH effects in electrocatalytic reactions. Varying the solution pH not only changes reactant concentrations in bulk solution, but also the local reaction environment that is shaped together by macroscopic mass transport and microscopic electric double layer effects. Understanding the ubiquitous pH effects in electrocatalysis requires disentangling these interwoven factors, which is a difficult, if not impossible, task without modelling.

Herein, I demonstrate how the hierarchical model can help understand pH effects of formic acid oxidation reaction, which is an important model reaction in electrochemistry. In terms of the relation between the peak activity and the solution pH, intrinsic pH effects without considering changes in the LRE would lead to a bell shape peaked at pH = 6. Adding only macroscopic mass transport, I can already reproduce qualitatively the experimentally observed trapezoidal shape with a plateau between pH 5 and 10 in perchlorate and sulfate solutions. A quantitative agreement with experimental data requires the consideration of EDL effects to go beyond Frumkin correlations. Specifically, the peculiar nonmonotonic surface charging relation affects the free energies of adsorbed intermediates. The pH effects of FAOR in phosphate and chloride-containing solutions are further discussed, for which the anion adsorption becomes important. This work underpins the importance of the complex interplay of multiple factors for the interpretation of pH effects in electrocatalysis.

The chapter is based on the published research article:

- Zhu, X.; Huang, J.; Eikerling, M. *pH Effects in a Model Electrocatalytic Reaction Disentangled.* JACS Au 2023, 3(4), 1052–1064.

4.1 Introduction

A quintessential aspect of electrocatalysis is that the activity of a particular reaction can vary over several orders of magnitude if different electrode materials or atomic surface configurations are used.[1, 15] In the past decades, remarkable progress in understanding the role of the electrode material has paved the way towards rational designs of electrocatalysts.[1, 15, 17, 122–125] The other medium involved in electrocatalysis, viz. the electrolyte, is however much less understood. Controversy exists over how the type and concentration of cations modulate the reaction activity,[27, 53, 68] and why variations in solution pH cause activity differences of several orders of magnitude for specific reactions.[50, 62, 126–129]

Various explanations of pH effects in electrocatalytic reactions have been given, including shifts of bulk proton concentration and electrode potential on the SHE scale,[129, 130] changes in proton donor or oxidant,[50, 131, 132] and modulations on possible solution-phase reactions.[133–135] In addition to these overall properties, local properties in the EDL, including local potential, concentration and electric field, can also change with the solution pH.

Recent years have witnessed growing attention to the LRE effects. For instance, macroscopic mass transport induces departure of the local pH from the bulk pH during the FAOR.[136, 137] Additionally, the local reactant concentration, which is lower than the bulk concentration due to the macroscopic mass transport, is a key factor to understand the pH effects on the HER/HOR[50, 138] and the CO_2RR.[97, 139] It has also been demonstrated that the electric field in the EDL impacts the free energies of intermediates in the ORR[140, 141] and the CO electrochemical reduction.[53, 113] Lastly, the role of the reorganization of interfacial water affected by the electric field is highlighted in the HER.[13, 142] These studies have shown that the apparent pH effects are the consequence of multiple interacting factors. Any endeavor towards a comprehensive understanding should be aware of their interplay and find a proper way to disentangle them, which is highly nontrivial even for simple model reactions, such as

HER and FAOR.[13, 143] Theory and modeling are indispensable to this end.[1, 15, 126]

In this chapter, I aim to disentangle the aforementioned multiple factors that affect the pH effects in FAOR. Marked pH effects have been reported by several independent groups for this model system, but the explanations given have remained controversial. The controversy on reproducible experimental phenomena in the simplest model system just indicates the complexity arising from multiple interacting factors, as well as the lack of a reliable approach to handle the complexity. I carefully analyze experimental data using a set of models that gradually climb the ladder of complexity, in order to avoid overfitting of experimental data. The incremental analysis underlines the importance of considering LRE in understanding experimental pH effects. Additionally, it is revealed that a quantitative analysis of experiments requires taking into account EDL effects that go beyond the Frumkin corrections but were not considered in previous studies.

4.2 Model development

The oxidation of formic acid for a system consisting of a Pt(111) RDE in 0.5 M perchlorate solutions under ambient conditions (25 °C, 101.3 kPa) is modelled. The pH range from 0 to 12 is considered.

4.2.1 Microkinetics

The reaction mechanism used in this model involves three adsorbates, $HCOO_b$, $HCOO_m$, and OH_{ad},[67]

$$\mathrm{HCOOH} + 2^* \rightleftharpoons \mathrm{HCOO_b} + \mathrm{H^+} + \mathrm{e^-} \quad \text{(Step 1)}$$

$$\mathrm{HCOO^-} + 2^* \rightleftharpoons \mathrm{HCOO_b} + \mathrm{e^-} \quad \text{(Step 2)}$$

$$\mathrm{HCOOH} + {}^* \rightleftharpoons \mathrm{HCOO_m} + \mathrm{H^+} + \mathrm{e^-} \quad \text{(Step 3)}$$

$$\mathrm{HCOO^-} + {}^* \rightleftharpoons \mathrm{HCOO_m} + \mathrm{e^-} \quad \text{(Step 4)}$$

$$\mathrm{HCOO_m} \rightarrow \mathrm{CO_2} + \mathrm{H^+} + \mathrm{e^-} + {}^* \quad \text{(Step 5)}$$

$$\mathrm{H_2O} + {}^* \rightleftharpoons \mathrm{OH_{ad}} + \mathrm{H^+} + \mathrm{e^-} \quad \text{(Step 6)}$$

$$\mathrm{OH^-} + {}^* \rightleftharpoons \mathrm{OH_{ad}} + \mathrm{e^-} \quad \text{(Step 7)}$$

Bridge-bonded formate $HCOO_b$ was detected on Pt electrodes by surface-enhanced IR absorption spectroscopy.[144] However, $HCOO_b$ is unlikely to be the main active intermediate because density functional theory (DFT) calculations have shown that its oxidation barrier is too high ($\approx$ 1.1 eV).[145, 146] In situ IR studies have shown that $HCOO_b$ is a site-blocking spectator.[147, 148] Therefore, the oxidation step of $HCOO_b$ should be negligible. It has then been speculated that there must be other active intermediates, which, due to their short lifetime and/or low coverage, were not detected in spectroscopic measurements.[148] DFT calculations have proposed two candidates, $COOH_{ad}$[149] and C–H down monodentate formate $HCOO_m$.[150, 151] Following studies on the pH effects of FAOR,[57, 135, 152, 153] the $HCOO_m$ as the main active intermediate is considered. Herein, there is negligible adsorbed CO_{ad} because CO_{ad} is considered to be absent on defect-free Pt(111).[154] In addition, cyclic voltammetry data in the negative scan during which CO_{ad} is oxidized are used for the analysis.[57, 155, 156] In addition to the main reactions, this model also considers water oxidation at high potentials that forms site-blocking OH_{ad}.

For the case of phosphate solutions, the FAOR is inhibited when pH > 4.[57, 157] This is the pH range in which $\mathrm{HPO_4^{2-}}$ appears. Therefore, the adsorption of $\mathrm{HPO_4^{2-}}$ is considered,

$$\mathrm{HPO_4^{2-}} + * \rightleftharpoons \mathrm{HPO^-_{4,ad}} + e^- \quad \text{(Step 8)}$$

For the case of chloride-containing solutions, anion adsorption is accounted for via

$$\mathrm{Cl}^- + * \rightleftharpoons \mathrm{Cl}_{\mathrm{ad}} + e^- \quad \text{(Step 9)}$$

Based on the postulated reaction mechanism, rate equations for the changes of adsorbate coverages, which are zero at steady state, can be formulated

$$\frac{d\theta_{\mathrm{HCOO_b}}}{dt} = r_1 + r_2, \tag{4.1}$$

$$\frac{d\theta_{\mathrm{HCOO_m}}}{dt} = r_3 + r_4 - r_5, \tag{4.2}$$

$$\frac{d\theta_{\mathrm{OH_{ad}}}}{dt} = r_6 + r_7, \tag{4.3}$$

$$\frac{d\theta_{\mathrm{HPO^-_{4,ad}}}}{dt} = r_8, \tag{4.4}$$

$$\frac{d\theta_{\mathrm{Cl_{ad}}}}{dt} = r_9, \tag{4.5}$$

where $\theta_{\mathrm{HCOO_b}}$, $\theta_{\mathrm{HCOO_m}}$, $\theta_{\mathrm{OH_{ad}}}$, $\theta_{\mathrm{HPO^-_{4,ad}}}$, and $\theta_{\mathrm{Cl_{ad}}}$ are coverages, and r_i is the reaction rate of step i. For the latter, there are the following relations,

$$r_1 = k_1 c^{\mathrm{RP}}_{\mathrm{HCOOH}} \theta_0^2 - k_{-1} \theta_{\mathrm{HCOO_b}} c^{\mathrm{RP}}_{\mathrm{H^+}}, \tag{4.6}$$

$$r_2 = k_2 c^{\mathrm{RP}}_{\mathrm{HCOO^-}} \theta_0^2 - k_{-2} \theta_{\mathrm{HCOO_b}}, \tag{4.7}$$

$$r_3 = k_3 c^{\mathrm{RP}}_{\mathrm{HCOOH}} \theta_0 - k_{-3} \theta_{\mathrm{HCOO_m}} c^{\mathrm{RP}}_{\mathrm{H^+}}, \tag{4.8}$$

$$r_4 = k_4 c^{\mathrm{RP}}_{\mathrm{HCOO^-}} \theta_0 - k_{-4} \theta_{\mathrm{HCOO_m}}, \tag{4.9}$$

$$r_5 = k_5 \theta_{\mathrm{HCOO_m}}, \tag{4.10}$$

$$r_6 = k_6 \theta_0 - k_{-6} \theta_{\mathrm{OH_{ad}}} c^{\mathrm{RP}}_{\mathrm{H^+}}, \tag{4.11}$$

$$r_7 = k_7 c^{\mathrm{RP}}_{\mathrm{OH^-}} \theta_0 - k_{-7} \theta_{\mathrm{OH_{ad}}}, \tag{4.12}$$

$$r_8 = k_8 c^{\mathrm{RP}}_{\mathrm{HPO_4^{2-}}} \theta_0 - k_{-8} \theta_{\mathrm{HPO^-_{4,ad}}}, \tag{4.13}$$

$$r_9 = k_9 c^{\mathrm{RP}}_{\mathrm{Cl^-}} \theta_0 - k_{-9} \theta_{\mathrm{Cl_{ad}}}, \tag{4.14}$$

where $\theta_0 = \theta_{\text{max}} - 2\theta_{\text{HCOO}_\text{b}} - \theta_{\text{HCOO}_\text{m}} - \theta_{\text{OH}_\text{ad}} - \theta_{\text{HPO}^-_{4,\,\text{ad}}} - \theta_{\text{Cl}_\text{ad}}$ is the coverage of vacancy (free sites), with $\theta_{\text{max}} = 0.6$ being the maximum $2\theta_{\text{HCOO}_\text{b}}$.[158] c_i^{RP} are concentrations at the reaction plane that need to be determined from the local reaction environment model.

It should be noted that the same θ_{max} for all adsorbates is used, while the θ_{max} for OH_ad in ref. [159] is about 0.3. Therefore, the sensitivity of $\theta_{\text{OH}}^{\text{max}}$ in the $j - E_\text{M}$ curve at pH values of 3, 7, and 11 is examined, corresponding to acidic, neutral, and alkaline conditions, respectively. The results in Figure 4.1 show that the $j - E_\text{M}$ curve is not sensitive to $\theta_{\text{OH}}^{\text{max}}$ at acidic pH, while the decrease in $\theta_{\text{OH}}^{\text{max}}$ weakens the site-blocking effect of OH_ad at neutral/alkaline pH and high potentials. However, the trend of the $j - E_\text{M}$ curve remains the same. Therefore, the simplification of using the same θ_{max} for HCOO_b and OH_ad is reasonable for the case in this work.

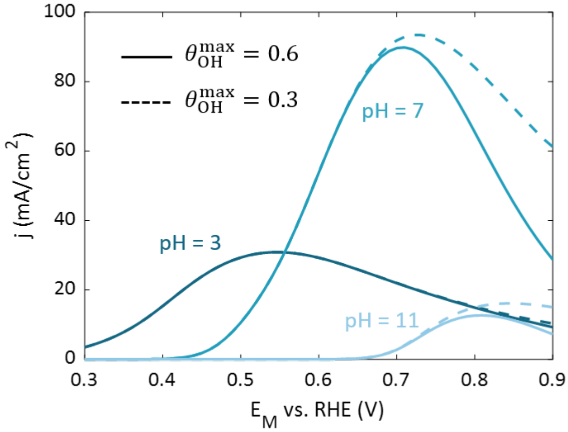

Figure 4.1: Sensitivity of $\theta_{\text{OH}}^{\text{max}}$ in the $j - E_\text{M}$ curve at pH = 3, pH = 7 and pH = 11, corresponding to acidic, neutral and alkaline conditions, respectively.

The variations in the Gibbs free energies of HCOO_b, HCOO_m, OH_ad, and $\text{HPO}^-_{4,\text{ad}}$ due to lateral interactions between adsorbates are considered,

$$\Delta G_{\mathrm{HCOO_b}} = \xi_{\mathrm{HCOO_b-HCOO_b}}\theta_{\mathrm{HCOO_b}}, \tag{4.15}$$

$$\Delta G_{\mathrm{HCOO_m}} = \xi_{\mathrm{HCOO_b-HCOO_m}}\theta_{\mathrm{HCOO_b}} + \xi_{\mathrm{OH_{ad}-HCOO_m}}\theta_{\mathrm{OH_{ad}}} + \xi_{\mathrm{HPO^-_{4,ad}-HCOO_m}}\theta_{\mathrm{HPO^-_{4,ad}}}, \tag{4.16}$$

$$\Delta G_{\mathrm{OH_{ad}}} = \xi_{\mathrm{OH_{ad}-OH_{ad}}}\theta_{\mathrm{OH_{ad}}}, \tag{4.17}$$

$$\Delta G_{\mathrm{HPO^-_{4,ad}}} = \xi_{\mathrm{HPO^-_{4,ad}-HPO^-_{4,ad}}}\theta_{\mathrm{HPO^-_{4,ad}}}, \tag{4.18}$$

with ξ_{X-Y} the lateral interaction parameters. The variations in the reaction Gibbs free energies of steps are given by,

$$\Delta\Delta G_1 = \Delta\Delta G_2 = \Delta G_{\mathrm{HCOO_b}}, \tag{4.19}$$

$$\Delta\Delta G_3 = \Delta\Delta G_4 = -\Delta\Delta G_5 = \Delta G_{\mathrm{HCOO_m}}, \tag{4.20}$$

$$\Delta\Delta G_6 = \Delta\Delta G_7 = \Delta G_{\mathrm{OH_{ad}}}, \tag{4.21}$$

$$\Delta\Delta G_8 = \Delta G_{\mathrm{HPO^-_{4,ad}}}. \tag{4.22}$$

$\theta_{\mathrm{HCOO_b}}$, $\theta_{\mathrm{HCOO_m}}$, $\theta_{\mathrm{OH_{ad}}}$, $\theta_{\mathrm{HPO^-_{4,\,ad}}}$, and $\theta_{\mathrm{Cl_{ad}}}$ are obtained by solving the rate equations. The partial current densities are given by,

$$j_{\mathrm{HCOOH}} = -2e\rho r_3, \tag{4.23}$$

$$j_{\mathrm{HCOO^-}} = -2e\rho r_4, \tag{4.24}$$

$$j_{\mathrm{H}} = -(j_{\mathrm{HCOOH}} + j_{\mathrm{HCOO^-}}/2), \tag{4.25}$$

$$j_{\mathrm{total}} = 2e\rho r_5, \tag{4.26}$$

$$\tag{4.27}$$

with ρ the number density of active sites at Pt(111) and $e\rho = 2.41$ C m^{-2} in this model.[74]

4.2.2 Local reaction environment

The model system is shown in Figure 4.2. I consider an adlayer between the electrode and the electrolyte, in which the intermediates are adsorbed and the potential distribution across the adlayer is assumed to be linear. The reaction plane (RP) is located at the outer surface of the adlayer (x=0), which is also the position of closest ion. Outside the RP resides the diffusion layer, whose thickness is determined as,[160]

$$\delta_\mathrm{D} = 1.62 D_{\mathrm{HCOO^-}}^{1/3} v^{1/6} \omega^{-1/2}, \tag{4.28}$$

where $D_{\mathrm{HCOO^-}}$ is the diffusion coefficient of $\mathrm{HCOO^-}$, v is the kinematic viscosity of the solution phase, and ω is the rotation speed of the RDE. $D_{\mathrm{HCOO^-}}$ is used to calculate the diffusion layer thickness since $\mathrm{HCOO^-}$ is the main reactant.

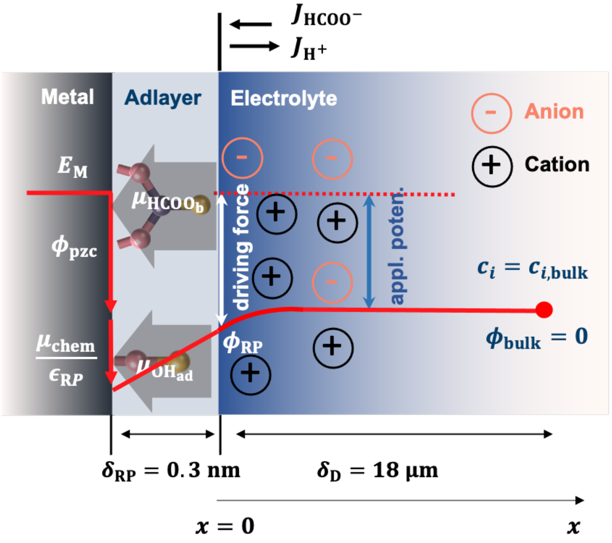

Figure 4.2: Schematic illustration of the model system. Two zones at the electrode-electrolyte surface are distinguished: the adlayer and the boundary layer in the electrolyte. The reaction plane is located at the boundary between them, where the fluxes are indicated. The solid red line is a schematic potential profile for the case of negative surface charge, with E_M denoting the applied metal potential and ϕ_{pzc} the potential of zero charge. μ_{chem} is the dipole moment associated with chemisorbed $\mathrm{HCOO_b}$ and $\mathrm{OH_{ad}}$. The driving force for interface reactions is defined as the difference between the applied potential E_M and the potential at the reaction plane ϕ_{RP}. δ_{RP} and $\delta_\mathrm{D}$are the thicknesses of the adlayer and diffusion layer, respectively.

The multicomponent mass transport including HCOOH, $HCOO^-$, OH^-, ClO_4^-, H^+, Na^+, H_3PO_4, $H_2PO_4^-$, HPO_4^{2-}, and PO_4^{3-} are described by the modified PNP theory, namely, eq. (3.22). The simplified version takes into account steric effects but neglects water polarization.

Two homogeneous reactions, formic acid dissociation and water dissociation, are considered to occur in the perchlorate electrolyte,

$$\mathrm{HCOOH} \rightleftharpoons \mathrm{H}^+ + \mathrm{HCOO}^- \quad (\mathrm{pK_a} = 3.75) \quad \text{(Step R1)}$$

$$\mathrm{H_2O} \rightleftharpoons \mathrm{OH}^- + \mathrm{H}^+ \quad (\mathrm{pK_a} = 14) \quad \text{(Step R2)}$$

When the FAOR in phosphate solution is explored, in addition to Steps R1 and R2, the following buffer reactions are considered,

$$\mathrm{H_3PO_4} \rightleftharpoons \mathrm{H_2PO_4^-} + \mathrm{H}^+ \quad (\mathrm{pK_a} = 2.16) \quad \text{(Step R3)}$$

$$\mathrm{H_2PO_4^-} \rightleftharpoons \mathrm{HPO_4^{2-}} + \mathrm{H}^+ \quad (\mathrm{pK_a} = 7.21) \quad \text{(Step R4)}$$

$$\mathrm{HPO_4^{2-}} \rightleftharpoons \mathrm{PO_4^{3-}} + \mathrm{H}^+ \quad (\mathrm{pK_a} = 12.32) \quad \text{(Step R5)}$$

4.2.3 Model parameterization

All the parameters included in the microkinetic model are listed in Tables 4.1 and 4.2.

According to the thermodynamic equilibrium, one finds

$$E_1^{\mathrm{eq}} = E_2^{\mathrm{eq}} + \frac{\Delta G^0_{\mathrm{HCOO^-}} + \Delta G^0_{\mathrm{H^+}} - \Delta G^0_{\mathrm{HCOOH}}}{e}. \tag{4.29}$$

According to the dissociation equilibrium of formic acid, Step R1,

$$\Delta G^0_{\mathrm{HCOOH}} = \Delta G^0_{\mathrm{HCOO^-}} + \Delta G^0_{\mathrm{H^+}} + k_B T \ln 10^{-\mathrm{pK_a}}. \tag{4.30}$$

Combining eqs. (4.29) and (4.30), the relations between the standard equilibrium potentials of

Steps 1 and 2 can be determined,

$$E_1^{\mathrm{eq}} = E_2^{\mathrm{eq}} + 0.22\ \mathrm{V}. \tag{4.31}$$

Following the same logic,

$$E_3^{\mathrm{eq}} = E_4^{\mathrm{eq}} + 0.22\ \mathrm{V}, \tag{4.32}$$

$$E_5^{\mathrm{eq}} = -E_3^{\mathrm{eq}} - 0.07\ \mathrm{V}, \tag{4.33}$$

$$E_6^{\mathrm{eq}} = E_7^{\mathrm{eq}} + 0.83\ \mathrm{V}. \tag{4.34}$$

The $\mathrm{HCOO_b}$ adsorption is very fast and in equilibrium, as shown in the voltammograms.[161] Therefore, the activation barriers of $\mathrm{HCOO_b}$ adsorption steps should be very low.$G_{\mathrm{a},1}^{\mathrm{eq}} = G_{\mathrm{a},2}^{\mathrm{eq}} = 0.3$ eV are used, close to the DFT calculations.[146] $E_1^{\mathrm{eq}} = 0.4$ V is taken from DFT results,[145, 146] which is consistent with the peak position of $\mathrm{HCOO_b}$ adsorption.[161] $E_2^{\mathrm{eq}} = 0.18$ V is calculated based on Eq. (4.31). $\beta_1 = \beta_2 = 0.5$ is taken from the DFT study.[146]

Using transient calorimetry, $\Delta G^0_{\mathrm{HCOO_m}} - \Delta G^0_{\mathrm{HCOO_b}} = 0.3$ eV is obtained.[162] Therefore,

$$E_3^{\mathrm{eq}} = E_1^{\mathrm{eq}} + 0.3 = 0.7\ \mathrm{V}, \tag{4.35}$$

$$E_4^{\mathrm{eq}} = E_3^{\mathrm{eq}} - 0.22 = 0.48\ \mathrm{V}, \tag{4.36}$$

$$E_5^{\mathrm{eq}} = -E_1^{\mathrm{eq}} - 0.07 = -0.77\ \mathrm{V}. \tag{4.37}$$

The oxidation of $\mathrm{HCOO_m}$ is much faster than its adsorption due to its negligible coverage, implying that the adsorption Steps 3 and 4 are rate-determining steps. Therefore, $\beta_3 = \beta_4$ is set to be 0.4, corresponding to the value estimated from the Tafel slope (150 mV/dec).[163] $G_{\mathrm{a},3}^{\mathrm{eq}}$ and $G_{\mathrm{a},4}^{\mathrm{eq}}$ are fitted in the experimentally determined range of apparent activation barriers (0.4 – 0.6 eV).[164] $G_{\mathrm{a},5}^{\mathrm{eq}}$ and β_5 are not sensitive parameters. β_5 is set to the usual value of 0.5, and $G_{\mathrm{a},5}^{\mathrm{eq}}$ is given as 0.6 eV (the activation barrier is low in the potential range of interest since E_5^{eq} is very negative).

For $\mathrm{OH_{ad}}$ adsorption, the DFT-calculated parameters are adopted.[74, 165] For $\mathrm{HPO_4^{2-}}$ and

Cl^- adsorption, $G_{\mathrm{a},8}^{\mathrm{eq}} = G_{\mathrm{a},9}^{\mathrm{eq}} = 0.3$ eV are used, implying the strong adsorption of these two anions. E_8^{eq} and E_9^{eq} correspond to the potentials at which specific adsorption occurs.[166, 167] $\beta_8 = \beta_9 = 0.5$ are usual values.

Table 4.1: Reaction parameters used in the model, including the activation energies, $G_{a,i}^{\mathrm{eq}}$, the standard equilibrium potentials, E_i^{eq}, and the transfer coefficients, β_i, of step i

Step i	E_i^{eq} (V SHE)	$G_{a,i}^{\mathrm{eq}}$ (eV)	β_i
1	0.3	0.4	0.5
2	0.3	0.18	0.5
3	0.56	0.7	0.4
4	0.44	0.48	0.4
5	0.6	-0.77	0.5
6	0.26	0.78	0.5
7	0.26	-0.05	0.5
8	0.3	0.06	0.5
9	0.3	-0.04	0.5

For the lateral interaction parameters, $\xi_{\mathrm{HCOO_b-HCOO_b}}$ was calculated to be 0.2 eV,[158] $\xi_{\mathrm{OH_{ad}-OH_{ad}}}$ is set to be 0.15 eV,[7] $\xi_{\mathrm{HCOO_b-HCOO_m}}$ and $\xi_{\mathrm{OH_{ad}-HCOO_m}}$ are fitted parameters.

Table 4.2: Lateral interaction parameters (eV)

$\xi_{\mathrm{HCOO_b-HCOO_m}}$	0.2	$\xi_{\mathrm{HPO^-_{4,ad}-HCOO_m}}$	0.15
$\xi_{\mathrm{HCOO_b-HCOO_b}}$	0.2	$\xi_{\mathrm{HPO^-_{4,ad}-HPO^-_{4,ad}}}$	0.3
$\xi_{\mathrm{OH_{ad}-HCOO_m}}$	0.15	$\xi_{\mathrm{Cl_{ad}-HCOO_m}}$	0.15
$\xi_{\mathrm{OH_{ad}-OH_{ad}}}$	0.15	$\xi_{\mathrm{Cl_{ad}-Cl_{ad}}}$	0.25

The forward rate constants of the homogeneous reactions are listed in Table 4.3.[11, 168, 169]

The reverse rate constants can be calculated as,

$$k_{-Ri} = k_{Ri} 10^{\mathrm{pK_a}}. \tag{4.38}$$

Table 4.3: Forward rate constants of homogeneous reactions

Reaction	R1	R2	R3	R4	R5
k_{Ri}	4×10^5	2.4×10^{-5}	1×10^6	1×10^6	1×10^6

The parameters used to describe the mass transport, including diffusion coefficients D_α, effective solvated diameter d_α, kinematic viscosity of solution v, and the rotation speed of the RDE ω are listed in Table 4.4. [57, 117, 136, 137, 170, 171]

Table 4.4: Parameters for the mass transport

Category	Item	Value
D_α (m^2/s)	HCOOH	1.41×10^{-9}
	$HCOO^-$	1.454×10^{-9}
	OH^-	5.27×10^{-9}
	H^+	9.311×10^{-9}
	Na^+	1.334×10^{-9}
	ClO_4^-	1.029×10^{-9}
	H_3PO_4	9.59×10^{-10}
	$H_2PO_4^-$	8.5×10^{-10}
	HPO_4^{2-}	6.9×10^{-10}
	PO_4^{3-}	6.1×10^{-10}
d_α (m)	Na^+	0.716×10^{-9}
v (m^2/s)	Kinematic viscosity of water	1.1×10^{-6}
ω (rpm)	Rotation speed of the RDE	1000

The parameters of the EDL are listed in Table 4.5. The net charge numbers of adsorbates are fitted parameters with experiments. The permittivity of the adlayer is taken as $2.3\epsilon_0$, which is usually in the range of $2-10\epsilon_0$.[50] The thickness of the adlayer is assumed to be 0.3 nm, which is the Pt-C distance of $HCOO_b$.[149] ϕ_{pzc} is measured to be 0.3 V versus SHE.[172] Other parameters are constants.

Table 4.5: Parameters for the electric double layer

Category	Item	Value
Net charge number per adsorbate	ς_{HCOO_b}	0.03
	$\varsigma_{OH_{ad}}$	0.04
	$\varsigma_{HPO^-_{4,ad}}$	0.06
	$\varsigma_{Cl_{ad}}$	0.02
Permittivity of the vacuum	ϵ_0	8.85×10^{-12}
Permittivity of the solution	ϵ_s	$78.5\epsilon_0$
Permittivity of the adlayer	ϵ_{RP}	$2.3\epsilon_0$
Thickness of the adlayer	δ_{RP}	0.3 nm
Potential of zero charge	ϕ_{pzc}	0.3 V (SHE)

4.3 Results

In this work, I mainly focus on the relation between the peak current density and the pH value, namely, the j_p- pH relation, which is the most discussed relation in studies of the pH effects in FAOR.[57, 135] The analysis begins with exclusive consideration of the microkinetics. The mass transport effects and surface charging effects are then added in sequential steps. This approach allows disentangling different factors controlling the overall pH effects.

4.3.1 Intrinsic microkinetics

The intrinsic microkinetics is defined as reaction kinetics without accounting for effects of the local reaction environment, which means that $c_\alpha = c_{\alpha,\mathrm{bulk}}$, $\phi_{\mathrm{RP}} = 0$, and $\sigma_{\mathrm{free}} = 0$ are considered. I start with simulating the polarization curves, namely, the $j - E_\mathrm{M}$ curves, at different pHs using the parameters in Tables 4.1 and 4.2. Figure 4.3 compares the simulations and experiments, with experimental data taken from ref. [164]. The model captures main features of experimental data, namely, the $j - E_\mathrm{M}$ curve presents as a bell shape and the activity increases with pH.

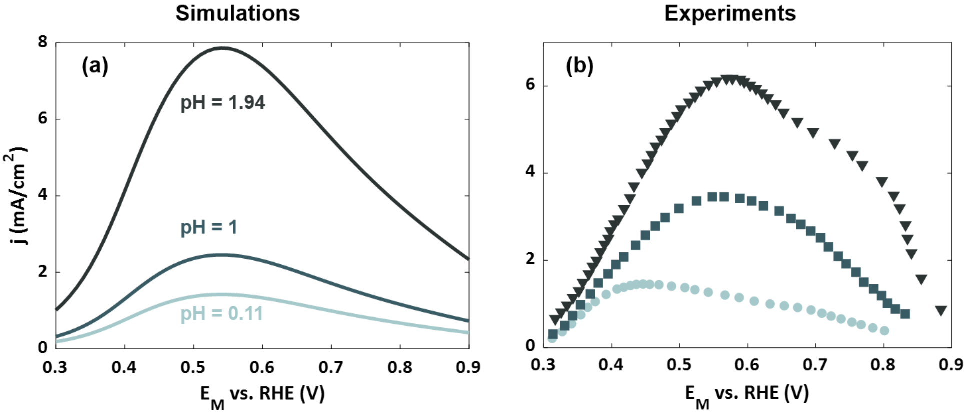

Figure 4.3: Comparison of simulated and experimental $j - E_\mathrm{M}$ curves at pH = 0.11 (1 M $HClO_4$), pH = 1 (0.1 M $HClO_4$), and pH = 1.94 (0.01 M $HClO_4$ + 0.09 M $NaClO_4$). The concentration of formic acid is 0.1 M.

However, there are quantitative differences between simulations and experiments. There could be two reasons. On the one hand, the LRE is not considered here, on the other hand, there are also noticeable discrepancies between experiments,[164, 173, 174] as shown in Figure 4.4.

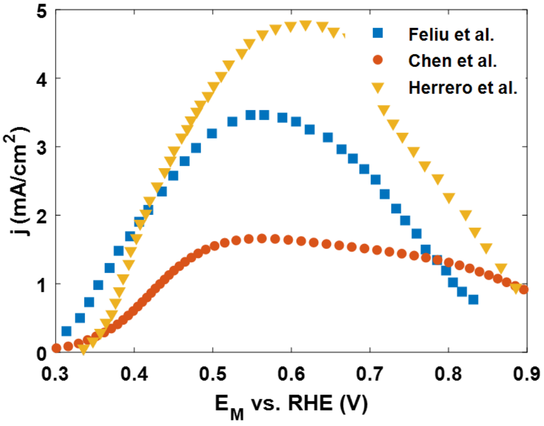

Figure 4.4: Comparison of experimental $j - E_\mathrm{M}$ curves at Pt(111) from different literature.

Recently, Herrero *et al.* reported that the reaction order for formate is 1.[153] To further validate the purported microkinetic model, I calculate the reaction order with respect to formate concentration in solutions with pH 1.2, 2.4 and 3.9 at 0.13 V versus SHE and for concentrations of formic acid between 0.01 and 2 M. The results in Figure 4.5 confirm that the reaction order is nearly 1.

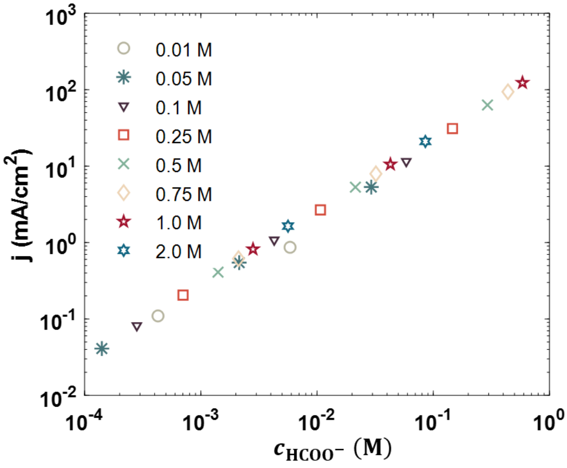

Figure 4.5: Simulated current densities at 0.13 V vs SHE as a function of the formate concentration in solutions with pH 1.2, 2.4 and 3.9. The total concentration of formic acid considered is between 0.01 and 2 M. The different symbols refer to the total formic acid concentrations.

The model is then extended to a wide pH range. Figure 4.6(a) shows the simulated $j - E_\mathrm{M}$

curves at pH from 0 to 12. The $j_\mathrm{p} - \mathrm{pH}$ relation, obtained from Figure 4.6(a), is shown in Figure 4.6(b). The $j_\mathrm{p} - \mathrm{pH}$ relation is shown to present as a bell shape, with the peak located at pH = 6, not the pK$_a$ of formic acid as previously thought.[135, 136] In addition, the peak current density remains almost constant between pH 5 and 7, with a difference below 5%.

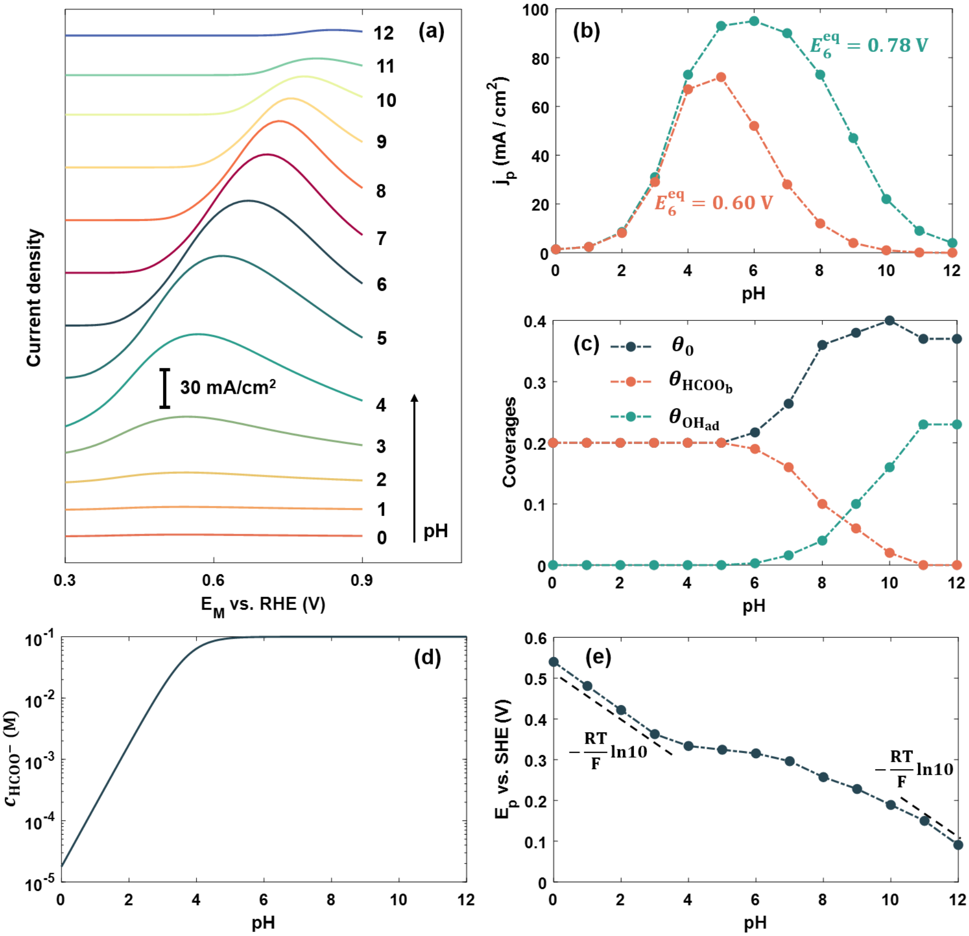

Figure 4.6: (a) Simulated $j - E_\mathrm{M}$ curves in pH range from 0 to 12. (b) Simulated $j_\mathrm{p} - \mathrm{pH}$ relations for $E_6^\mathrm{eq} = 0.78$ V (used in this work) and $E_6^\mathrm{eq} = 0.6$ V. (c) Coverages of free sites, HCOO$_b$ and OH$_{ad}$ at peak potentials. (d) Bulk concentration of HCOO$^-$ at different pHs. (e) Peak potentials on the SHE scale, $E_\mathrm{p,\,SHE}$.

It is noticed that in the work of Joo *et al.*[135] and Zhang *et al.*,[136] $E_6^\mathrm{eq} = 0.6$ V (SHE) is used to obtain the bell-shaped $j_\mathrm{p} - \mathrm{pH}$ relation with the peak near the pK$_a$ of formic acid. However, 0.6 V is much lower than the common equilibrium potential of OH$_{ad}$ adsorption at Pt(111), which is about 0.8 V,[74, 165] resulting in an overestimation of the site-blocking effect of $\mathrm{OH_{ad}}$. The comparison of $\theta_{\mathrm{OH_{ad}}}$ for $E_6^{\mathrm{eq}} = 0.78$ V and $E_6^{\mathrm{eq}} = 0.6$ V is provided in Figure 4.7.

To understand the physical origins behind the bell-shaped $j_\mathrm{p}-\mathrm{pH}$ relation, an analytical solution of the peak potential E_p is given, which is defined as the potential where the peak current density lies at a specific pH. However, since there are three adsorbates, $\mathrm{HCOO_b}$, $\mathrm{HCOO_m}$ and $\mathrm{OH_{ad}}$, and $\mathrm{HCOO_b}$ occupies two sites, the system is highly nonlinear and it cannot be solved analytically. Instead of solving E_p directly, I solve $\theta_{\mathrm{HCOO_b}}$ and $\theta_{\mathrm{OH_{ad}}}$ at E_p, which is very helpful for the analysis of the $j_\mathrm{p} - \mathrm{pH}$ relation. The lateral interactions between adsorbates are neglected for the moment to obtain the analytical solution. The validity of this assumption will be discussed later.

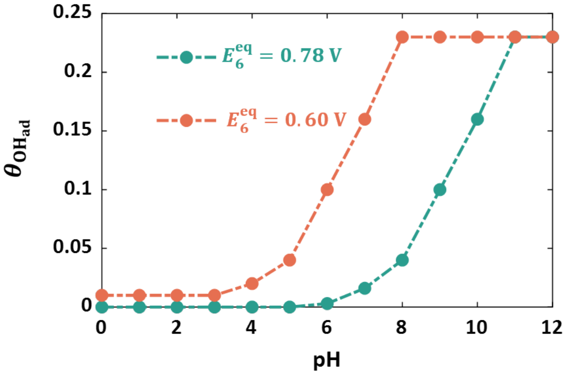

Figure 4.7: $\theta_{\mathrm{OH_{ad}}}$ at peak potentials for $E_6^{\mathrm{eq}} = 0.78$ V and $E_6^{\mathrm{eq}} = 0.6$ V.

Considering that $\mathrm{HCOO^-}$ is the main reactant and the adsorption of $\mathrm{HCOO_m}$ is the rate-determining step, the turnover frequency (TOF) can be written as

$$\mathrm{TOF} = r_4 = k_4 c_{\mathrm{HCOO^-}} (\theta_{\max} - 2\theta_{\mathrm{HCOO_b}} - \theta_{\mathrm{OH_{ad}}}). \tag{4.39}$$

The adsorption isotherms of $\mathrm{HCOO_b}$ and $\mathrm{OH_{ad}}$ are

$$\frac{(\theta_{\max} - 2\theta_{\mathrm{HCOO_b}} - \theta_{\mathrm{OH_{ad}}})^2}{\theta_{\mathrm{HCOO_b}}} = \frac{1}{K_2[\mathrm{HCOO^-}]}, \tag{4.40}$$

$$\frac{\theta_{\max} - 2\theta_{\mathrm{HCOO_b}} - \theta_{\mathrm{OH_{ad}}}}{\theta_{\mathrm{OH_{ad}}}} = \frac{1}{K_7[\mathrm{OH^-}]}, \tag{4.41}$$

with $K_i = k_i/k_{-i} = \exp\left(\frac{e}{k_BT}(E_\mathrm{M} - E_i^\mathrm{eq})\right)$ being the equilibrium constant of Step i.

At the peak potential, $\frac{\partial \mathrm{TOF}}{\partial E_\mathrm{M}} = 0$. Differentiating eq.(4.39) with respect to E_M yields

$$2\frac{\partial \theta_{\mathrm{HCOO_b}}}{\partial E_\mathrm{M}} + \frac{\partial \theta_{\mathrm{OH_{ad}}}}{\partial E_\mathrm{M}} = \frac{\beta_4 F}{RT}(\theta_\mathrm{max} - 2\theta_{\mathrm{HCOO_b}} - \theta_{\mathrm{OH_{ad}}}). \tag{4.42}$$

Differentiating eqs. (4.40) and (4.41) with respect to E_M, one finds

$$4\frac{\partial \theta_{\mathrm{HCOO_b}}}{\partial E_\mathrm{M}} + 2\frac{\partial \theta_{\mathrm{OH_{ad}}}}{\partial E_\mathrm{M}} + \frac{\theta_\mathrm{max} - 2\theta_{\mathrm{HCOO_b}} - \theta_{\mathrm{OH_{ad}}}}{\theta_{\mathrm{HCOO_b}}}\frac{\partial \theta_{\mathrm{HCOO_b}}}{\partial E_\mathrm{M}} = \frac{F}{RT}(\theta_\mathrm{max} - 2\theta_{\mathrm{HCOO_b}} - \theta_{\mathrm{OH_{ad}}}), \tag{4.43}$$

$$2\frac{\partial \theta_{\mathrm{HCOO_b}}}{\partial E_\mathrm{M}} + \frac{\partial \theta_{\mathrm{OH_{ad}}}}{\partial E_\mathrm{M}} + \frac{\theta_\mathrm{max} - 2\theta_{\mathrm{HCOO_b}} - \theta_{\mathrm{OH_{ad}}}}{\theta_{\mathrm{OH_{ad}}}}\frac{\partial \theta_{\mathrm{OH_{ad}}}}{\partial E_\mathrm{M}} = \frac{F}{RT}(\theta_\mathrm{max} - 2\theta_{\mathrm{HCOO_b}} - \theta_{\mathrm{OH_{ad}}}). \tag{4.44}$$

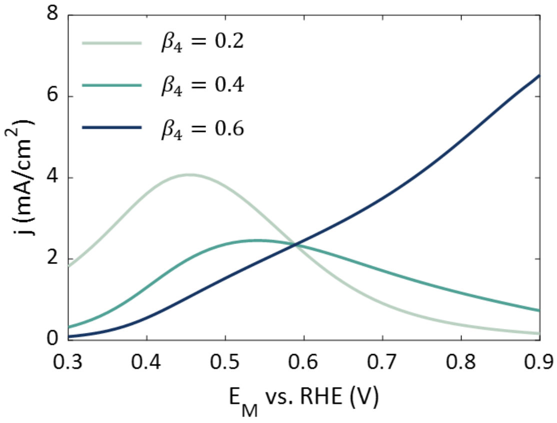

Figure 4.8: Sensitivity of β_4 in the $j - E_\mathrm{M}$ curve at pH = 1. To assess the sensitivity, the value of β_4 is varied while keeping all other parameters constant, and then simulating the $j - E_\mathrm{M}$ curves. The $j - E_\mathrm{M}$ curve is bell-shaped only when $\beta_4 < 0.5$, as predicted in Eq. (4.46). In addition, the peak potential of the bell-shaped $j - E_\mathrm{M}$ curve shifts toward a more negative potential as β_4 decreases.

Solving eqs. (4.42), (4.43), and (4.44) together, I get

$$2\frac{1-\beta_4}{\beta_4}\theta_{\mathrm{HCOO_b}} + \frac{1}{\beta_4}\theta_{\mathrm{OH_{ad}}} = \theta_\mathrm{max}, \tag{4.45}$$

where $\theta_\mathrm{max} = 0.6$ and $\beta_4 = 0.4$. In the case where $\mathrm{OH_{ad}}$ adsorption can be neglected, for example at acidic pH,[161] one can obtain

$$\theta_{\mathrm{HCOO_b}} = \frac{1}{2}\frac{\beta_4}{1-\beta_4}\theta_{\mathrm{max}} = 0.2. \tag{4.46}$$

The peak potential only exists when $\beta_4 < 0.5$ since $\theta_{\mathrm{HCOO_b}} < \frac{1}{2}\theta_{\mathrm{max}}$ ($HCOO_b$ occupies two sites). The sensitivity of β_4 in the $j - E_{\mathrm{M}}$ curve at pH = 1 is shown in Figure 4.8.

In the case where $HCOO_b$ adsorption can be neglected,

$$\theta_{\mathrm{OH_{ad}}} = \beta_4\theta_{\mathrm{max}} = 0.24. \tag{4.47}$$

The peak potential always exists in this case. Numerical calculations considering the lateral interactions do not alter the above conclusion, as shown in Figure 4.9.

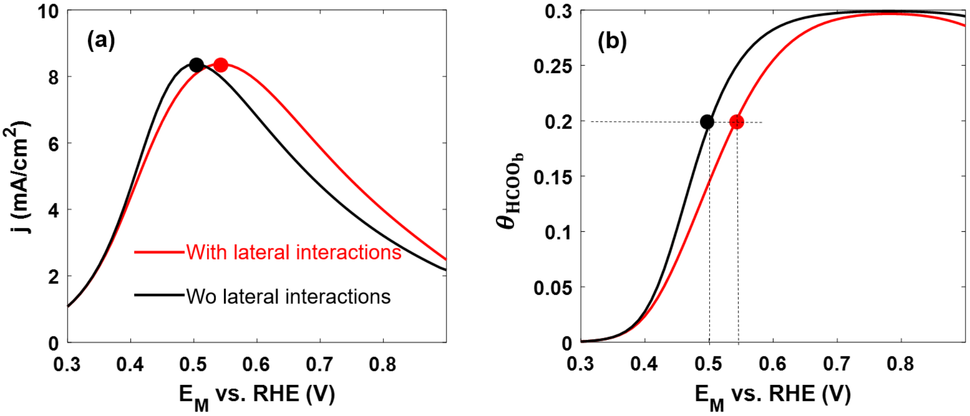

Figure 4.9: (a) Simulated $j - E_{\mathrm{M}}$ curves with and without considering lateral interactions at pH = 2. The peak potentials are indicated by dots. (b) Simulated coverages of $HCOO_b$ with and without considering lateral interactions. In both cases, $\theta_{\mathrm{HCOO_b}} = \frac{1}{2}\frac{\beta_4}{1-\beta_4}\theta_{\mathrm{max}} = 0.2$ is valid at the peak potentials.

The simulated peak potentials lie at $\theta_{\mathrm{HCOO_b}} = 0.2$ when pH < 5, in which case OH_{ad} adsorption is negligible, as shown in Figure 4.6(c). This is consistent with the analytical expression of Eq. (4.46). Specifically, $c_{\mathrm{HCOO^-}}$ shown in Figure 4.6(d) increases approximately 10 times if pH increases by 1 when pH < 3 due to the dissociation equilibrium of formic acid. Therefore, the peak potential $E_{\mathrm{p,SHE}}$ must decrease by $\frac{k_BT}{e}\ln 10$ to maintain $\theta_{\mathrm{HCOO_b}} = 0.2$ according to eq. (4.40), as shown in Figure 4.6(e). The peak current density will accordingly increase by $\exp\left(-\frac{\beta_4 e}{k_B T}\frac{k_B T}{e}\ln 10\right) \times 10 = 10^{0.6} \approx 4$ times since θ_0 is constant. When $5 < \mathrm{pH} < 10$, $c_{\mathrm{HCOO^-}}$ is constant, $E_{\mathrm{p,SHE}}$ decreases, and θ_0 increases, resulting in a nonmonotonic $j_{\mathrm{p}} - \mathrm{pH}$ relation. The adsorption of $\mathrm{OH_{ad}}$ is dominant and the adsorption of $\mathrm{HCOO_b}$ is negligible when 11 < pH < 12. Therefore, $E_{\mathrm{p,SHE}}$ decreases by $\frac{k_B T}{e}\ln 10$ to keep $\theta_{\mathrm{OH_{ad}}} = 0.24$ according to eq. (4.41), leading to a decrease of activity.

4.3.2 Mass transport

In this section, the mass transport of species is added into the play, while the effects of surface charge are not yet considered, *i.e.*, $\phi_{\mathrm{RP}} = 0$ and $\sigma_{\mathrm{free}} = 0$. Since the FAOR generates protons, the solution phase in close proximity to the electrode surface should be more acidic than the solution phase in the bulk.

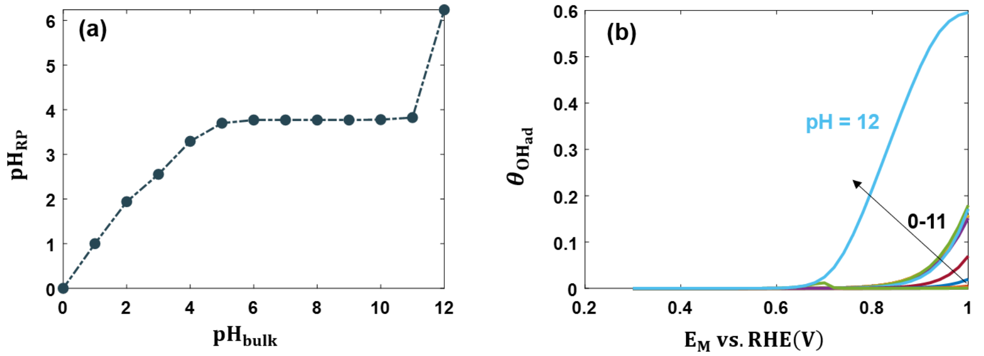

Figure 4.10: (a) Comparison of the surface pH and the bulk pH at peak potentials. (b) Adsorption isotherm of $\mathrm{OH_{ad}}$ in the pH range of 0 and 12.

Figure 4.10(a) shows the simulated behaviour of the pH at the reaction plane, $\mathrm{pH_{RP}}$, at the peak potential as a function of the bulk pH. $\mathrm{pH_{RP}}$ deviates strongly from the bulk pH for $\mathrm{pH_{bulk}} > 4$. In the range of $5 < \mathrm{pH_{bulk}} < 11$, $\mathrm{pH_{RP}}$ remains constant at $\mathrm{pH_{RP}} \approx 4$, which is consistent with previous simulations.[136] Due to the inhibited growth of $\mathrm{pH_{RP}}$ with $\mathrm{pH_{bulk}}$, $\mathrm{OH_{ad}}$ adsorption is suppressed, as shown in Figure 4.10(b). For comparison, the isotherm of $\mathrm{OH_{ad}}$ adsorption without accounting for mass transport effects is provided in Figure 4.11.

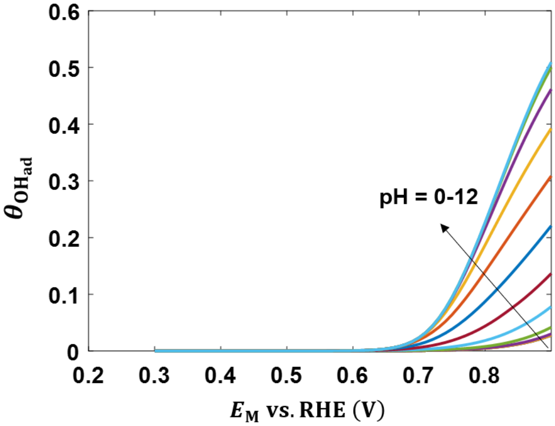

Figure 4.11: Adsorption isotherm of OH_{ad} in the pH range of 0 and 12 without considering the effects of mass transport.

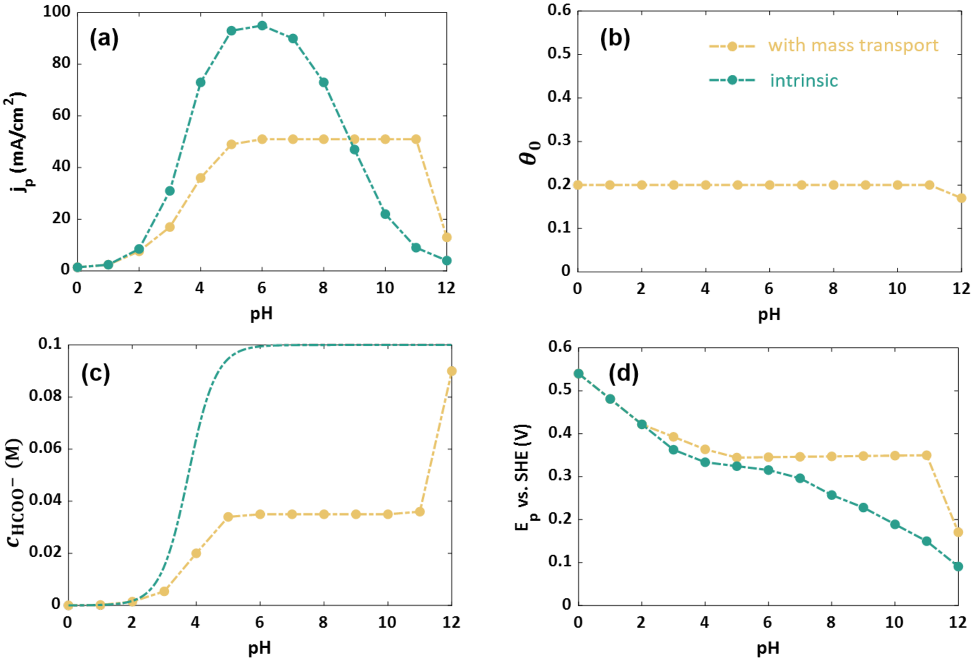

Figure 4.12: (a) Comparison of the j_p – pH relation considering only intrinsic microkinetics and the j_p – pH relation corrected by mass transport effects. (b) Coverage of free sites at peak potentials. (c) Comparison of the bulk and the surface concentrations of $HCOO^-$. (d) Comparison of the intrinsic microkinetics controlled peak potentials and the mass transport corrected peak potentials.

Under the influence of mass transport effects, the j_p – pH relation transforms from a bell shape to a trapezoidal shape, with a plateau between pH 5 and 11, as shown in Figure 4.12(a). In this pH range, OH_{ad} adsorption is negligible, Figure 4.10(b). Therefore, the peak potential remains at $\theta_{HCOO_b} = 0.2$, as shown in Figure 4.12(b). θ_0 is shown here since $\theta_0 = \theta_{max} - 2\theta_{HCOO_b} = 0.2 = \theta_{HCOO_b}$. The isotherm of $HCOO_b$ adsorption given in Figure 4.13 is consistent with the trend in experimental data in refs. [137, 158]. Since c_{HCOO^-} at the RP is constant in this pH range, as seen in Figure 4.12(c), $E_{p,SHE}$ must be fixed to maintain $\theta_{HCOO_b} = 0.2$, Figure 4.12(d). The activity therefore remains constant according to eq. (4.39).

In addition, mass transport exerts two competing effects: decreasing the reactant concentration c_{HCOO^-} at the RP, Figure 4.12(c), and increasing the driving force, Figure 4.12(d), by suppressing OH_{ad} adsorption. When pH < 9, the effect of decreasing c_{HCOO^-} dominates, leading to a decrease in activity. When pH > 9, the effect of increasing the driving force dominates, which promotes the activity.

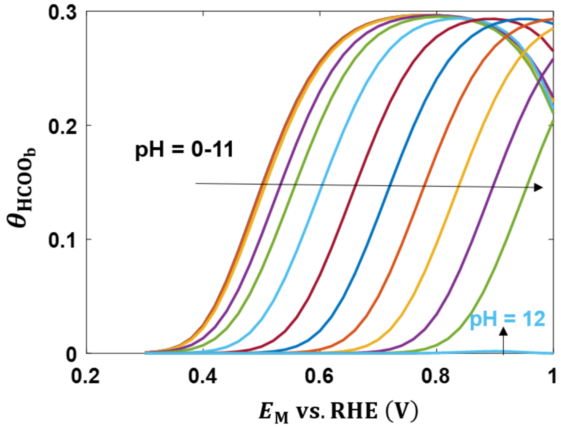

Figure 4.13: Adsorption isotherm of $HCOO_b$ in the pH range of 0 and 12 in the case of considering mass transport effects.

It has been proposed that the j_p − pH relation in phosphate solution is intrinsic because of the buffering capacity of the electrolyte.[136] I calculate the surface pH and the mass transport corrected j_p − pH relation in 0.2 M phosphate solution without considering the specific adsorption of phosphate anions. The results are shown in Figure 4.14.

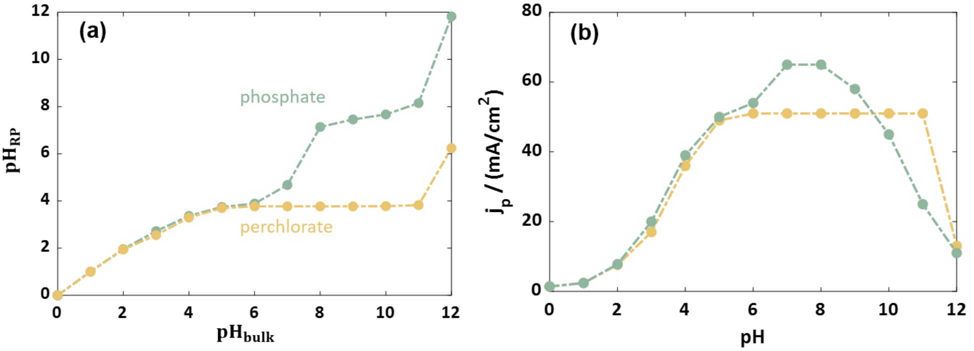

Figure 4.14: (a) Comparison of the surface pH at peak potentials and (b) comparison of the j_p − pH relations in phosphate solutions and perchlorate solutions. The specific adsorption of phosphate anions is not considered in this case.

Compared with the case in perchlorate solution, the mass transport effects are weakened due to the buffer reactions (Steps R3-R5). Correspondingly, the activity in phosphate solution is higher than that in perchlorate solution when pH < 9, contrary to the experimental observation that the activity in phosphate solution is much lower than that in perchlorate solution.[57, 135, 155, 175] This discrepancy implies that the strong anion adsorption in phosphate solution plays a more important role than its buffering capacity.

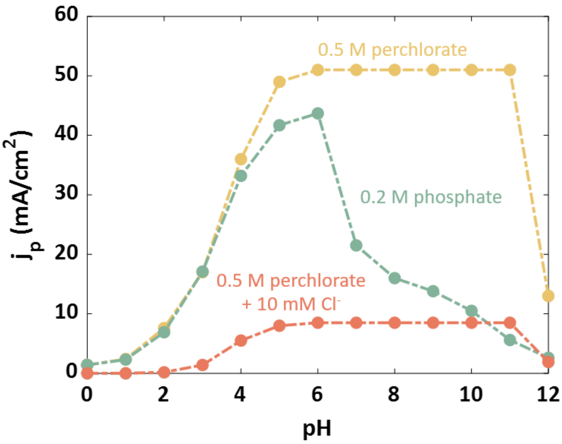

Figure 4.15: Mass transport-corrected j_p − pH relations in 0.5 M perchlorate, 0.2 M phosphate, and 0.5 M perchlorate + 10 mM chloride solutions.

In a further step, I include the specific adsorption of phosphate anions (Step 8) in the microkinetics. The result in Figure 4.15 shows that the $j_\mathrm{p} - \mathrm{pH}$ relation in phosphate solution is bell-shaped with the peak at pH = 6. This trend is consistent with experimental data on Pt(111) in ref. [157]. However, on polycrystalline Pt, the peak is located at pH = 4.[57, 135] This may be due to the fact that adsorption of phosphate anions on polycrystalline Pt is different from that on Pt(111).[166] In addition, Figure 4.15 shows that the site-blocking effect of adsorbed phosphate is negligible when pH < 4, and becomes significant when pH > 6, in agreement with the concentration profile of $H_2PO_4^-$ versus pH.

Unlike $H_2PO_4^-$, whose concentration is pH-dependent, added Cl^- has a pH-independent concentration. Therefore, the site-blocking effect of Cl^- is significant at any pH. The simulated $j_\mathrm{p} - \mathrm{pH}$ relation in perchlorate solution containing 10 mM Cl^- captures the experimental trend in ref. [57].

4.3.3 Surface charging effects

So far, I have explained the physical origin of the experimentally observed trapezoidal-shaped $j_\mathrm{p} - \mathrm{pH}$ relation in perchlorate solution by combining microkinetic modeling with mass transport effects in the previous section. However, it is noticed that the simulated current density in the plateau region lies by about a factor of three above experimental data.[57, 150] One may assume that this is due to the underestimation of mass transport effects. Therefore, I examine the sensitivity of the diffusion layer thickness.

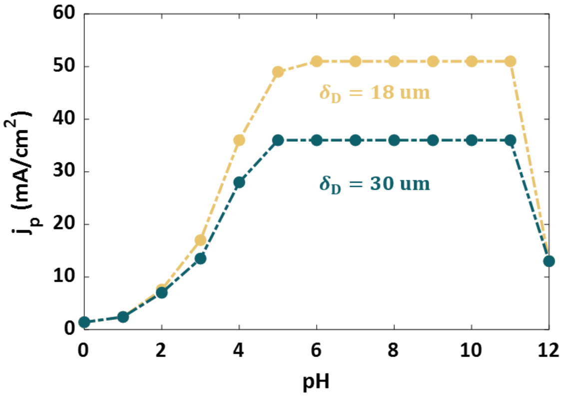

Figure 4.16: Sensitivity of the diffusion layer thickness δ_D in the mass transport corrected $j_p - \text{pH}$ relations.

As shown in Figure 4.16, the simulated current density in the flat region is still about two times higher than the experiments even δ_D is increased to 30 µm, which corresponds to $\omega = 350$ rpm, while the experiments are usually conducted in $\omega > 1000$ rpm.[57] Analytically, it has been found that j_p increases about 4 times if pH increases by 1 when pH < 3, which means that $j_p = 16$ mA/cm^2 at pH = 3 if $j_p = 1$ mA/cm^2 at pH = 1, while experiments give $j_p \approx 3$ mA/cm^2 at pH = 1.[164, 173] Combined, there should be other factors that affect the $j_p - \text{pH}$ relation, and I am about to show that surface charging effects are very likely responsible for this.

The surface charging effects considered in this work contain two aspects, *i.e.*, the Frumkin effects that the reactant concentration and potential at the reaction plane are controlled not only by the mass transport effects, but also by the electrode surface charge density, and the Gibbs free energies of intermediates that depend on it. The Frumkin corrections are firstly considered. The simulated $j_p - \text{pH}$ relation is shown in Figure 4.17.

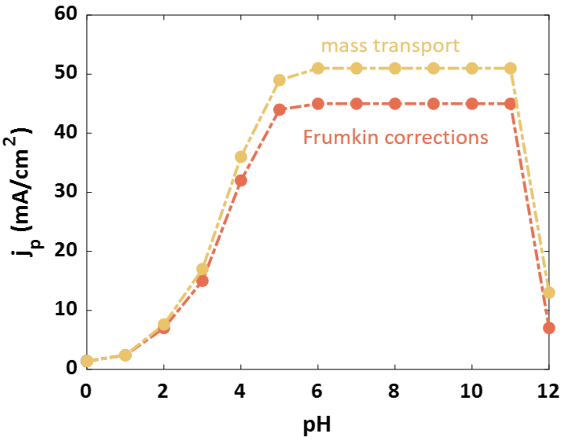

Figure 4.17: Comparison of the $j_\text{p} - \text{pH}$ relation corrected by only mass transport effects and the $j_\text{p} - \text{pH}$ relation corrected by Frumkin corrections in perchlorate solution.

Compared with the case that includes mass transport effects only, the inclusion of Frumkin corrections does not significantly change the trend, but only slightly reduces the activity. This is because the negative surface charge has two competing impacts (as shown in Figure 4.2): it increases the driving force and decreases the surface concentration of HCOO⁻, c_{HCOO^-} (opposite for positive surface charge). The two competing effects more or less cancel each other off in this case. This balance is not sensitive to the key parameters of the electric double layer, ϵ_RP and δ_RP, as shown in Figure 4.18.

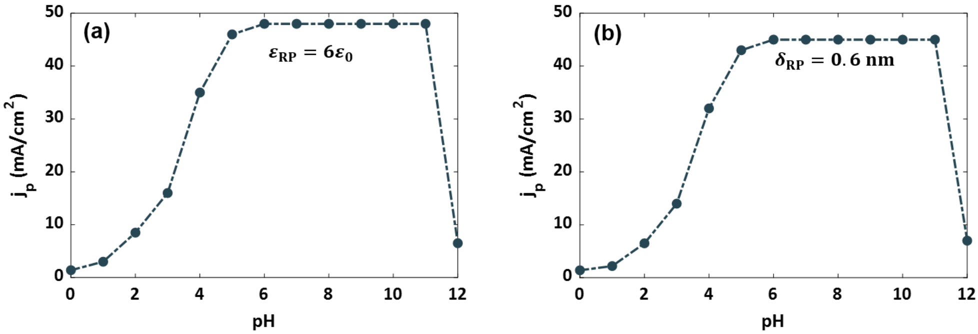

Figure 4.18: Simulated $j_\text{p} - \text{pH}$ relations when (a) $\epsilon_\text{RP} = 6\epsilon_0$ and (b)$\delta_\text{RP} = 0.6$ nm. Other parameters remain unchanged.

Comparison of the $j_\text{p} - \text{pH}$ relations corrected by only mass transport effects and the $j_\text{p} - \text{pH}$

relations corrected by Frumkin corrections in phosphate and chloride-containing solutions is shown in Figure 4.19. In both cases, the quantitative agreement between simulations and experiments does not show significant improvement.

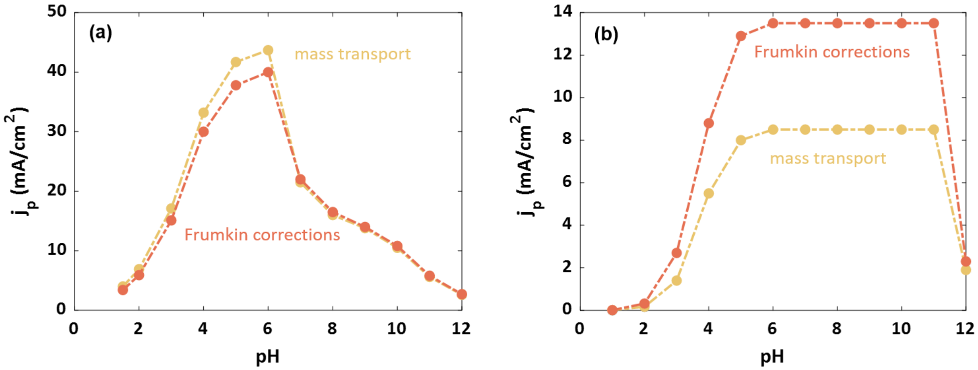

Figure 4.19: Comparison of the j_p − pH relations corrected by only mass transport effects and the j_p − pH relations corrected by Frumkin corrections in (a) phosphate solution and (b) chloride-containing solution.

Recent theoretical studies have shown that the formation energies of adsorbates depend on the surface charge. [11, 77] Moreover, it has been proposed that a positive surface charge is more favorable for formate adsorption. [151, 176] To incorporate surface charge effects beyond Frumkin corrections, I assume that variations in the Gibbs free energies of adsorption for $HCOO_b$ and $HCOO_m$ are linearly correlated with the surface charge density,

$$\Delta\Delta G_{\mathrm{HCOO}_m} = \chi_1 \sigma_{\mathrm{free}} h(\sigma_{\mathrm{free}}) + \chi_2 \sigma_{\mathrm{free}} h(-\sigma_{\mathrm{free}}), \tag{4.48}$$

$$\Delta\Delta G_{\mathrm{HCOO}_b} = \chi_3 \sigma_{\mathrm{free}} h(\sigma_{\mathrm{free}}) + \chi_4 \sigma_{\mathrm{free}} h(-\sigma_{\mathrm{free}}), \tag{4.49}$$

where $h(\sigma_{\mathrm{free}}) = 1$ for $\sigma_{\mathrm{free}} > 0$ and $h(\sigma_{\mathrm{free}}) = 0$ otherwise. The parameters are given as $\chi_1 = \chi_3 = \chi_4 = -3$ eV/(C/m^2), and $\chi_2 = -12$ eV/(C/m^2). Eqs. (4.48) and (4.49) indicate that a positive surface charge density promotes formate adsorption, whereas a negative surface charge density suppresses it. This suppression effect is more pronounced for $HCOO_m$.

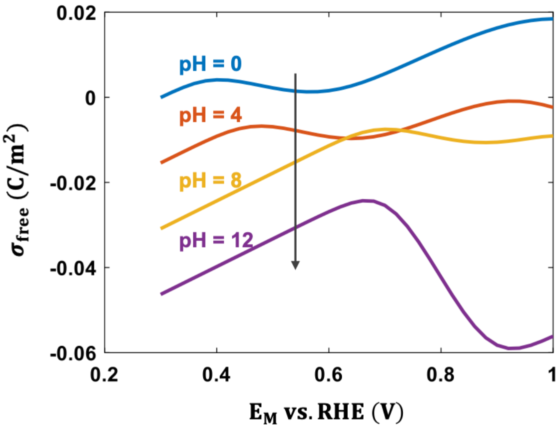

Figure 4.20: Surface charging relations at different pHs. The nonmonotonic features are caused by the chemisorption of $HCOO_b$ and OH_{ad}.

The surface charge becomes more negative with increasing pH (Figure 4.20) for two main reasons. First, ϕ_{pzc} on the RHE scale increases 0.059 with pH increasing by 1 in the absence of adsorption. Second, the adsorption of OH_{ad} is enhanced at higher pH, and these adsorbed hydroxide species carry excess electrons, further contributing to the negative surface charge. Due to the negative shift of the surface charge density, the adsorption of $HCOO_m$ is suppressed and the activity is reduced correspondingly.

As shown in Figure 4.21, a quantitative agreement with experiments is achieved after taking into account the surface charging effect on the free energies of intermediates. Experimental data for polycrystalline Pt are taken from ref. [57], for Pt(111) in perchlorate solution from ref. [176], and for Pt(111) in sulfate solution from ref. [136].

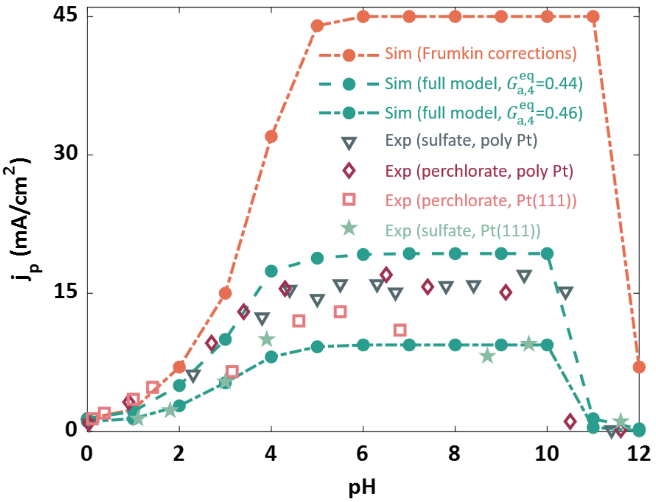

Figure 4.21: Comparison of the simulated $j_p - \mathrm{pH}$ relations and the experimental $j_p - \mathrm{pH}$ relations in perchlorate and sulfate solutions. The concentration of formic acid is 0.1 M. The sensitivity of $G^{\mathrm{eq}}_{\mathrm{a},4}$ is examined to cover the experimental fluctuations.

In addition, the $j_p - \mathrm{pH}$ relation is sensitive to the activation barrier of the key reaction step, $G^{\mathrm{eq}}_{\mathrm{a},4}$. A range of only 0.02 eV for this parameter can cover the experimental fluctuations. This implies that kinetic factors must be taken into account in model-based analyses of electrocatalytic activity.

The polarization curve is also affected by surface charging effects. The surface charging relation is nonmonotonic in the adsorption region (Figure 4.20) since I have considered the partially charged adsorbates in this model. Therefore, the increase of negative surface charge induced by the dipole moment of the adsorbates suppresses the activity by inhibiting the adsorption of formate (eqs. (4.48) and (4.49)).

As shown in Figure 4.22, the simulated $j - E_{\mathrm{M}}$ curve transforms from a bell shape to a camel shape, with a valley in the adsorption region of $\mathrm{HCOO_b}$. This phenomenon is observed in the experiments of FAOR on a polycrystalline Pt electrode.[155] However, it is not observed in experiments on a Pt(111) electrode.[150] The reason for this discrepancy might be the oversimplification of the surface charging effect as accounted for in the Gibbs free energies of adsorbates. Detailed atomic calculations will be needed to describe this relation more accurately.

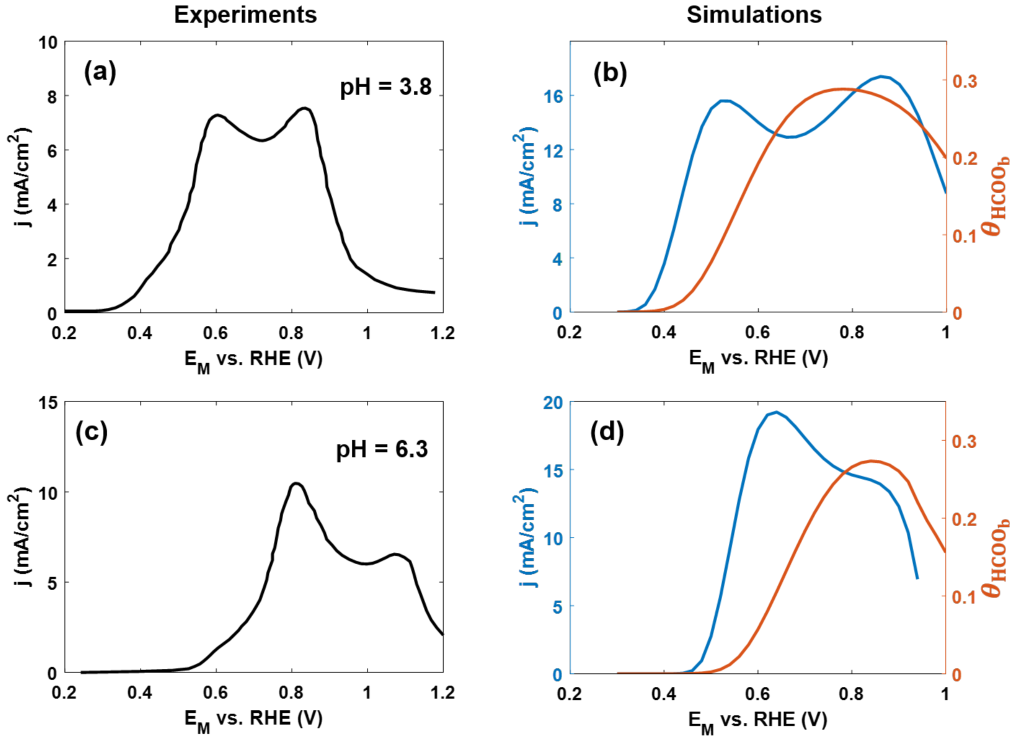

Figure 4.22: Comparisons of the experimental, (a) and (c), and the simulated, (b) and (d), $j - E_M$ curves at pH = 3.8, (a) and (b), and pH = 6.3, (c) and (d). The simulated coverages of $HCOO_b$ are also shown in (b) and (d).

The model is furthermore examined by comparing it with experimental data for formic acid oxidation in phosphate and chloride-containing solutions. Simulations done with the full model closely reproduce the experimental data (data for Pt(111) in phosphate solution are taken from ref. [157] and those for polycrystalline Pt in chloride-containing solution from ref. [57]), as can be seen in Figure 4.23. The quantitative agreement demonstrates that the full model reliably captures the interplay of intrinsic kinetics, mass transport and surface charging effects in different solutions.

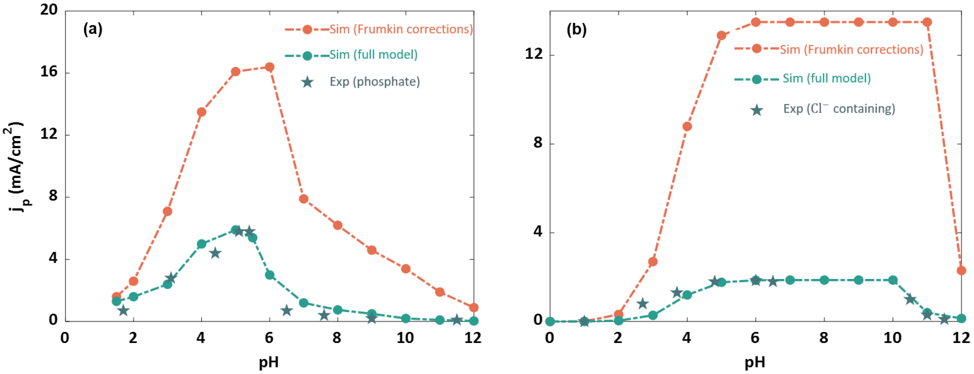

Figure 4.23: Comparison of the simulated j_p − pH relations and the experimental j_p − pH relations in (a) 0.2 M phosphate solution and (b) 0.5 M perchlorate + 10 mM chloride solution. The temperature is 20 ℃ in phosphate solution and 25 ℃ in chloride-containing solution in experiments. The concentration of formic acid is 0.05 M in phosphate solution and 0.1 M in chloride-containing solution.

4.4 A critical review of existing explanations

There have been several explanations for the pH effects in FAOR. Joo *et al.* observed a bell-shaped j_p − pH relation on Pt with the peak at pK$_a$. They explained this phenomenon as follows. When pH < pK$_a$, the concentration of HCOO$^-$ increases with pH, then the activity increases since HCOO$^-$ is the main reactant. When pH > pK$_a$, the site-blocking effect of OH$_{ad}$ adsorption decreases the activity.[135] Brimaud *et al.* also obtained such a bell-shaped relation on Au. However, the OH$_{ad}$ adsorption is negligible on Au in the potential range of interest. They then proposed that the main reactant is not the HCOO$^-$, but the [HCOOH-HCOO$^-$] dimer, which has the highest concentration at pK$_a$.[155]

However, recent experiments have shown that the j_p − pH relation in perchlorate/sulfate solutions presents a trapezoidal shape with a plateau between pH 5 and 10.[57, 137] Neither of the above two mechanisms can explain this phenomenon. Perales-Rondón *et al.* noticed that the bell-shaped j_p − pH relation in ref. [135] is obtained in phosphate solution. Therefore, they stressed the site-blocking effect of adsorbed phosphate anions and attributed the plateau region to the constant concentration of reactant HCOO$^-$.[57, 155] In contrast, Zhang *et al.* proposed that the $j_\mathrm{p} - \mathrm{pH}$ relation in phosphate solution is intrinsic due to the buffering capacity of electrolyte, while the site-blocking effect of adsorbed phosphate anions is not important. They conjectured that the plateau region in non-buffered perchlorate solution might be caused by the local pH shift.[136] However, because their model did not include the effects of local pH and reactant concentration on the microkinetics, they were unable to find a consistent physical explanation of the experimental observation.

In addition, the activity, which is proportional to $k_4 c_{\mathrm{HCOO}^-} \theta_0$, is not solely determined by the reactant concentration or the surface pH. There are three factors, the rate constant, the reactant concentration, and the abundance of free surface sites, that control the activity. Specifically, the rate constant, $k_i \propto \exp\left(\frac{e(E_\mathrm{M} - \phi_\mathrm{RP} - E_i^\mathrm{eq})}{k_B T}\right)$, wherein the driving force is defined as $E_\mathrm{M,\,RHE} - 0.059\mathrm{pH}_\mathrm{bulk} - \phi_\mathrm{RP}$, does not explicitly depend on the surface pH, but the bulk pH of the solution. In addition, ϕ_RP, which is controlled by the surface charge density, changes with pH (Figure 4.24).

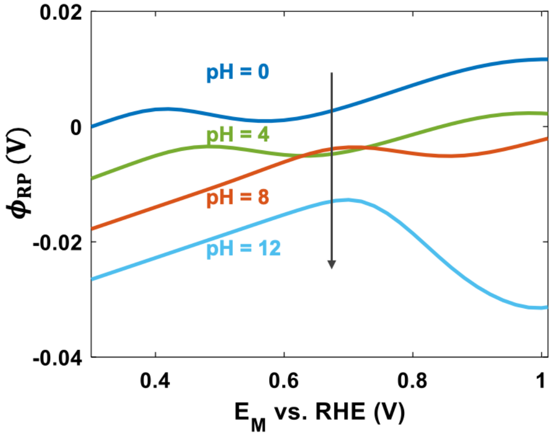

Figure 4.24: Potential at the reaction plane, ϕ_RP, at different E_M and pHs.

The reactant concentration is not only dictated by the surface pH since the dissociation reaction of a weak acid does not remain in equilibrium during the reaction process.[169] As shown in Figure 4.25, the water dissociation deviates from the equilibrium state when pH = 12. The coverage of free sites$\theta_0 = \theta_\mathrm{max} - 2\theta_{\mathrm{HCOO_b}} - \theta_{\mathrm{OH_{ad}}}$ depends not only on $\mathrm{OH_{ad}}$ adsorption, but also on $\mathrm{HCOO_b}$ adsorption.

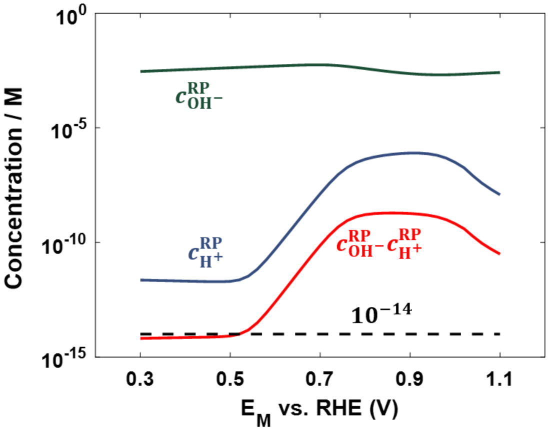

Figure 4.25: $c_{\mathrm{H^+}}^{\mathrm{RP}}$, $c_{\mathrm{OH^-}}^{\mathrm{RP}}$, and $c_{\mathrm{H^+}}^{\mathrm{RP}}c_{\mathrm{OH^-}}^{\mathrm{RP}}$ at pH = 12. $c_{\mathrm{H^+}}c_{\mathrm{OH^-}} = 10^{-14}$ if the water dissociation is in equilibrium, as indicated by the dashed line.

By combining microkinetic modeling and LRE effects, I resolve the discrepancy on the pH effects in FAOR: (1) the intrinsic kinetic $j_{\mathrm{p}} - \mathrm{pH}$ relation exhibits a bell shape with the peak at a pH close to 6; (2) in perchlorate solution, the surface pH remains constant around 4 between pH 5 and 10 due to the mass transport, which inhibits the adsorption of $\mathrm{OH_{ad}}$ and hereby leads to constant $c_{\mathrm{HCOO^-}}$, $E_{\mathrm{p,SHE}}$ and θ_0, thus resulting in the plateau region; (3) in phosphate solution, the site-blocking effect of adsorbed phosphate is negligible when pH < 4, and becomes significant when pH > 6, resulting in a bell-shaped $j_{\mathrm{p}} - \mathrm{pH}$ relation with the peak at pH = 6, but this is not the intrinsic kinetic $j_{\mathrm{p}} - \mathrm{pH}$ relation; in perchlorate solution containing $\mathrm{Cl^-}$, the site-blocking effect of $\mathrm{Cl^-}$ is significant at any pH, resulting in a plateau region between pH 6 and 10; (4) the increasing negative surface charge density with pH suppresses the activity. The latter three aspects further support the crucial message that proper consideration of the LRE is important to correctly predict pH effects in electrocatalytic reactions.

4.5 Conclusions

In this chapter, I have applied the hierarchical framework to understand the pH effects in electrocatalytic reactions. Capabilities of this framework have been examined by studying the pH effects of FAOR. It has been shown that the intrinsic kinetic activity-pH relation of FAOR exhibits a bell shape, but the peak locates at pH = 6, rather than at the pK_a of formic acid, deviating from previous wisdom. Mass transport effects, which keep the surface pH close to 4 for $5 < pH < 10$ and thus inhibit OH_{ad} adsorption, induce the activity-pH relation to transform from a bell shape to a trapezoidal shape. The bell-shaped activity-pH relation with the peak at pH = 6 in phosphate solution is atrributed to the strong adsorption of phosphate anions. The Frumkin corrections include two competing factors, *i.e.*, increasing (decreasing) the driving force and decreasing (increasing) the reactant concentration at the surface. These two factors more or less cancel each other off in this case, and thus do not markedly affect the activity-pH relations. By considering the surface charging effects on the free energies of intermediates, a quantitative agreement with the experimental findings has been obtained. Though this work focuses on the FAOR, the insights obtained in this work are general and readily applicable to other electrocatalytic reactions.

5 Summary and outlook

In this thesis, I have constructed a hierarchical framework for deciphering complex electrocatalytic reactions. This framework encompasses microkinetic modeling, which considers the thermodynamics and kinetics of elementary steps without relying on the critical assumptions inherent in RDS analysis. Concurrently, it dissects the local reaction environment, including local reactant concentrations, pH, potential and electric field, with taking into consideration the intricate EDL details and mass transport phenomena. I have successfully applied this framework to unravel various phenomena in critical reactions such as electrochemical CO_2 reduction, oxygen reduction/evolution reaction, and formic acid oxidation. Based on these applications, vital insights into electrode kinetics have been proposed, which are general for other electrocatalytic reactions and are summarized in the following section.

The chapter is based on the published account article:

- Zhu, X.; Huang, J.; Eikerling, M. *Hierarchical Modeling of the Local Reaction Environment in Electrocatalysis.* Acc. Chem. Res. 2024, 57, 15, 2080–2092.

5.1 Insights into electrode kinetics

5.1.1 Potential-dependent Tafel slopes

Potential-dependent Tafel slopes are prevalent across many reactions,[23] constituting a topic of ongoing discussion in electrocatalysis. The conventional view attributes potential-dependent Tafel slopes to transitions of the RDS. For a sequence of consecutive elementary steps, the

Tafel slope b is related to the “overall transfer coefficient” α,[42]

$$b = \frac{k_B T}{e\alpha} \ln 10 = \frac{59}{\alpha} \text{ mV dec}^{-1} \tag{5.1}$$

at room temperature. Here, $\alpha = n_f + \beta_r n_r$, where n_f is the number of electrons released before the RDS, n_r is the number of electrons involved in the RDS, and β_r is the transfer coefficient of the RDS.

With a predefined reaction mechanism, Eq. (5.1) allows identification of the RDS from the Tafel slope. For example, a Tafel slope of approximately 118 mV/dec is often interpreted as evidence that the first electron transfer is the RDS, a slope of 59 mV/dec suggests that a second chemical step following an electrochemical step is the RDS, and a slope of 39 mV/dec indicates that the second electron transfer step is the RDS. It is important to note that this interpretation assumes $\beta_r = 0.5$, which lacks fundamental justification. Moreover, Marcus theory of electron transfer shows that $\beta_r = \frac{1}{2} - \frac{e\eta}{2\lambda}$, with η being the overpotential and λ is the solvent reorganization energy. This expression implies that β_r varies with overpotential.[177]

Additionally, this conventional view relies on two key assumptions. Firstly, it presupposes a slow step that governs the overall reaction rate, with all other steps in quasi-equilibrium. Secondly, it assumes that the coverage of adsorbates on the catalyst surface is negligible.[23, 24] In some cases, the second assumption is relaxed by determining adsorbate coverages under quasi-equilibrium conditions.[23] However, the quasi-equilibrium conditions implied by both assumptions contradict the fact that the reaction has a net rate and that all elementary steps proceed at the same rate.[46] To overcome these limitations, the development of a microkinetic model that incorporates the thermodynamics and kinetics of all elementary steps is necessary.[46, 48]

The hierarchical framework presented here effectively deciphers potential-dependent Tafel slopes for the OER,[48] ORR,[7] and CO_2RR.[51] A common trend observed is that the Tafel slope increases with overpotential, which can be rationalized through the RDT analysis of intrinsic multistep kinetics.[48]

In addition to the intrinsic multistep kinetics, the LRE also impacts measured Tafel slopes.

Moreover, the influence of the LRE is unavoidable due to the presence of the EDL. I have depicted the LRE effects on the Tafel slopes of the CO_2RR. Mass transport effects tend to increase the Tafel slope with increasing current density, especially for reactions with low reactant concentration in bulk solution (*e.g.*, CO_2RR), due to the concentration decrease at surface. At low overpotentials, the EDL effects are usually predominant. For instance, the intrinsic Tafel slope is 39 mV/dec for the ORR at 0.9 V and the CO_2RR at -0.3 V, while the apparent Tafel slope is close to 59 mV/dec due to the EDL effects.[7, 51] However, 39 mV/dec and 59 mV/dec imply different RDSs in the conventional analysis. Furthermore, lateral interactions from competitive adsorbates and surface charging effects on adsorption energies are revealed as significant influences on the Tafel slope.

Combined, I conclude that the apparent Tafel slope is a composite reaction parameter and may be a poor activity metric as it is influenced by several interacting factors, including the thermodynamics and kinetics of multiple elementary steps, and the LRE effects. The proposed framework aids in revealing the mechanisms behind the apparent potential-dependent Tafel slopes, remedying an oversimplified analysis of the RDS from the Tafel slope.

5.1.2 Cation overcrowding effect

The effects of cation type and concentration have been explored for various electrocatalytic reactions.[52, 54, 178–180] To elucidate the observed cation effects, several mechanisms have been proposed. For instance, Singh *et al.* attributed cation effects in the CO_2RR to cation hydrolysis. Specifically, cations with a smaller hydrated size can buffer the interfacial pH near the cathode more effectively.[54]. Using the modified Poisson-Boltzmann model, Ringe *et al.* demonstrated that the electrode surface charge density is more negative for Cs^+ than for Li^+, which, in turn, enhances the stability of intermediates such as $CO_{2,\,ad}$ and $COOH_{ad}$ in CO_2RR.[27] Similar surface charge effects have also been used to explain cation effects in the HER,[52] ORR,[178], and OER.[179] Huang *et al.* rationalized cation-dependent kinetics of the HER/HOR by considering the influence of cations on the interfacial water structure and H-bonding network.[64] Furthermore, Qin *et al.* proposed that CO_2RR proceeds via an innersphere electron transfer pathway in the presence of alkali cations and, in contrast, through an outer-sphere electron transfer pathway in systems without cations.[180]

Most of the above mechanisms assume that the binding energies of adsorbed intermediates are affected by the electric field, which is then modulated by the cations. Following this line of thermodynamic binding-energy approach, one would expect opposite sequences of cation size effects for metals on the left and right legs of the volcano plot. Specifically, for metals on the right leg of the volcano plot, the activity follows the sequence of $Li^+ < Na^+ < K^+ < Cs^+$. Conversely, for metals on the left leg of the volcano plot, the activity should follow the sequence of $Li^+ > Na^+ > K^+ > Cs^+$. Xue *et al.* observed opposite trends of cation size effects on the HER at Pt or Au, which adsorb hydrogen too strongly or too weakly, respectively.[52] However, such opposite trends are absent for CO_2RR.

In particular, for CO_2RR to HCOOH, Sn is located at the peak of the volcano plot.[95] Thus, enhancing the adsorption of the key intermediate $OCHO_{ad}$ would be expected to decrease the activity. In contrast, since Ag lies on the right leg of the volcano plot, enhancing $OCHO_{ad}$ adsorption should increase its activity. However, experimental data indicate that CO_2RR to HCOOH follows the sequence $Li^+ < Na^+ < K^+ < Cs^+$ at both Sn and Ag.[53] This discrepancy has motivated me to look beyond the binding-energy approach and introduce an electrostatic factor, *i.e.*, the cation overcrowding effect, into consideration. This mechanism was previously acknowledged by Frumkin *et al.* in the study of peroxydisulfate anion reduction when the surface charge is very negative.[9] My works demonstrated that the cation overcrowding effect offers an alternative or at least complementary explanation to previously observed cation effects.

The overcrowding effect describes how cations accumulating exceedingly near the negatively charged surface diminish the space for reactants and influence the local electrostatic potential and electric field.[51, 68] Specifically, the free space for species other than cations is $1 - N_A d_c^3 c_c$, with d_c being the effective diameter and c_c the concentration of cations. Theory and simulations accounting for the cation size have shown that this effect is more pronounced for cations with a larger hydrated size,[51, 68] as depicted in Figure 5.1(a). Consequently, the concentration of reactant, *e.g.*, CO_2 for CO_2RR and OH^- for OER, at the surface follows the order $Li^+ < Na^+ < K^+$ (Figure 5.1(b)), which results in the same order of activity. Despite its simplicity, this rationale was shown to be relevant in explaining the cation effects in the CO_2RR at Ag (Figure 5.1(c)),[51] and the OER at Ni-based catalysts.[68]

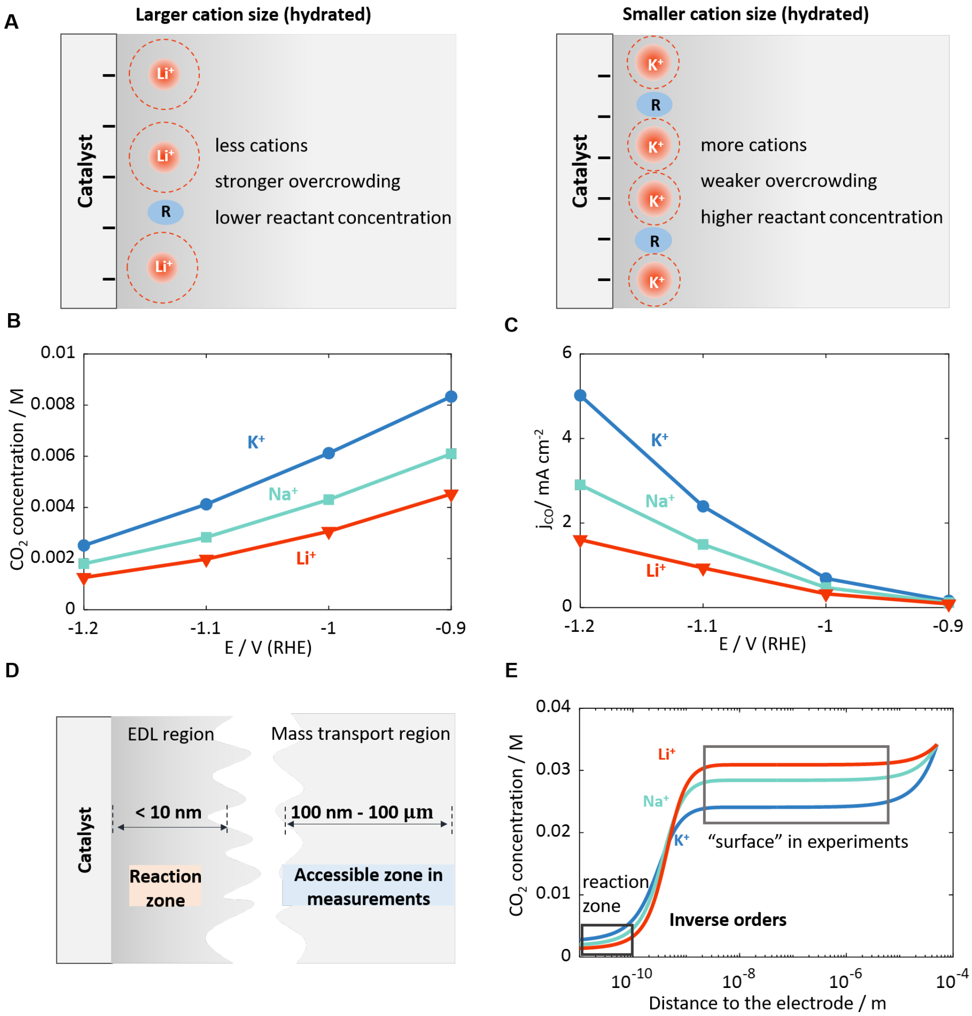

Figure 5.1: (a) Schematic illustration of the cation overcrowding effect in electrocatalysis. Cations accumulated near the negatively charged surface diminish the space for reactants, resulting in a decrease in the reactant concentration. Moreover, this effect is more pronounced for cations with a larger hydrated size. (b-c) Cation effects on CO_2RR at Ag in 0.1 M $KHCO_3$/$NaHCO_3$/$LiHCO_3$ solutions: (b) CO_2 concentration at the reaction plane; (c) model-derived CO current density. (d) Schematic illustration of the difference between the most probable reaction zone and the accessible zone in experimental measurements. (e) Distribution of CO_2 concentration in solutions at -1.2 V versus RHE.

Various experimental techniques have been employed to detect the local reactant concentration or the local pH, such as surface enhanced infrared absorption spectroscopy, Raman spectroscopy, and scanning electrochemical microscopy.[33–35] However, it is essential to acknowledge that in these experiments, the term “surface” typically refers to somewhere within the diffusion layer. The distance of the probe position to the catalyst surface varies from hundreds of nanometers to hundreds of micrometers, which is still far from the reaction zone within the EDL. This discrepancy in the designation of the “surface” concentration, as depicted in Figure 5.1(d), may lead to confusion. For instance, Malkani *et al.* observed that the “surface” CO_2 concentration follows the sequence of $Li^+ > Na^+ > K^+$. At first glance, this shows the opposite trend to my simulations in Figure 5.1(b). This superficial inconsistency can be resolved by distinguishing the “surface” concentration in experiments and in simulations. As shown in Figure 5.1(e), the simulations show that the CO_2 concentration in the diffusion layer, which corresponds to the “surface” in experiments, follows the order of $Li^+ > Na^+ > K^+$. The concentration in this diffusion region is determined by mass transport effects; the above concentration sequence is a direct consequence of the fact that the current density of the CO_2RR follows the sequence $Li^+ < Na^+ < K^+$. However, electrostatic interactions and the cation overcrowding effect dominate within the EDL, leading to the inverse order of CO_2 concentration.

5.1.3 pH effects

The influence of solution pH on electrocatalytic reactions is multifaceted, including intrinsic pH effects and local pH effects. In broad terms, changes in solution pH impact reaction kinetics by inducing shifts in both proton activity and absolute potential of the electrode (*i.e.*, versus the SHE). Given that many electrocatalytic reactions involve proton and electron transfers, variations in pH play a pivotal role. Moreover, the proton donor or oxidant involved in the reaction may transition from proton/hydroxyl to water molecules when pH varies in a wide range. Additionally, for reactants engaged in acid-alkaline equilibrium, such as formic acid and formate, the concentration of the reactant is influenced by the solution pH. These influences are termed as intrinsic pH effects as they collectively shape the overall properties of electrocatalytic reactions. These intrinsic effects have been widely employed to understand pH effects in various electrocatalytic reactions, including CO_2RR,[28] electrochemical carbon monoxide reduction,[65] HER,[50] ORR,[128] OER,[58] and FAOR.[57, 135]

In addition to these intrinsic pH effects, I have emphasized the importance of considering local pH effects, namely, the pH effects arising in the LRE.[14, 68, 69] On one hand, the local pH shifts with the reaction rate due to the production/consumption of protons, and this pH shift is more pronounced in the intermediate pH range than in strongly acidic or alkaline conditions.[136] On the other hand, the pzc on the reversible hydrogen electrode (RHE) scale increases with pH,

$$E_{\text{pzc,RHE}} = E_{\text{pzc,SHE}} + 0.0592\text{pH}. \tag{5.2}$$

Here, $E_{\text{pzc, SHE}}$ is the pzc on the SHE scale. Consequently, the surface charge is more negative at higher pH at the same potential versus RHE, resulting in the change of EDL properties.

Thermodynamic equilibrium conditions predict that the OER activity should be independent of pH on the RHE scale since it is a proton-coupled electron transfer (PCET) reaction.[58] However, experiments show that the activity increases with pH.[58] This discrepancy can be understood by considering the EDL effects.

For the electrochemical oxidation of anions, such as OH^- in the OER, the negative surface charge induces two competing effects, as per Frumkin effects: it increases the driving force and decreases the surface concentration of anions (opposite for positive surface charge). The outcome of these competing effects determines the promotion or inhibition of activity. Furthermore, Frumkin effects depend on the pH, as it modulates the surface charge, *i.e.*, the surface charge is more negative at higher pH. For the case of the OER at NiOOH, the effect of increasing the driving force is more pronounced. As a result, the activity exhibits an increase as the surface charge becomes more negative, and thus at higher pH.[68]

However, Frumkin effects have been revealed as being insignificant in the case of FAOR, as the competing effects more or less cancel each other out. Instead, the mass transport-induced local pH shift emerges as a crucial factor that influences observed pH effects.[14] The complexity of pH effects in this model system arises from multiple interacting factors, including pH-dependent thermodynamics and reaction kinetics of multiple steps, and pH-dependent LRE effects. This situation has motivated me to build a hierarchical model in an incremental manner, which allows different factors that control the overall pH effect to be disentangled. The analysis began with exclusive consideration of the microkinetics in perchlorate solutions, in which the specific adsorption of electrolyte anions can be avoided. Based on the modeling at this level, the intrinsic activity-pH relation without accounting for the LRE was obtained, which is bell-shaped and inconsistent with the observed trapezoidal shape. The mass transport effects was then added to the model. It has been found that the pH at the reaction plane ($\mathrm{pH_{RP}}$) is much lower than the pH in the bulk solution ($\mathrm{pH_{bulk}}$), as the FAOR generates protons. Moreover, the $\mathrm{pH_{RP}}$ remains almost constant at $\mathrm{pH_{RP}} = 4$ in the range of $5 < \mathrm{pH_{bulk}} < 11$. This local pH shift induces a transformation of the activity-pH relation from bell shape to trapezoidal shape, yielding qualitative agreement with the experimental trend. For the activity-pH relation in phosphate solution, there are two additional electrolyte effects, *i.e.*, the buffering effect and the specific adsorption of phosphate anions. By incorporating both effects, the model captured the experimental trends in phosphate solution, with the activity being lower than that in perchlorate solution and the activity-pH relation being bell-shaped. Furthermore, the site-blocking effect of the specific adsorption of phosphate anions was revealed to be the determining factor.

Given the above analysis, the importance of considering the variation of LRE when the solution pH changes is underscored. Fluctuations in local pH and surface charging relation induced by pH changes could be the determining factors of apparent pH effects.

5.2 Outlook

Until now, the framework has been applied to planar electrodes with static structure and operated in the steady state. Several important extensions to the framework should be made in the stride towards realism with realistic structure and dynamic conditions.[181]

Firstly, time-dependent methods, *e.g.*, pulsed electrolysis, have been acknowledged to be effective in improving the activity and selectivity of CO2RR[182] and ORR.[183] Secondly, the catalyst has been revealed to dynamically reconstruct, instead of being static, during reactions.[184] Thirdly, electrochemical energy conversion technologies typically employ supported nanoparticle catalysts, requiring a proper treatment of synergistic effects due to the overlap of the EDLs from catalytic nanoparticles and support material.[185] Fourthly, the catalyst in gas diffusion electrodes is not simply embedded into an aqueous electrolyte (as usually considered in model studies) but it is surrounded by a thin ionomer film that creates a water-filled nanogap region around the catalyst.[186] This interfacial configuration is crucial for understanding LRE effects at catalyst-ionomer interfaces.

Future endeavours in addressing these complexities should take advantage of recent developments in theory and modelling of electrochemical phenomena. For instance, the thermodynamics and kinetics of elementary steps involved in the microkinetic model can be calculated with increasing accuracy using grand-canonical DFT.[187] In addition, Marcus-Hush-Chidsey theory should be employed instead of the Butler–Volmer equation to describe the elementary electron-transfer kinetics at high overpotentials[177] and in the case of the solvent reorganization energy changing markedly with electrode potential.[142] Furthermore, the mean field EDL model can be refined and complemented by incorporating atomistic and molecular details obtained from first-principles calculations.[26] Finally, development of high-performance computation infrastructure and rapidly emerging machine learning techniques pave the way towards handling complexities of real-world electrocatalytic systems.[188] For instance, modern supercomputing platforms now enable large-scale AIMD simulations for the electrochemical interfaces that were previously computationally prohibitive.[189]

Bibliography

[1] Z. W. Seh, J. Kibsgaard, C. F. Dickens, I. Chorkendorff, J. K. Nørskov, and T. F. Jaramillo. *Combining theory and experiment in electrocatalysis: Insights into materials design*. Science, 355(6321), eaad4998, 2017.

[2] *World Energy Outlook 2024*. Technical report, International Energy Agency, 2024.

[3] S. Nitopi, E. Bertheussen, S. B. Scott, X. Liu, A. K. Engstfeld, S. Horch, B. Seger, I. E. Stephens, K. Chan, C. Hahn, et al. *Progress and perspectives of electrochemical CO2 reduction on copper in aqueous electrolyte*. Chemical reviews, 119(12), 7610–7672, 2019.

[4] M. Chatenet, B. G. Pollet, D. R. Dekel, F. Dionigi, J. Deseure, P. Millet, R. D. Braatz, M. Z. Bazant, M. Eikerling, I. Staffell, et al. *Water electrolysis: from textbook knowledge to the latest scientific strategies and industrial developments*. Chemical society reviews, 51 (11), 4583–4762, 2022.

[5] X. Zhu, J. Huang, and M. Eikerling. *Hierarchical modeling of the local reaction environment in electrocatalysis*. Accounts of Chemical Research, 57(15), 2080–2092, 2024.

[6] J. Huang, A. Malek, J. Zhang, and M. H. Eikerling. *Non-monotonic surface charging behavior of platinum: a paradigm change*. The Journal of Physical Chemistry C, 120 (25), 13587–13595, 2016.

[7] J. Huang, J. Zhang, and M. Eikerling. *Unifying theoretical framework for deciphering the oxygen reduction reaction on platinum*. Physical Chemistry Chemical Physics, 20(17), 11776–11786, 2018.

[8] A. Frumkin. *Wasserstoffüberspannung und Struktur der Doppelschicht*. Zeitschrift für physikalische Chemie, 164(1), 121–133, 1933.

[9] A. Frumkin, N. Nikolaeva-Fedorovich, N. Berezina, and K. E. Keis. *The electroreduction of the S2O82- anion*. Journal of Electroanalytical Chemistry and Interfacial Electrochemistry, 58(1), 189–201, 1975.

[10] J. Gu, S. Liu, W. Ni, W. Ren, S. Haussener, and X. Hu. *Modulating electric field distribution by alkali cations for CO2 electroreduction in strongly acidic medium*. Nature Catalysis, 5(4), 268–276, 2022.

[11] S. Ringe, C. G. Morales-Guio, L. D. Chen, M. Fields, T. F. Jaramillo, C. Hahn, and K. Chan. *Double layer charging driven carbon dioxide adsorption limits the rate of electrochemical carbon dioxide reduction on Gold*. Nature communications, 11(1), 33, 2020.

[12] X.-Y. Li, T. Wang, Y.-C. Cai, Z.-D. Meng, J.-W. Nan, J.-Y. Ye, J. Yi, D.-P. Zhan, N. Tian, Z.-Y. Zhou, et al. *Mechanism of cations suppressing proton diffusion kinetics for electrocatalysis*. Angewandte Chemie, 135(14), e202218669, 2023.

[13] L. Rebollar, S. Intikhab, N. J. Oliveira, Y. Yan, B. Xu, I. T. McCrum, J. D. Snyder, and M. H. Tang. *“Beyond adsorption” descriptors in hydrogen electrocatalysis*. ACS catalysis, 10 (24), 14747–14762, 2020.

[14] X. Zhu, J. Huang, and M. Eikerling. *pH effects in a model electrocatalytic reaction disentangled*. JACS Au, 3(4), 1052–1064, 2023.

[15] J. Resasco, F. Abild-Pedersen, C. Hahn, Z. Bao, M. T. Koper, and T. F. Jaramillo. *Enhanc-*

ing the connection between computation and experiments in electrocatalysis. Nature Catalysis, 5(5), 374–381, 2022.

[16] B. Hammer and J. K. Norskov. *Why gold is the noblest of all the metals*. Nature, 376 (6537), 238–240, 1995.

[17] J. K. Nørskov, J. Rossmeisl, A. Logadottir, L. Lindqvist, J. R. Kitchin, T. Bligaard, and H. Jonsson. *Origin of the overpotential for oxygen reduction at a fuel-cell cathode*. The Journal of Physical Chemistry B, 108(46), 17886–17892, 2004.

[18] F. Calle-Vallejo, D. Loffreda, M. T. Koper, and P. Sautet. *Introducing structural sensitivity into adsorption–energy scaling relations by means of coordination numbers*. Nature chemistry, 7(5), 403–410, 2015.

[19] A. R. Zeradjanin, P. Narangoda, J. Masa, and R. Schlogl. *What controls activity trends of electrocatalytic hydrogen evolution reaction? Activation Energy Versus Frequency Factor*. ACS Catalysis, 12(19), 11597–11605, 2022.

[20] K. S. Exner. *A universal descriptor for the screening of electrode materials for multiple-electron processes: beyond the thermodynamic overpotential*. ACS Catalysis, 10(21), 12607–12617, 2020.

[21] Y. Zhang, J. Huang, and M. Eikerling. *Criterion for finding the optimal electrocatalyst at any overpotential*. Electrochimica Acta, 400, 139413, 2021.

[22] A. M. Gómez-Marín, R. Rizo, and J. M. Feliu. *Oxygen reduction reaction at Pt single crystals: a critical overview*. Catalysis Science & Technology, 4(6), 1685–1698, 2014.

[23] T. Shinagawa, A. T. Garcia-Esparza, and K. Takanabe. *Insight on Tafel slopes from a microkinetic analysis of aqueous electrocatalysis for energy conversion*. Scientific reports, 5(1), 13801, 2015.

[24] M. T. Koper. *Analysis of electrocatalytic reaction schemes: distinction between rate-determining and potential-determining steps*. Journal of Solid State Electrochemistry, 17, 339–344, 2013.

[25] M. Dunwell, W. Luc, Y. Yan, F. Jiao, and B. Xu. *Understanding surface-mediated electrochemical reactions: CO2 reduction and beyond*. Acs Catalysis, 8(9), 8121–8129, 2018.

[26] P. Li, Y. Jiao, J. Huang, and S. Chen. *Electric double layer effects in electrocatalysis: Insights from ab initio simulation and hierarchical continuum modeling*. JACS Au, 3(10), 2640–2659, 2023.

[27] S. Ringe, E. L. Clark, J. Resasco, A. Walton, B. Seger, A. T. Bell, and K. Chan. *Understanding cation effects in electrochemical CO 2 reduction*. Energy & Environmental Science, 12(10), 3001–3014, 2019.

[28] A. Xu, N. Govindarajan, G. Kastlunger, S. Vijay, and K. Chan. *Theories for electrolyte effects in CO2 electroreduction*. Accounts of Chemical Research, 55(4), 495–503, 2022.

[29] L. M. Pinto, E. Spohr, P. Quaino, E. Santos, and W. Schmickler. *Why silver deposition is so fast: Solving the enigma of metal deposition*. Angewandte Chemie International Edition, 52(30), 7883–7885, 2013.

[30] J. Huang. *Mixed quantum-classical treatment of electron transfer at electrocatalytic interfaces: Theoretical framework and conceptual analysis*. The Journal of Chemical Physics, 153(16), 2020.

[31] V. G. Levich. *Theory of the nonequilibrium double layer*. In *Dokl. Akad. Nauk SSSR*, volume 67, page 309, 1949.

[32] A. Z. Weber and J. Newman. *Modeling transport in polymer-electrolyte fuel cells*. Chemical reviews, 104(10), 4679–4726, 2004.

[33] M. C. Monteiro and M. T. Koper. *Measuring local pH in electrochemistry*. Current opinion in electrochemistry, 25, 100649, 2021.

[34] M. C. Monteiro, A. Mirabal, L. Jacobse, K. Doblhoff-Dier, S. C. Barton, and M. T. Koper. *Time-resolved local pH measurements during CO2 reduction using scanning electrochemical microscopy: Buffering and tip effects*. Jacs Au, 1(11), 1915–1924, 2021.

[35] A. S. Malkani, J. Anibal, and B. Xu. *Cation effect on interfacial CO2 concentration in the electrochemical CO2 reduction reaction*. ACS Catalysis, 10(24), 14871–14876, 2020.

[36] A. Botz, J. Clausmeyer, D. Öhl, T. Tarnev, D. Franzen, T. Turek, and W. Schuhmann. *Local Activities of Hydroxide and Water Determine the Operation of Silver-Based Oxygen Depolarized Cathodes*. Angewandte Chemie International Edition, 57(38), 12285–12289, 2018.

[37] I. C. Man, H.-Y. Su, F. Calle-Vallejo, H. A. Hansen, J. I. Martínez, N. G. Inoglu, J. Kitchin, T. F. Jaramillo, J. K. Nørskov, and J. Rossmeisl. *Universality in oxygen evolution electrocatalysis on oxide surfaces*. ChemCatChem, 3(7), 1159–1165, 2011.

[38] B. Hammer and J. K. Nørskov. *Electronic factors determining the reactivity of metal surfaces*. Surface science, 343(3), 211–220, 1995.

[39] F. Calle-Vallejo, J. Tymoczko, V. Colic, Q. H. Vu, M. D. Pohl, K. Morgenstern, D. Loffreda, P. Sautet, W. Schuhmann, and A. S. Bandarenka. *Finding optimal surface sites on heterogeneous catalysts by counting nearest neighbors*. Science, 350(6257), 185–189, 2015.

[40] S. Trasatti. *Work function, electronegativity, and electrochemical behaviour of metals: III. Electrolytic hydrogen evolution in acid solutions*. Journal of Electroanalytical Chemistry and Interfacial Electrochemistry, 39(1), 163–184, 1972.

[41] D. Zhou, J. Wei, Z.-D. He, M.-L. Xu, Y.-X. Chen, and J. Huang. *Combining single crystal experiments and microkinetic modeling in disentangling thermodynamic, kinetic, and double-layer factors influencing oxygen reduction*. The Journal of Physical Chemistry C, 124(25), 13672–13678, 2020.

[42] R. Guidelli, R. G. Compton, J. M. Feliu, E. Gileadi, J. Lipkowski, W. Schmickler, and S. Trasatti. *Defining the transfer coefficient in electrochemistry: An assessment (IUPAC Technical Report)*. Pure and Applied Chemistry, 86(2), 245–258, 2014.

[43] S. Kozuch and J. M. Martin. *The rate-determining step is dead. Long live the rate-determining state!* ChemPhysChem, 12(8), 1413–1418, 2011.

[44] D. Sepa, M. Vojnovic, L. M. Vracar, and A. Damjanovic. *Different views regarding the kinetics and mechanisms of oxygen reduction at Pt and Pd electrodes*. Electrochimica Acta, 32(1), 129–134, 1987.

[45] A. Holewinski and S. Linic. *Elementary mechanisms in electrocatalysis: revisiting the ORR Tafel slope*. Journal of The Electrochemical Society, 159(11), H864, 2012.

[46] A. T. Marshall and L. Vaisson-Béthune. *Avoid the quasi-equilibrium assumption when evaluating the electrocatalytic oxygen evolution reaction mechanism by Tafel slope analysis*. Electrochemistry Communications, 61, 23–26, 2015.

[47] A. M. Limaye, J. S. Zeng, A. P. Willard, and K. Manthiram. *Bayesian data analysis reveals no preference for cardinal Tafel slopes in CO2 reduction electrocatalysis*. Nature communications, 12(1), 703, 2021.

[48] J. Huang, X. Zhu, and M. Eikerling. *The rate-determining term of electrocatalytic reactions with first-order kinetics*. Electrochimica Acta, 393, 139019, 2021.

[49] M. R. Singh, J. D. Goodpaster, A. Z. Weber, M. Head-Gordon, and A. T. Bell. *Mechanistic insights into electrochemical reduction of CO2 over Ag using density functional theory and transport models*. Proceedings of the National Academy of Sciences, 114(42), E8812–E8821, 2017.

[50] P. S. Lamoureux, A. R. Singh, and K. Chan. *pH effects on hydrogen evolution and oxidation over Pt (111): insights from first-principles*. Acs Catalysis, 9(7), 6194–6201,

2019.

[51] X. Zhu, J. Huang, and M. Eikerling. *Electrochemical CO2 reduction at silver from a local perspective*. ACS catalysis, 11(23), 14521–14532, 2021.

[52] S. Xue, B. Garlyyev, S. Watzele, Y. Liang, J. Fichtner, M. D. Pohl, and A. S. Bandarenka. *Influence of alkali metal cations on the hydrogen evolution reaction activity of Pt, Ir, Au, and Ag electrodes in alkaline electrolytes*. ChemElectroChem, 5(17), 2326–2329, 2018.

[53] J. Resasco, L. D. Chen, E. Clark, C. Tsai, C. Hahn, T. F. Jaramillo, K. Chan, and A. T. Bell. *Promoter effects of alkali metal cations on the electrochemical reduction of carbon dioxide*. Journal of the American Chemical Society, 139(32), 11277–11287, 2017.

[54] M. R. Singh, Y. Kwon, Y. Lum, J. W. Ager III, and A. T. Bell. *Hydrolysis of electrolyte cations enhances the electrochemical reduction of CO2 over Ag and Cu*. Journal of the American chemical society, 138(39), 13006–13012, 2016.

[55] J. D. Michael, E. L. Demeter, S. M. Illes, Q. Fan, J. R. Boes, and J. R. Kitchin. *Alkaline electrolyte and Fe impurity effects on the performance and active-phase structure of NiOOH thin films for OER catalysis applications*. The Journal of Physical Chemistry C, 119(21), 11475–11481, 2015.

[56] G. Marcandalli, M. C. Monteiro, A. Goyal, and M. T. Koper. *Electrolyte effects on CO2 electrochemical reduction to CO*. Accounts of chemical research, 55(14), 1900–1911, 2022.

[57] J. V. Perales-Rondon, S. Brimaud, J. Solla-Gullon, E. Herrero, R. J. Behm, and J. M. Feliu. *Further insights into the formic acid oxidation mechanism on platinum: pH and anion adsorption effects*. Electrochimica Acta, 180, 479–485, 2015.

[58] L. Giordano, B. Han, M. Risch, W. T. Hong, R. R. Rao, K. A. Stoerzinger, and Y. Shao-Horn. *pH dependence of OER activity of oxides: current and future perspectives*. Catalysis Today, 262, 2–10, 2016.

[59] T. F. Fuller and J. Newman. *Water and thermal management in solid-polymer-electrolyte fuel cells*. Journal of the Electrochemical Society, 140(5), 1218, 1993.

[60] M. Eikerling and A. Kornyshev. *Modelling the performance of the cathode catalyst layer of polymer electrolyte fuel cells*. Journal of Electroanalytical Chemistry, 453(1-2), 89–106, 1998.

[61] M. Eikerling and A. Kornyshev. *Electrochemical impedance of the cathode catalyst layer in polymer electrolyte fuel cells*. Journal of Electroanalytical Chemistry, 475(2), 107–123, 1999.

[62] W. Sheng, H. A. Gasteiger, and Y. Shao-Horn. *Hydrogen oxidation and evolution reaction kinetics on platinum: acid vs alkaline electrolytes*. Journal of The Electrochemical Society, 157(11), B1529, 2010.

[63] J. C. Fornaciari, L.-C. Weng, S. M. Alia, C. Zhan, T. A. Pham, A. T. Bell, T. Ogitsu, N. Danilovic, and A. Z. Weber. *Mechanistic understanding of pH effects on the oxygen evolution reaction*. Electrochimica acta, 405, 139810, 2022.

[64] B. Huang, R. R. Rao, S. You, K. Hpone Myint, Y. Song, Y. Wang, W. Ding, L. Giordano, Y. Zhang, T. Wang, et al. *Cation-and pH-dependent hydrogen evolution and oxidation reaction kinetics*. Jacs Au, 1(10), 1674–1687, 2021.

[65] G. Kastlunger, L. Wang, N. Govindarajan, H. H. Heenen, S. Ringe, T. Jaramillo, C. Hahn, and K. Chan. *Using pH dependence to understand mechanisms in electrochemical CO reduction*. ACS Catalysis, 12(8), 4344–4357, 2022.

[66] M. C. Monteiro, F. Dattila, B. Hagedoorn, R. García-Muelas, N. López, and M. T. Koper. *Absence of CO2 electroreduction on copper, gold and silver electrodes without metal cations in solution*. Nature Catalysis, 4(8), 654–662, 2021.

[67] X. Zhu and J. Huang. *Modeling electrocatalytic oxidation of formic acid at platinum*. Journal of The Electrochemical Society, 167(1), 013515, 2019.

[68] J. Huang, M. Li, M. J. Eslamibidgoli, M. Eikerling, and A. Groß. *Cation overcrowding effect on the oxygen evolution reaction*. Jacs Au, 1(10), 1752–1765, 2021.

[69] J. Huang, V. Climent, A. Groß, and J. M. Feliu. *Understanding surface charge effects in electrocatalysis. Part 2: Hydrogen peroxide reactions at platinum*. Chinese Journal of Catalysis, 43(11), 2837–2849, 2022.

[70] L. Zhang and J. Huang. *Understanding surface charge effects in electrocatalysis. Part I: peroxodisulfate reduction at Pt (111)*. The Journal of Physical Chemistry C, 124(31), 16951–16960, 2020.

[71] L. Zhang, J. Cai, Y. Chen, and J. Huang. *Modelling electrocatalytic reactions with a concerted treatment of multistep electron transfer kinetics and local reaction conditions*. Journal of Physics: Condensed Matter, 33(50), 504002, 2021.

[72] H.-G. Qin, F.-Z. Li, Y.-F. Du, L.-F. Yang, H. Wang, Y.-Y. Bai, M. Lin, and J. Gu. *Quantitative understanding of cation effects on the electrochemical reduction of CO2 and H+ in acidic solution*. ACS Catalysis, 13(2), 916–926, 2022.

[73] E. F. Johnson, E. Boutin, S. Liu, and S. Haussener. *Pathways to enhance electrochemical CO 2 reduction identified through direct pore-level modeling*. EES catalysis, 1(5), 704–719, 2023.

[74] H. A. Hansen, V. Viswanathan, and J. K. Nørskov. *Unifying kinetic and thermodynamic analysis of 2 e–and 4 e–reduction of oxygen on metal surfaces*. The Journal of Physical Chemistry C, 118(13), 6706–6718, 2014.

[75] T. Bligaard, J. K. Nørskov, S. Dahl, J. Matthiesen, C. H. Christensen, and J. Sehested. *The Brønsted–Evans–Polanyi relation and the volcano curve in heterogeneous catalysis*. Journal of catalysis, 224(1), 206–217, 2004.

[76] D. Bohra, I. Ledezma-Yanez, G. Li, W. de Jong, E. A. Pidko, and W. A. Smith. *Lateral adsorbate interactions inhibit HCOO- while promoting CO selectivity for CO2 electrocatalysis on silver*. Angewandte Chemie, 131(5), 1359–1363, 2019.

[77] L. D. Chen, M. Urushihara, K. Chan, and J. K. Nørskov. *Electric field effects in electrochemical CO2 reduction*. Acs Catalysis, 6(10), 7133–7139, 2016.

[78] N. M. Marković, R. R. Adžić, B. Cahan, and E. Yeager. *Structural effects in electrocatalysis: oxygen reduction on platinum low index single-crystal surfaces in perchloric acid solutions*. Journal of Electroanalytical Chemistry, 377(1-2), 249–259, 1994.

[79] N. Markovic, H. Gasteiger, and P. N. Ross. *Kinetics of oxygen reduction on Pt (hkl) electrodes: implications for the crystallite size effect with supported Pt electrocatalysts*. Journal of the Electrochemical Society, 144(5), 1591, 1997.

[80] N. M. Markovic, H. A. Gasteiger, and P. N. Ross. *Oxygen reduction on platinum low-index single-crystal surfaces in alkaline solution: rotating ring diskPt (hkl) studies*. The Journal of Physical Chemistry, 100(16), 6715–6721, 1996.

[81] N. Marković, B. Grgur, and P. N. Ross. *Temperature-dependent hydrogen electrochemistry on platinum low-index single-crystal surfaces in acid solutions*. The Journal of Physical Chemistry B, 101(27), 5405–5413, 1997.

[82] M. S. Kilic, M. Z. Bazant, and A. Ajdari. *Steric effects in the dynamics of electrolytes at large applied voltages. I. Double-layer charging*. Physical Review E—Statistical, Nonlinear, and Soft Matter Physics, 75(2), 021502, 2007.

[83] M. S. Kilic, M. Z. Bazant, and A. Ajdari. *Steric effects in the dynamics of electrolytes at large applied voltages. II. Modified Poisson-Nernst-Planck equations*. Physical Review E—Statistical, Nonlinear, and Soft Matter Physics, 75(2), 021503, 2007.

[84] A. A. Kornyshev. *Double-layer in ionic liquids: paradigm change?* The Journal of Physical Chemistry B, 111(20), 5545–5557, 2007.

[85] Y. A. Budkov. *Nonlocal statistical field theory of dipolar particles in electrolyte solutions*. Journal of Physics: Condensed Matter, 30(34), 344001, 2018.

[86] Y. Zhang and J. Huang. *Treatment of ion-size asymmetry in lattice-gas models for electrical double layer*. The Journal of Physical Chemistry C, 122(50), 28652–28664, 2018.

[87] A. Abrashkin, D. Andelman, and H. Orland. *Dipolar Poisson-Boltzmann equation: ions and dipoles close to charge interfaces*. Physical review letters, 99(7), 077801, 2007.

[88] J. Huang. *Zooming into the inner helmholtz plane of Pt (111)–aqueous solution interfaces: Chemisorbed water and partially charged ions*. JACS Au, 3(2), 550–564, 2023.

[89] M. L. Foresti, M. Innocenti, F. Forni, and R. Guidelli. *Electrosorption valency and partial charge transfer in halide and sulfide adsorption on Ag (111)*. Langmuir, 14(24), 7008–7016, 1998.

[90] E. F. Johnson, E. Boutin, and S. Haussener. *Surface charge boundary condition often misused in CO2 reduction models*. The Journal of Physical Chemistry C, 127(37), 18784–18790, 2023.

[91] J. Koutecky and V. Levich. *The use of a rotating disk electrode in the studies of electrochemical kinetics and electrolytic processes*. Zh. Fiz. Khim, 32, 1565–1575, 1958.

[92] P. Sebastián-Pascual, S. Mezzavilla, I. E. Stephens, and M. Escudero-Escribano. *Structure-sensitivity and electrolyte effects in CO2 electroreduction: from model studies to applications*. ChemCatChem, 11(16), 3626–3645, 2019.

[93] M. G. Kibria, J. P. Edwards, C. M. Gabardo, C.-T. Dinh, A. Seifitokaldani, D. Sinton, and E. H. Sargent. *Electrochemical CO2 reduction into chemical feedstocks: from mechanistic electrocatalysis models to system design*. Advanced Materials, 31(31), 1807166, 2019.

[94] H. A. Hansen, J. B. Varley, A. A. Peterson, and J. K. Nørskov. *Understanding trends in the electrocatalytic activity of metals and enzymes for CO2 reduction to CO*. The journal of physical chemistry letters, 4(3), 388–392, 2013.

[95] J. T. Feaster, C. Shi, E. R. Cave, T. Hatsukade, D. N. Abram, K. P. Kuhl, C. Hahn, J. K. Nørskov, and T. F. Jaramillo. *Understanding selectivity for the electrochemical reduction of carbon dioxide to formic acid and carbon monoxide on metal electrodes*. Acs Catalysis, 7(7), 4822–4827, 2017.

[96] J. Rosen, G. S. Hutchings, Q. Lu, S. Rivera, Y. Zhou, D. G. Vlachos, and F. Jiao. *Mechanistic insights into the electrochemical reduction of CO2 to CO on nanostructured Ag surfaces*. Acs Catalysis, 5(7), 4293–4299, 2015.

[97] M. Dunwell, X. Yang, B. P. Setzler, J. Anibal, Y. Yan, and B. Xu. *Examination of near-electrode concentration gradients and kinetic impacts on the electrochemical reduction of CO2 using surface-enhanced infrared spectroscopy*. Acs Catalysis, 8(5), 3999–4008, 2018.

[98] A. Goyal, G. Marcandalli, V. A. Mints, and M. T. Koper. *Competition between CO2 reduction and hydrogen evolution on a gold electrode under well-defined mass transport conditions*. Journal of the American Chemical Society, 142(9), 4154–4161, 2020.

[99] A. S. Varela, M. Kroschel, T. Reier, and P. Strasser. *Controlling the selectivity of CO2 electroreduction on copper: The effect of the electrolyte concentration and the importance of the local pH*. Catalysis Today, 260, 8–13, 2016.

[100] E. L. Clark and A. T. Bell. *Direct observation of the local reaction environment during the electrochemical reduction of CO2*. Journal of the American Chemical Society, 140(22), 7012–7020, 2018.

[101] B. Kim, S. Ma, H.-R. M. Jhong, and P. J. Kenis. *Influence of dilute feed and pH on electrochemical reduction of CO2 to CO on Ag in a continuous flow electrolyzer*. Electrochimica Acta, 166, 271–276, 2015.

[102] N. Gupta, M. Gattrell, and B. MacDougall. *Calculation for the cathode surface concentrations in the electrochemical reduction of CO2 in KHCO3 solutions*. Journal of applied electrochemistry, 36(2), 161–172, 2006.

[103] M. R. Singh, E. L. Clark, and A. T. Bell. *Effects of electrolyte, catalyst, and membrane composition and operating conditions on the performance of solar-driven electrochemical reduction of carbon dioxide*. Physical Chemistry Chemical Physics, 17(29), 18924–18936, 2015.

[104] E. L. Clark, S. Ringe, M. Tang, A. Walton, C. Hahn, T. F. Jaramillo, K. Chan, and A. T. Bell. *Influence of Atomic Surface Structure on the Activity of Ag for the Electrochemical Reduction of CO2 to CO*. ACS catalysis, 9(5), 4006–4014, 2019.

[105] N. Hoshi, M. Kato, and Y. Hori. *Electrochemical reduction of CO2 on single crystal electrodes of silver Ag (111), Ag (100) and Ag (110)*. Journal of electroanalytical chemistry, 440(1-2), 283–286, 1997.

[106] J. A. Dean. *Lange's handbook of chemistry. McGraw-Hill*. Inc., New York, page 11, 1999.

[107] T. Hatsukade, K. P. Kuhl, E. R. Cave, D. N. Abram, and T. F. Jaramillo. *Insights into the electrocatalytic reduction of CO 2 on metallic silver surfaces*. Physical Chemistry Chemical Physics, 16(27), 13814–13819, 2014.

[108] M. Dunwell, Q. Lu, J. M. Heyes, J. Rosen, J. G. Chen, Y. Yan, F. Jiao, and B. Xu. *The central role of bicarbonate in the electrochemical reduction of carbon dioxide on gold*. Journal of the American Chemical Society, 139(10), 3774–3783, 2017.

[109] S. Back, M. S. Yeom, and Y. Jung. *Active sites of Au and Ag nanoparticle catalysts for CO2 electroreduction to CO*. Acs Catalysis, 5(9), 5089–5096, 2015.

[110] J. S. Yoo, R. Christensen, T. Vegge, J. K. Nørskov, and F. Studt. *Theoretical insight into the trends that guide the electrochemical reduction of carbon dioxide to formic acid*. ChemSusChem, 9(4), 358–363, 2016.

[111] M. Liu, Y. Pang, B. Zhang, P. De Luna, O. Voznyy, J. Xu, X. Zheng, C. T. Dinh, F. Fan, C. Cao, et al. *Enhanced electrocatalytic CO2 reduction via field-induced reagent concentration*. Nature, 537(7620), 382–386, 2016.

[112] N. J. Firet and W. A. Smith. *Probing the reaction mechanism of CO2 electroreduction over Ag films via operando infrared spectroscopy*. Acs Catalysis, 7(1), 606–612, 2017.

[113] X. Liu, P. Schlexer, J. Xiao, Y. Ji, L. Wang, R. B. Sandberg, M. Tang, K. S. Brown, H. Peng, S. Ringe, et al. *pH effects on the electrochemical reduction of CO (2) towards C2 products on stepped copper*. Nature communications, 10(1), 32, 2019.

[114] J. Wellendorff, K. T. Lundgaard, A. Møgelhøj, V. Petzold, D. D. Landis, J. K. Nørskov, T. Bligaard, and K. W. Jacobsen. *Density functionals for surface science: Exchange-correlation model development with Bayesian error estimation*. Physical Review B—Condensed Matter and Materials Physics, 85(23), 235149, 2012.

[115] J. Huang. *On obtaining double-layer capacitance and potential of zero charge from voltammetry*. Journal of Electroanalytical Chemistry, 870, 114243, 2020.

[116] A. Malek and M. H. Eikerling. *Chemisorbed oxygen at Pt (111): a DFT study of structural and electronic surface properties*. Electrocatalysis, 9, 370–379, 2018.

[117] D. Bohra, J. H. Chaudhry, T. Burdyny, E. A. Pidko, and W. A. Smith. *Modeling the electrical double layer to understand the reaction environment in a CO 2 electrocatalytic system*. Energy & Environmental Science, 12(11), 3380–3389, 2019.

[118] L.-C. Weng, A. T. Bell, and A. Z. Weber. *Modeling gas-diffusion electrodes for CO 2*

reduction. Physical Chemistry Chemical Physics, 20(25), 16973–16984, 2018.

[119] Y. Chen, C. W. Li, and M. W. Kanan. *Aqueous CO2 reduction at very low overpotential on oxide-derived Au nanoparticles*. Journal of the American Chemical Society, 134(49), 19969–19972, 2012.

[120] A. Wuttig, Y. Yoon, J. Ryu, and Y. Surendranath. *Bicarbonate is not a general acid in Au-catalyzed CO2 electroreduction*. Journal of the American Chemical Society, 139(47), 17109–17113, 2017.

[121] A. Wuttig, M. Yaguchi, K. Motobayashi, M. Osawa, and Y. Surendranath. *Inhibited proton transfer enhances Au-catalyzed CO2-to-fuels selectivity*. Proceedings of the National Academy of Sciences, 113(32), E4585–E4593, 2016.

[122] J. Greeley, T. F. Jaramillo, J. Bonde, I. Chorkendorff, and J. K. Nørskov. *Computational high-throughput screening of electrocatalytic materials for hydrogen evolution*. Nature materials, 5(11), 909–913, 2006.

[123] E. Santos, P. Quaino, and W. Schmickler. *Theory of electrocatalysis: hydrogen evolution and more*. Physical Chemistry Chemical Physics, 14(32), 11224–11233, 2012.

[124] J. K. Nørskov, T. Bligaard, J. Rossmeisl, and C. H. Christensen. *Towards the computational design of solid catalysts*. Nature chemistry, 1(1), 37–46, 2009.

[125] A. Kulkarni, S. Siahrostami, A. Patel, and J. K. Nørskov. *Understanding catalytic activity trends in the oxygen reduction reaction*. Chemical reviews, 118(5), 2302–2312, 2018.

[126] J. Huang, P. Li, and S. Chen. *Quantitative understanding of the sluggish kinetics of hydrogen reactions in alkaline media based on a microscopic Hamiltonian model for the Volmer step*. The Journal of Physical Chemistry C, 123(28), 17325–17334, 2019.

[127] V. Briega-Martos, E. Herrero, and J. M. Feliu. *Effect of pH and water structure on the oxygen reduction reaction on platinum electrodes*. Electrochimica Acta, 241, 497–509, 2017.

[128] M. F. Li, L. W. Liao, D. F. Yuan, D. Mei, and Y.-X. Chen. *pH effect on oxygen reduction reaction at Pt (1 1 1) electrode*. Electrochimica Acta, 110, 780–789, 2013.

[129] L. Wang, S. A. Nitopi, E. Bertheussen, M. Orazov, C. G. Morales-Guio, X. Liu, D. C. Higgins, K. Chan, J. K. Nørskov, C. Hahn, et al. *Electrochemical carbon monoxide reduction on polycrystalline copper: effects of potential, pressure, and pH on selectivity toward multicarbon and oxygenated products*. Acs Catalysis, 8(8), 7445–7454, 2018.

[130] M. T. Koper. *Volcano activity relationships for proton-coupled electron transfer reactions in electrocatalysis*. Topics in Catalysis, 58, 1153–1158, 2015.

[131] P. Rodriguez, N. Garcia-Araez, and M. T. Koper. *Self-promotion mechanism for CO electrooxidation on gold*. Physical Chemistry Chemical Physics, 12(32), 9373–9380, 2010.

[132] N. Govindarajan, A. Xu, and K. Chan. *How pH affects electrochemical processes*. Science, 375(6579), 379–380, 2022.

[133] Y. Kwon, S. C. Lai, P. Rodriguez, and M. T. Koper. *Electrocatalytic oxidation of alcohols on gold in alkaline media: base or gold catalysis?* Journal of the American Chemical Society, 133(18), 6914–6917, 2011.

[134] S. C. Lai, S. E. Kleijn, F. T. Öztürk, V. C. van Rees Vellinga, J. Koning, P. Rodriguez, and M. T. Koper. *Effects of electrolyte pH and composition on the ethanol electro-oxidation reaction*. Catalysis Today, 154(1-2), 92–104, 2010.

[135] J. Joo, T. Uchida, A. Cuesta, M. T. Koper, and M. Osawa. *Importance of acid–base equilibrium in electrocatalytic oxidation of formic acid on platinum*. Journal of the American Chemical Society, 135(27), 9991–9994, 2013.

[136] M.-K. Zhang, Z. Wei, W. Chen, M.-L. Xu, J. Cai, and Y.-X. Chen. *Bell shape vs volcano*

shape pH dependent kinetics of the electrochemical oxidation of formic acid and formate, intrinsic kinetics or local pH shift? Electrochimica Acta, 363, 137160, 2020.

[137] Z. Wei, M. K. Zhang, B. Q. Zhu, J. Cai, and Y.-X. Chen. *Mechanistic insight into formic acid/formate oxidation at the Au (111) electrode: implications from the pH effect and H/D kinetic isotope effect*. The Journal of Physical Chemistry C, 126(29), 11987–12002, 2022.

[138] L. Rebollar, S. Intikhab, J. D. Snyder, and M. H. Tang. *Determining the viability of hydroxide-mediated bifunctional HER/HOR mechanisms through single-crystal voltammetry and microkinetic modeling*. Journal of The Electrochemical Society, 165(15), J3209–J3221, 2018.

[139] G. Marcandalli, A. Goyal, and M. T. Koper. *Electrolyte effects on the faradaic efficiency of CO2 reduction to CO on a gold electrode*. ACS catalysis, 11(9), 4936–4945, 2021.

[140] S. R. Kelly, C. Kirk, K. Chan, and J. K. Nørskov. *Electric field effects in oxygen reduction kinetics: rationalizing pH dependence at the Pt (111), Au (111), and Au (100) electrodes*. The Journal of Physical Chemistry C, 124(27), 14581–14591, 2020.

[141] B. B. Blizanac, C. A. Lucas, M. E. Gallagher, M. Arenz, P. N. Ross, and N. Marković. *Anion adsorption, CO oxidation, and oxygen reduction reaction on a Au (100) surface: The pH effect*. The Journal of Physical Chemistry B, 108(2), 625–634, 2004.

[142] I. Ledezma-Yanez, W. D. Z. Wallace, P. Sebastián-Pascual, V. Climent, J. M. Feliu, and M. Koper. *Interfacial water reorganization as a pH-dependent descriptor of the hydrogen evolution rate on platinum electrodes*. Nature Energy, 2(4), 1–7, 2017.

[143] W. Chen, M.-K. Zhang, B.-Y. Liu, J. Cai, and Y.-X. Chen. *Challenges and recent progress in unraveling the intrinsic pH effect in electrocatalysis*. Current Opinion in Electrochemistry, 34, 101003, 2022.

[144] A. Miki, S. Ye, and M. Osawa. *Surface-enhanced IR absorption on platinum nanoparticles: an application to real-time monitoring of electrocatalytic reactions*. Chemical Communications, (14), 1500–1501, 2002.

[145] H.-F. Wang and Z.-P. Liu. *Formic acid oxidation at Pt/H2O interface from periodic DFT calculations integrated with a continuum solvation model*. The Journal of Physical Chemistry C, 113(40), 17502–17508, 2009.

[146] S. Sakong and A. Groß. *The importance of the electrochemical environment in the electro-oxidation of methanol on Pt (111)*. ACS catalysis, 6(8), 5575–5586, 2016.

[147] Y.-X. Chen, M. Heinen, Z. Jusys, and R. J. Behm. *Bridge-bonded formate: active intermediate or spectator species in formic acid oxidation on a Pt film electrode?* Langmuir, 22(25), 10399–10408, 2006.

[148] Y. X. Chen, M. Heinen, Z. Jusys, and R. J. Behm. *Kinetics and mechanism of the electrooxidation of formic acid—spectroelectrochemical studies in a flow cell*. Angewandte Chemie International Edition, 45(6), 981–985, 2006.

[149] J. Scaranto and M. Mavrikakis. *HCOOH decomposition on Pt (111): A DFT study*. Surface Science, 648, 201–211, 2016.

[150] A. Ferre-Vilaplana, J. V. Perales-Rondón, C. Buso-Rogero, J. M. Feliu, and E. Herrero. *Formic acid oxidation on platinum electrodes: a detailed mechanism supported by experiments and calculations on well-defined surfaces*. Journal of Materials Chemistry A, 5(41), 21773–21784, 2017.

[151] C. Busó-Rogero, A. Ferre-Vilaplana, E. Herrero, and J. M. Feliu. *The role of formic acid/formate equilibria in the oxidation of formic acid on Pt (111)*. Electrochemistry Communications, 98, 10–14, 2019.

[152] J. Joo, T. Uchida, A. Cuesta, M. T. Koper, and M. Osawa. *The effect of pH on the electrocatalytic oxidation of formic acid/formate on platinum: A mechanistic study by*

surface-enhanced infrared spectroscopy coupled with cyclic voltammetry. Electrochimica Acta, 129, 127–136, 2014.

[153] M. J. Salamon, V. Briega-Martos, A. Cuesta, and E. Herrero. *Insight into the role of adsorbed formate in the oxidation of formic acid from pH-dependent experiments with Pt single-crystal electrodes*. Journal of Electroanalytical Chemistry, 925, 116886, 2022.

[154] V. Grozovski, V. Climent, E. Herrero, and J. M. Feliu. *Intrinsic activity and poisoning rate for HCOOH oxidation on platinum stepped surfaces*. Physical Chemistry Chemical Physics, 12(31), 8822–8831, 2010.

[155] S. Brimaud, J. Solla-Gullón, I. Weber, J. M. Feliu, and R. J. Behm. *Formic acid electrooxidation on noble-metal electrodes: role and mechanistic implications of pH, surface structure, and anion adsorption*. ChemElectroChem, 1(6), 1075–1083, 2014.

[156] H. Lee, S. E. Habas, G. A. Somorjai, and P. Yang. *Localized Pd overgrowth on cubic Pt nanocrystals for enhanced electrocatalytic oxidation of formic acid*. Journal of the American Chemical Society, 130(16), 5406–5407, 2008.

[157] A. Abdelrahman, J. M. Hermann, and L. A. Kibler. *Electrocatalytic oxidation of formate and formic acid on platinum and gold: study of pH dependence with phosphate buffers*. Electrocatalysis, 8, 509–517, 2017.

[158] X. Chen, L. P. Granda-Marulanda, I. T. McCrum, and M. T. Koper. *How palladium inhibits CO poisoning during electrocatalytic formic acid oxidation and carbon dioxide reduction*. Nature communications, 13(1), 38, 2022.

[159] M. Wakisaka, Y. Udagawa, H. Suzuki, H. Uchida, and M. Watanabe. *Structural effects on the surface oxidation processes at Pt single-crystal electrodes studied by X-ray photoelectron spectroscopy*. Energy & Environmental Science, 4(5), 1662–1666, 2011.

[160] A. J. Bard, L. R. Faulkner, and H. S. White. *Electrochemical methods: fundamentals and applications*. John Wiley & Sons, 2022.

[161] V. Grozovski, F. J. Vidal-Iglesias, E. Herrero, and J. M. Feliu. *Adsorption of formate and its role as intermediate in formic acid oxidation on platinum electrodes*. ChemPhysChem, 12(9), 1641–1644, 2011.

[162] T. L. Silbaugh, E. M. Karp, and C. T. Campbell. *Energetics of formic acid conversion to adsorbed formates on Pt (111) by transient calorimetry*. Journal of the American Chemical Society, 136(10), 3964–3971, 2014.

[163] J. Lović, A. Tripković, S. L. Gojković, K. D. Popović, D. Tripković, P. Olszewski, and A. Kowal. *Kinetic study of formic acid oxidation on carbon-supported platinum electrocatalyst*. Journal of electroanalytical chemistry, 581(2), 294–302, 2005.

[164] J. V. Perales-Rondón, E. Herrero, and J. M. Feliu. *Effects of the anion adsorption and pH on the formic acid oxidation reaction on Pt (111) electrodes*. Electrochimica Acta, 140, 511–517, 2014.

[165] V. Tripković, E. Skúlason, S. Siahrostami, J. K. Nørskov, and J. Rossmeisl. *The oxygen reduction reaction mechanism on Pt (1 1 1) from density functional theory calculations*. Electrochimica Acta, 55(27), 7975–7981, 2010.

[166] R. Gisbert, G. García, and M. T. Koper. *Adsorption of phosphate species on polyoriented Pt and Pt (1 1 1) electrodes over a wide range of pH*. Electrochimica Acta, 55(27), 7961–7968, 2010.

[167] N. Li and J. Lipkowski. *Chronocoulometric studies of chloride adsorption at the Pt (111) electrode surface*. Journal of Electroanalytical Chemistry, 491(1-2), 95–102, 2000.

[168] H. Hashiba, L.-C. Weng, Y. Chen, H. K. Sato, S. Yotsuhashi, C. Xiang, and A. Z. Weber. *Effects of electrolyte buffer capacity on surface reactant species and the reaction rate of CO2 in electrochemical CO2 reduction*. The Journal of Physical Chemistry C, 122(7), 3719–3726, 2018.

[169] J. C. Bui, E. W. Lees, L. M. Pant, I. V. Zenyuk, A. T. Bell, and A. Z. Weber. *Continuum modeling of porous electrodes for electrochemical synthesis*. Chemical reviews, 122(12), 11022–11084, 2022.

[170] S. R. Heil, M. Holz, T. M. Kastner, and H. Weingärtner. *Self-diffusion of the perchlorate ion in aqueous electrolyte solutions measured by 35 Cl NMR spin–echo experiments*. Journal of the Chemical Society, Faraday Transactions, 91(12), 1877–1880, 1995.

[171] D. Hochfilzer, A. Xu, J. E. Sørensen, J. L. Needham, K. Krempl, K. K. Toudahl, G. Kastlunger, I. Chorkendorff, K. Chan, and J. Kibsgaard. *Transients in electrochemical CO reduction explained by mass transport of buffers*. ACS Catalysis, 12(9), 5155–5161, 2022.

[172] R. Martínez-Hincapié, V. Climent, and J. M. Feliu. *Peroxodisulfate reduction as a probe to interfacial charge*. Electrochemistry Communications, 88, 43–46, 2018.

[173] A. Betts, V. Briega-Martos, A. Cuesta, and E. Herrero. *Adsorbed formate is the last common intermediate in the dual-path mechanism of the electrooxidation of formic acid*. ACS Catalysis, 10(15), 8120–8130, 2020.

[174] Y. Wei, X. Q. Zuo, Z. Da He, W. Chen, C. H. Lin, J. Cai, M. Sartin, and Y.-X. Chen. *The mechanisms of HCOOH/HCOO–oxidation on Pt electrodes: Implication from the pH effect and H/D kinetic isotope effect*. Electrochemistry Communications, 81, 1–4, 2017.

[175] J. M. Hermann, A. Abdelrahman, T. Jacob, and L. A. Kibler. *The effect of pH and anion adsorption on formic acid oxidation on Au (111) electrodes*. Electrochimica Acta, 385, 138279, 2021.

[176] A. Ferre-Vilaplana, J. V. Perales-Rondon, J. M. Feliu, and E. Herrero. *Understanding the effect of the adatoms in the formic acid oxidation mechanism on Pt (111) electrodes*. Acs Catalysis, 5(2), 645–654, 2015.

[177] E. Laborda, M. C. Henstridge, C. Batchelor-McAuley, and R. G. Compton. *Asymmetric Marcus–Hush theory for voltammetry*. Chemical Society Reviews, 42(12), 4894–4905, 2013.

[178] J. L. Hubner, L. E. Lucchetti, H. N. Nong, D. I. Sharapa, B. Paul, M. Kroschel, J. Kang, D. Teschner, S. Behrens, F. Studt, et al. *Cation effects on the acidic oxygen reduction reaction at carbon surfaces*. ACS Energy Letters, 9(4), 1331–1338, 2024.

[179] C. Yang, O. Fontaine, J.-M. Tarascon, and A. Grimaud. *Chemical recognition of active oxygen species on the surface of oxygen evolution reaction electrocatalysts*. Angewandte Chemie, 129(30), 8778–8782, 2017.

[180] X. Qin, H. A. Hansen, K. Honkala, and M. M. Melander. *Cation-induced changes in the inner-and outer-sphere mechanisms of electrocatalytic CO2 reduction*. Nature Communications, 14(1), 7607, 2023.

[181] C. Zhang, J. Cheng, Y. Chen, M. K. Chan, Q. Cai, R. P. Carvalho, C. F. Marchiori, D. Brandell, C. M. Araujo, M. Chen, et al. *2023 Roadmap on molecular modelling of electrochemical energy materials*. Journal of Physics: Energy, 5(4), 041501, 2023.

[182] R. Casebolt, K. Levine, J. Suntivich, and T. Hanrath. *Pulse check: Potential opportunities in pulsed electrochemical CO2 reduction*. Joule, 5(8), 1987–2026, 2021.

[183] Y. Ding, W. Zhou, J. Li, J. Wang, L. Xie, X. Meng, J. Gao, F. Sun, G. Zhao, and Y. Qin. *Revealing the in situ dynamic regulation of the interfacial microenvironment induced by pulsed electrocatalysis in the oxygen reduction reaction*. ACS Energy Letters, 8(7), 3122–3130, 2023.

[184] H. Jiang, Q. He, Y. Zhang, and L. Song. *Structural self-reconstruction of catalysts in electrocatalysis*. Accounts of chemical research, 51(11), 2968–2977, 2018.

[185] J. Huang, J. Zhang, and M. H. Eikerling. *Particle proximity effect in nanoparticle electrocatalysis: surface charging and electrostatic interactions*. The Journal of Physical

Chemistry C, 121(9), 4806–4815, 2017.

[186] S. Woo, S. Lee, A. Z. Taning, T.-H. Yang, S.-H. Park, and S.-D. Yim. *Current understanding of catalyst/ionomer interfacial structure and phenomena affecting the oxygen reduction reaction in cathode catalyst layers of proton exchange membrane fuel cells*. Current Opinion in Electrochemistry, 21, 289–296, 2020.

[187] M. M. Melander. *Grand canonical ensemble approach to electrochemical thermodynamics, kinetics, and model Hamiltonians*. Current Opinion in Electrochemistry, 29, 100749, 2021.

[188] T. Mou, H. S. Pillai, S. Wang, M. Wan, X. Han, N. M. Schweitzer, F. Che, and H. Xin. *Bridging the complexity gap in computational heterogeneous catalysis with machine learning*. Nature Catalysis, 6(2), 122–136, 2023.

[189] Y. Zhou, Y. Ouyang, Y. Zhang, Q. Li, and J. Wang. *Machine learning assisted simulations of electrochemical interfaces: recent progress and challenges*. The Journal of Physical Chemistry Letters, 14(9), 2308–2316, 2023.

List of publications

Journal articles

- **Zhu, X.**; Huang, J.; Eikerling, M. *Electrochemical CO2 Reduction at Silver from a Local Perspective.* ACS Catal. 2021, 11(23), 14521–14532, doi: 10.1021/acscatal.1c04791.
- Huang, J.; **Zhu, X.**; Eikerling, M. *The Rate-Determining Term of Electrocatalytic Reactions with First-Order Kinetics.* Electrochim. Acta 2021, 393, 139019, doi: 10.1016/j.electacta.2021.139019.
- **Zhu, X.**; Huang, J.; Eikerling, M. *pH Effects in a Model Electrocatalytic Reaction Disentangled.* JACS Au 2023, 3(4), 1052–1064, doi: 10.1021/jacsau.2c00662.
- **Zhu, X.**; Huang, J.; Eikerling, M. *Hierarchical Modeling of the Local Reaction Environment in Electrocatalysis.* Acc. Chem. Res. 2024, 57, 15, 2080–2092, doi: 10.1021/acs.accounts.4c00234.

Conference talks

- **Zhu, X.**; Huang, J.; Eikerling, M. *Theoretical Modeling of the Local Reaction Environment at Interfaces for Formic Acid Oxidation*. 32nd Topical ISE Meeting, June 2022 (Stockholm, Sweden).
- **Zhu, X.**; Huang, J.; Eikerling, M. *pH Effects in a Model Electrocatalytic Reaction Disentangled*. 74th Annual Meeting of ISE, September 2023 (Lyon, France).
- **Zhu, X.**; Huang, J.; Eikerling, M. *Disentangling pH effects in Electrocatalytic Reactions*. 244th ECS Meeting, October 2023 (Gothenburg, Sweden).
- **Zhu, X.**; Huang, J.; Eikerling, M. *pH Effects in a Model Electrocatalytic Reaction Disentangled*. European Fuel Cell Forum 2023, July 2023 (Lucerne, Switzerland).

Conference posters

- **Zhu, X.**; Huang, J.; Eikerling, M. *Theoretical Understanding of the Potential Dependent Tafel Slopes of CO_2 Reduction at Ag*. 748. WE-Heraeus-Seminar, May 2021 (Virtual).
- **Zhu, X.**; Huang, J.; Eikerling, M. *Theoretical Modeling of the Local Reaction Environment at Interfaces for Formic Acid Oxidation*. 31st Topical ISE Meeting, May 2022 (Aachen, Germany).
- **Zhu, X.**; Huang, J.; Eikerling, M. *Hierarchical Modeling of the Local Reaction Environment in Electrocatalysis*. Faraday Discussion on New horizons in Nanoelectrochemistry, October 2024 (Nanjing, China).

Acknowledgments

First and foremost, I would like to thank my supervisor, Prof. Michael Eikerling. He has been incredibly supportive throughout this journey, not only academically but also personally. The period of 2020–2021 was particularly difficult for me: confined at home during the pandemic, my progress was slow and often discouraging. Michael never pressured me; instead, he offered constant encouragement and understanding. With his support, I was able to overcome this period and complete work that I believe to be meaningful.

I am deeply grateful to Prof. Jun Huang, who introduced me to the field of electrochemistry. It was thanks to his reference letter that I received the PhD offer from Michael. Over the past seven years, including four years at the same institute, I have learned a lot from him, not only about electrochemistry, but also about how to be a better person.

Beyond them, I extend my heartfelt thanks to every member of IET-3 (formerly IEK-13). The warmth of this group, the open and stimulating discussions, and the delicious cakes have made this journey feel like home.

These years in Germany have not been only about research. They have been filled with moments that make up life itself. My girlfriend, Wenqian, has a younger heart than I do. With her, I experienced many firsts—my first concert and my first cruise. These moments have kept me from growing old on the inside.

Here, I also found friendship. For six years, Yufan Zhang was my officemate. Now, as we both step into new chapters of our lives, I am grateful that we are each doing well. During my time at IEK-13, Dechun Si, Oskar Cheong, and Aikai Yang left me with many warm memories. At IET-3, Zengming Zhang, Weiqiang Tang, Chenkun Li, Lulu Zhang, and Kangjun Duan offered generous help in both life and research. I am also thankful to my roommates of four years, Congcong Zheng and Fengben Xi, with whom I shared meals and drinks.

Finally, I would like to thank my family. Their unwavering support has been my strongest pillar throughout these years of studying far from home.

Life is just beginning, a final line for myself: 莫听穿林打叶声，何妨吟啸且徐行。

Band / Volume 683
Assessment of erosion in recessed areas of fusion devices using multi-scale computer simulations
S. W. Rode (2025), viii, 196 pp
ISBN: 978-3-95806-867-4

Band / Volume 684
Europäische Energiewende – Deutschland im Herzen Europas
T. Klütz, P. Dunkel, T. Busch, J. Linssen, D. Stolten (2025), IV, 56 pp
ISBN: 978-3-95806-870-4

Band / Volume 685
Performance and stability of solar cells and modules: From laboratory characterization to field data analysis
T. S. Vaas (2025), xvii, 146 pp
ISBN: 978-3-95806-871-1

Band / Volume 686
From Soil Legacy to Wheat Yield Decline: Studying the Plant-Soil Feedback Mechanisms in Wheat Rotations
N. Kaloterakis (2025), XXIX, 188 pp
ISBN: 978-3-95806-874-2

Band / Volume 687
Entwicklung von Beschichtungsverfahren für die Herstellung von Wärmedämmschichten auf additiv gefertigten Komponenten
M. Rüßmann (2026), ix, 188 pp
ISBN: 978-3-95806-877-3

Band / Volume 688
Model Perovskite Oxide Electrocatalysts for the Oxygen Evolution Reaction and their Material Sustainability Evaluation
L. Heymann (2026), vi, 174 pp
ISBN: 978-3-95806-878-0

Band / Volume 689
Development of an oxygen ion conducting solid oxide electrolysis cell based on gadolinium-doped cerium oxide as fuel electrode and electrolyte material
D. Ramler (2026), ix, 162 pp
ISBN: 978-3-95806-879-7

Band / Volume 690
Design of Local Multi-Energy Systems: Impact of Coupled Energy Vector Integration and Grid Service Participation
P. S. Glücker (2026), xxviii, 145 pp
ISBN: 978-3-95806-880-3

Band / Volume 691
A Parallel-in-Space Simulator for Accelerating Power System Simulation on Graphics Processing Units
J. Zhang (2026), 112 pp
ISBN: 978-3-95806-882-7

Band / Volume 692
Entwicklung von Reparaturmethoden für einkristalline Bauteile mittels thermischer Spritzverfahren
M. L. Létang (2026), X, 211 pp
ISBN: 978-3-95806-883-4

Band / Volume 693
Assessing the Environmental Implications of Offshore Wind Energy Advancements on the Future German Electricity Sector
A. Benitez (2026), xi, 176 pp
ISBN: 978-3-95806-885-8

Band / Volume 694
Entwicklung von Korrosionsschutzschichten für Protonen-Austausch-Membran-Wasserelektrolyseure
T. Sievert (2026), 201 pp
ISBN: 978-3-95806-888-9

Band / Volume 695
Hierarchical Modeling of Electrocatalytic Reactions from a Local Perspective
X. Zhu (2026), ix, 121 pp
ISBN: 978-3-95806-889-6

Weitere ***Schriften des Verlags im Forschungszentrum Jülich*** unter
http://wwwzb1.fz-juelich.de/verlagextern1/index.asp

Energie & Umwelt / Energy & Environment
Band / Volume 695
ISBN 978-3-95806-889-6

Mitglied der Helmholtz-Gemeinschaft

JÜLICH
Forschungszentrum